

On Least-Squares Gradient Reconstruction and its application in conjunction with a Rosenbrock method

A.E. Dahoe and R.S. Cant

This is a working document to explore the application of stiff integration methods on unstructured grids!

Abstract

The potential of a methodology to remedy the occurrence of high frequency oscillations in the spatial derivatives computed on an unstructured tetrahedral mesh was explored. To verify this methodology, called least-squares gradient reconstruction, the diffusion equation was solved as a test-case for the problem of an instantaneous spherical surface source enclosed by a spherical domain. The same problem was also solved by means of the finite volume method based on the Green-Gauss theorem for the sake of comparison. The origin of these high frequency oscillations could be identified by analyzing the application of the Green-Gauss theorem on an unstructured mesh. Based on the same arguments it was anticipated that least-squares gradient reconstruction would constitute a remedy to the problem. This expectation was confirmed by numerical simulations. It was also attempted to combine least-squares gradient reconstruction with a method for stiff time-integration. The performance of various time-integration methods was assessed on a couple of stiff test-problems involving chemical kinetics, and a Rosenbrock method was identified as a suitable candidate. The feasibility of combining it with least squares gradient reconstruction was explored by solving the one-dimensional Euler and Navier-Stokes equations involving chemical reaction.

1 Introduction

The use of unstructured meshes becomes increasingly important in the application of the finite volume method to solve flow problems. This development is driven by a growing interest to perform CFD simulations in complex geometries and a need to apply solution-adaptive meshing. Although algorithms for computations on structured grids have reached a much more advanced state in terms of accuracy and stability in comparison with those developed for an unstructured mesh, it is presently acknowledged that the application of the former to complex geometries becomes impractical. The principal cause of this problem is a lack of flexibility. The creation of a structured grid of a complex geometry is a labor-intensive and time consuming process because it requires the geometry to be subdivided into an ordered block structure. The establishment of the connectivity between the blocks composing the structure, as well as between the patches associated with them, involves a great deal of human time and is prone to error. Unstructured mesh generation does not rely on a block structure and reduces this time significantly. Additional, but equally important advantages of unstructured mesh generation are the flexibility to implement solution-adaptive meshing

and the prospect of conveniently modifying an existing geometry without having to accept a long period of unproductive time before a new mesh becomes available.

The computation of spatial derivatives on an unstructured grid is known to pose a challenge. While this may be accomplished by simple finite difference formulas on structured grids, a straightforward extension to unstructured grids appears to be absent. To overcome this deficiency, various approaches have been adopted to deal with spatial derivatives on an unstructured mesh. These involve control-volume finite element schemes that rely on shape functions, least-squares interpolation, and the discrete form of the divergence theorem. Unlike the first two approaches, which are specific to cell-shape, the latter may be used with cells of arbitrary shape. A feature which becomes particularly useful when one has to deal with mixed elements in near-wall regions to improve accuracy and to conserve memory. It is for this reason that the discrete divergence theorem is being applied in research codes and a variety of commercial CFD-codes.

A persistent problem encountered with the application of the discrete divergence theorem on unstructured grids is the occurrence of high frequency oscillations in computed spatial derivatives. As will be clarified in the next section, these oscillations stem from the irregularity in the mesh and their magnitude scales with the mesh spacing. This has disastrous consequences for both the conservative integral formulations where the time variation of a conserved quantity depends on the surface value of the fluxes entering a control volume, as well as for non-conservative formulations where flux contributions appear as internal numerical sources involving the flux derivative. In the latter case, as the solution of a transient problem requires spatial differentiation prior to every consecutive time-integration step, the magnitude of these oscillations is continuously being amplified.

In the former case, it may be argued that, owing to the method of evaluating spatial derivative contributions by summing average values at the faces surrounding a control volume, the magnitude of these oscillations remains bounded during the solution process. Although this appears to be true, the presence of the oscillations may undo the main advantages of unstructured grids over structured ones. Nonlinear problems involving convective terms, as is the case with most flow problems of practical interest, possess a tendency to shift variations in the solution (i.e. quantities with a nonzero first spatial derivative) around in space. Errors of a large magnitude originating from coarse regions where the solution is of little interest, are therefore being convected into refined regions. As a result, the solution in these regions of interest, where unstructured meshing is supposed to prove its usefulness, is being corrupted and the advantages of an increased local spatial resolution are being nullified. Moreover, the magnitude of high frequency oscillations originating from coarse regions at a previous time-step may be so large that it renders the solution at a refined region useless as an initial condition for a next time-step.

Taking the foregoing into consideration, it is the purpose of the present paper to explore a remedy to the occurrence of high frequency oscillations in the spatial derivatives computed on an unstructured mesh. Least-squares gradient reconstruction is proposed as an alternative to the discrete divergence theorem and three legitimate issues associated with it are addressed. The first issue concerns an assessment of what actually happens when the discrete divergence theorem is employed to compute spatial derivatives. For this purpose it was decided to solve the diffusion equation for the problem of an instantaneous spherical surface source. The problem was solved on a three-dimensional cartesian unstructured mesh of a sphere with zero Neumann boundary conditions on the surface. The diffusion equation was chosen as the test problem because its solution depends entirely on second order spatial derivatives,

and, higher order derivatives are known to suffer more from geometric irregularities of an unstructured mesh. Another reason for solving the diffusion equation was that it is a linear problem. Owing to the linear dependence of the time derivative on the spatial derivatives, irregularities in the solution are a reliable measure of what happens to the spatial derivatives. A distortion of the spatial derivatives at a particular location within the mesh emerges at the same place in the solution field, and scales linearly with the time increment. Moreover, nonlinear terms that may give rise to oscillations, or may amplify and shift existing ones, are absent. A final reason solving the diffusion equation was that analytical solutions may be derived for the problem considered.

The second issue is that of the existence of an equivalent of finite difference formulas for unstructured grids. It was stated earlier that an extension of such formulas appears to be absent. In the present paper it is attempted to generalize finite differences to a least-squares gradient reconstruction method. The method employs a Taylor-expansion of each quantity of interest at each nodal point of the grid and finds the spatial derivatives by fitting it to sufficient nearest neighbors in the least-squares sense. It is based on the anticipation that the irregularity of the mesh is compensated for by choosing the separation between each nearest-neighbor and the vertex of interest along the coordinate-axes as a basis, and to treat the partial derivatives as degrees of freedom. The diffusion equation, as discussed previously, was solved using least-squares gradient reconstruction and the results are compared with those obtained by means of the discrete divergence theorem.

The third issue is related to the feasibility of establishing comprehensive numerical schemes based on least-squares gradient reconstruction. The establishment of an alternative method with superior properties when it concerns the computation of spatial derivatives does not automatically imply overall improvement within the broad spectrum of existing comprehensive schemes. To shed light on this matter, it is attempted to combine least-squares gradient reconstruction with two different time-integration methods, namely, a classical one for non-stiff problems and one for stiff problems. As a first test case, least-squares gradient reconstruction is combined with the well-known explicit Runge-Kutta method, and subsequently applied to the aforementioned diffusion problem (Section 6). Next, least-squares gradient reconstruction is combined with a Rosenbrock method. In a second test case, this combination of methods is applied to the compressible Euler equations involving exothermic chemical reaction (Section 7). In a third test case, this combination of methods is applied to the compressible Navier-Stokes equations involving exothermic chemical reaction (Section 8).

Prior to the selection of the Rosenbrock method, three stiff problems involving chemical kinetics were collected from the literature and subjected to various time-integration methods (Section 5) for the sake of comparison. The methods investigated were: a one step explicit Runge-Kutta method (5^{th} -order), two multi-step implicit Adams-Moulton methods (2^{nd} - and 5^{th} -order), two multi-step implicit Gear methods (2^{nd} - and 5^{th} -order), a variable order multi-step Gear method, and, a one-step semi-implicit Rosenbrock method (4^{th} -order).

2 High frequency oscillations in spatial derivatives arising from the Green-Gauss theorem

Broadly speaking, the discrete form of familiar vector differentiation operators, such as the gradient, divergence, and curl, may simply be derived from the so called Green-Gauss

theorem,

$$\iiint_V \nabla \circ \Psi dV = \iint_S d\mathbf{S} \circ \Psi \quad (1)$$

$$\Rightarrow \nabla \circ \Psi = \lim_{\Delta V \rightarrow 0} \frac{1}{\Delta V} \oint_{\Delta S} d\mathbf{S} \circ \Psi \approx \frac{1}{\Delta V} \sum_{i=1}^{\text{nfaces}} \Delta \mathbf{S}_i \circ \tilde{\Psi}_i \quad (2)$$

where Ψ may be a scalar, vector, or tensor quantity, and \circ may denote the scalar, dot, cross, or intermediate product. The approximation on the right hand side of the above equation is illustrated by Figure 1. It simply states that the spatial derivative of a quantity within a cell may be expressed as the product between the average value at the face and its vector area, summed over all faces, and subsequently divided by the volume of the cell. Obviously, this approximation puts no limitation on the shape of the cell.

With unstructured grids it is observed that the application of equation (2) leads to high frequency oscillations in the computed spatial derivatives. The origin of this problem may be attributed to the fact that the average value at the face is estimated by an oversimplification. Formally, this should be done by evaluating

$$\tilde{\Psi}_i = \frac{1}{\Delta S_i} \iint_{\Delta S_i} \Psi dS, \quad (3)$$

where $\Delta S_i = |\Delta \mathbf{S}_i|$, which can only be accomplished when Ψ is known at every point of the surface. Because the value of Ψ is only known at discrete points in space, $k_1, k_2, \dots, k_{\text{nnode}}$, and to keep the computational burden at a minimum, it is common practice to calculate $\tilde{\Psi}_i$ by taking the arithmetic mean of Ψ at the nodal points spanning the face,

$$\tilde{\Psi}_i = \frac{1}{3} (\Psi(\mathbf{x}_{k_1}) + \Psi(\mathbf{x}_{k_2}) + \Psi(\mathbf{x}_{k_3})), \quad (4)$$

prior to the summation over all faces. This practice is based on the argument that any variation of Ψ may locally be approximated by a linear variation and that the mean value at the face may be calculated by the aforementioned expression. To see why this is an oversimplification and to understand how it gives rise to these high frequency oscillations, it is helpful to evaluate equation (2) and to inquire what happens when the mean value at the face is calculated by (4) instead of (3).

When the shaded face shown in Figure 1 is parametrized by u and v , such that

$$\begin{aligned} x &= x_1(1-u-v) + x_2u + x_3v \\ y &= y_1(1-u-v) + y_2u + y_3v \\ z &= z_1(1-u-v) + z_2u + z_3v \end{aligned} \quad u, v \in [0, 1], \quad (5)$$

equation (3) may be evaluated as

$$\tilde{\Psi}_i = \frac{1}{\Delta S_i} \iint_{\Delta S_i} \Psi(x, y, z) dS = \frac{1}{\frac{1}{2}|\mathbf{t}_u \times \mathbf{t}_v|} \int_0^1 \left[\int_0^{1-u} \Psi(u, v) |\mathbf{t}_u \times \mathbf{t}_v| dv \right] du, \quad (6)$$

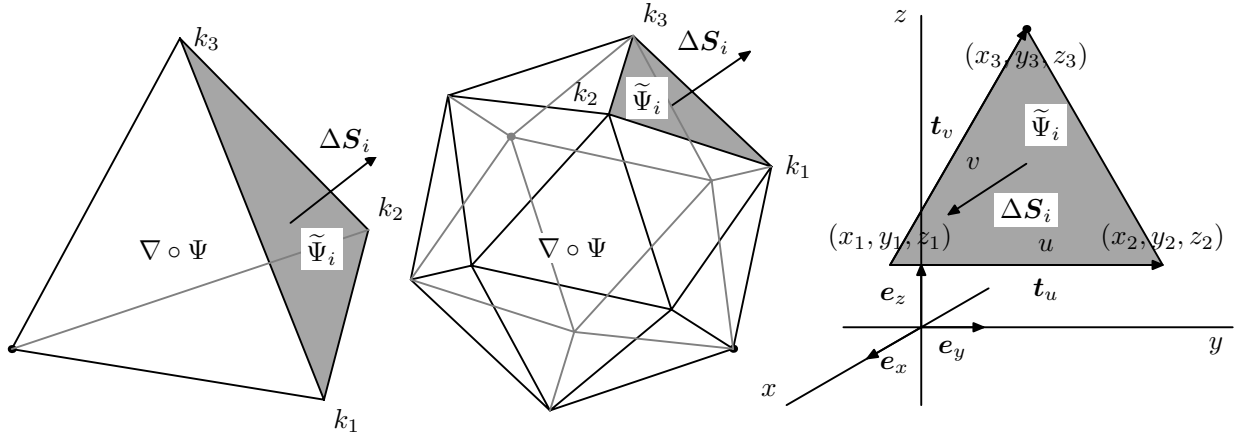


Figure 1. Application of the Green-Gauss theorem to approximate spatial derivatives within arbitrarily shaped cells. The quantities k_1 , k_2 and k_3 are node-indices.

where \mathbf{t}_u and \mathbf{t}_v are tangent vectors to the local coordinate lines, defined as

$$\begin{aligned}\mathbf{t}_u &= e_x \frac{\partial x}{\partial u} + e_y \frac{\partial y}{\partial u} + e_z \frac{\partial z}{\partial u} = (-x_1 + x_2)\mathbf{e}_x + (-y_1 + y_2)\mathbf{e}_y + (-z_1 + z_2)\mathbf{e}_z \\ \mathbf{t}_v &= e_x \frac{\partial x}{\partial v} + e_y \frac{\partial y}{\partial v} + e_z \frac{\partial z}{\partial v} = (-x_1 + x_3)\mathbf{e}_x + (-y_1 + y_3)\mathbf{e}_y + (-z_1 + z_3)\mathbf{e}_z.\end{aligned}\quad (7)$$

The parametrization (5) is such that the length of these vectors is equal to that of the edges of the triangle where they coincide. Hence, the magnitude of their cross product is twice the area of the triangle. If Ψ varies in space as

$$\begin{aligned}\Psi(x, y, z) = \Psi_0 + \beta_x x + \beta_{xy} y + \beta_z z + \frac{1}{2}\beta_{xx}x^2 + \frac{1}{2}\beta_{yy}y^2 + \frac{1}{2}\beta_{zz}z^2 \\ + \beta_{xy}xy + \beta_{xz}xz + \beta_{yz}yz + \dots,\end{aligned}\quad (8)$$

equation (3) leads to

$$\begin{aligned}\tilde{\Psi}_i = \Psi_0 + \frac{1}{3}\beta_x(x_1 + x_2 + x_3) + \frac{1}{3}\beta_y(y_1 + y_2 + y_3) + \frac{1}{3}\beta_z(z_1 + z_2 + z_3) \\ + \frac{1}{12}\beta_{xx}(x_1^2 + x_2^2 + x_3^2 + x_2x_3 + x_1(x_2 + x_3)) \\ + \frac{1}{12}\beta_{yy}(y_1^2 + y_2^2 + y_3^2 + y_2y_3 + y_1(y_2 + y_3)) \\ + \frac{1}{12}\beta_{zz}(z_1^2 + z_2^2 + z_3^2 + z_2z_3 + z_1(z_2 + z_3)) \\ + \frac{1}{12}\beta_{xy}(x_1(2y_1 + y_2 + y_3) + x_2(y_1 + 2y_2 + y_3) + x_3(y_1 + y_2 + 2y_3)) \\ + \frac{1}{12}\beta_{xz}(x_1(2z_1 + z_2 + z_3) + x_2(z_1 + 2z_2 + z_3) + x_3(z_1 + z_2 + 2z_3)) \\ + \frac{1}{12}\beta_{yz}(y_1(2z_1 + z_2 + z_3) + y_2(z_1 + 2z_2 + z_3) + y_3(z_1 + z_2 + 2z_3)) + \dots,\end{aligned}\quad (9)$$

for the mean value at the face, while the outcome of equation (4) does not extend beyond the fourth term on the right hand side. As a result, the application of equation (4) introduces an error which scales quadratically with the local mesh spacing. On a regular mesh this would only lead to a systematic error. In case of an unstructured grid, there is not only a systematic error, but irregularities in the mesh spacing are additionally being reflected in the computed spatial derivatives. Hence the high frequency oscillations.

3 Gradient Reconstruction

The removal of non-physical oscillations became a topic of active research when accurate approximations on regular structured grids were difficult to obtain due to solution discontinuities. Godunov [1] proposed a scheme involving a first-order accurate piecewise-constant reconstruction, which has proven to be quite an effective remedy. However, inadequacies arising from its first-order accuracy made it necessary to resort to schemes with greater accuracy, involving gradient reconstruction. A scheme with improved accuracy in smooth regions and less smearing of solution discontinuities, based on second-order accurate piecewise-linear reconstruction, was proposed by Van Leer [2]. The merits of this scheme in conjunction with various flux limiters are well-known from computations on structured grids and inspired sustained efforts to derive similar ones with higher order accuracy. This resulted in the development of the piecewise-parabolic method (PPM) [3], uniformly high order accurate non-oscillatory schemes (UNO) [4], essentially non-oscillatory schemes (ENO) [5], and weighted essentially non-oscillatory schemes (WENO) [6, 7].

As explained in the previous section, solution discontinuities are not the only cause of non-physical oscillations. They are also seen to arise from smooth solutions on unstructured grids. Because of the similarity between non-physical oscillations originating from solution discontinuities on structured grids, and those arising from mesh irregularity within unstructured ones, various researchers have applied these so called reconstruction-evolution methods (they are also known as MUSCL-type methods) to unstructured grids. However, instead of providing a remedy to the problem, these attempts have unveiled their limitation when mesh irregularity turns out to be the culprit. Cabello, Morgan & Lohner [8] compared the performance of several high order accurate reconstruction-evolution methods by simulating a one-dimensional shock tube problem on a two-dimensional isotropic and non-isotropic mesh. The poor performance on a distorted grid, as observed by these authors, is attributed to the one-dimensional nature of the reconstruction-evolution methods, and calls for a multi-dimensional approach [9]. This conclusion is also supported by findings of other researchers [10–13], who attempted to implement the one-dimensional reconstruction-evolution approach in higher order upwind schemes on unstructured grids.

Barth and Jespersen [14] were the first to introduce a multi-dimensional technique, called linear reconstruction, for the computation of solutions of the Euler equations on a two-dimensional unstructured grid. Their aim was to compute solutions with an accuracy greater than first order and to suppress the occurrence of local extrema arising from mesh irregularity, as well as from solution discontinuities. Their strategy was to enlarge the computational stencil by including the centroid-centroid path tracing the convex hull of the neighbor set of all centroids that share a common vertex with a parent cell (see Figure 2), and to employ the Green-Gauss theorem in conjunction with a limiter. The gradient within a cell is computed using values at the centroids of its nearest neighbors and the limiter ensures that the linearly reconstructed solution never exceeds the minimum and maximum of the neighboring centroid values (including the centroid of the parent cell). The technique by Barth and Jespersen will be outlined to provide a frame of reference. In what follows, the terminology used will be that of three-dimensional problems (i.e. triangles become tetrahedra, the surface area becomes a volume, and edges become faces), despite the two-dimensional nature of what could be found in the literature. It is assumed that this does not affect the integrity of the works cited.

A linear representation of the state variables about some as yet arbitrary origin, (x_j, y_j, z_j) ,

within a parent cell (i.e. the region indexed by j in Figure 2) is sought,

$$\begin{aligned}\Psi(x - x_j, y - y_j, z - z_j) &= \Psi(x_j, y_j, z_j) + \frac{\partial\Psi}{\partial x}\Big|_j (x - x_j) + \frac{\partial\Psi}{\partial y}\Big|_j (y - y_j) + \frac{\partial\Psi}{\partial z}\Big|_j (z - z_j) \\ &= \Psi(x_j, y_j, z_j) + \nabla\Psi|_j \cdot \Delta\mathbf{r},\end{aligned}\quad (10)$$

with the requirement that its volume average is a redistribution of the cell-averaged data,

$$\bar{\Psi}(x_j, y_j, z_j) = \frac{1}{\Delta V_j} \iiint_{\Delta V_j} \Psi(x - x_j, y - y_j, z - z_j) dV. \quad (11)$$

As this condition is satisfied for any constant gradient vector when (x_j, y_j, z_j) coincides with the centroid of cell j , the vector $\nabla\Psi|_j$ is the best approximation of the gradient within the cell, as computed from values at surrounding centroids. Oscillations in the reconstructed solution belonging to the parent cell, $\Psi(x - x_j, y - y_j, z - z_j)$, are suppressed by invoking a limiter into (10),

$$\Psi(x - x_j, y - y_j, z - z_j) = \Psi(x_j, y_j, z_j) + \Phi_j \nabla\Psi|_j \cdot \Delta\mathbf{r}_j \quad \Phi_j \in [0, 1], \quad (12)$$

and to seek the largest admissible Φ_j while imposing a “monotonicity principle” that values of the linearly reconstructed solution, $\Psi(x - x_j, y - y_j, z - z_j)$, may not exceed the extrema of neighboring centroids (including the centroid of the parent cell). The value of the limiter is calculated as follows. First, Ψ_j^{\min} and Ψ_j^{\max} are calculated as

$$\Psi_j^{\min} = \min(\Psi_j, \Psi_j^i) \quad i = 1, \dots, n\text{centroids} \quad (13)$$

$$\Psi_j^{\max} = \max(\Psi_A, \Psi_j^i) \quad i = 1, \dots, n\text{centroids}, \quad (14)$$

so that the reconstructed solution satisfies

$$\Psi_j^{\min} \leq \Psi(x - x_j, y - y_j, z - z_j) \leq \Psi_j^{\max}. \quad (15)$$

Next, the value of the limiter is sought by using the solution at the vertices spanning the faces that enclose the cell. The value at each of these vertices is employed as

$$\bar{\Phi}_j^i = \begin{cases} \min\left(1, \frac{\Psi_j^{\max} - \Psi_k}{\Psi_k - \Psi_j}\right) & \text{if } \Psi_k - \Psi_j > 0 \\ \min\left(1, \frac{\Psi_j^{\min} - \Psi_k}{\Psi_k - \Psi_j}\right) & \text{if } \Psi_k - \Psi_j < 0 \\ 1 & \text{if } \Psi_k - \Psi_j = 0 \end{cases} \quad k = 1, \dots, n\text{vertices}_i, \quad (16)$$

followed by

$$\Phi_j = \min(\bar{\Phi}_j^1, \bar{\Phi}_j^2, \dots, \bar{\Phi}_j^i, \dots, \bar{\Phi}_j^{n\text{faces}}). \quad (17)$$

According to Barth and Jespersen this procedure guarantees the monotonicity principle for reconstructed state variables anywhere within the parent cell, even when equation (16) is evaluated on the basis of values at isolated points on enclosing faces. When combined with the discrete Green-Gauss theorem (3), it amounts to compensating the effect of mesh

irregularity by introducing a multiplicative factor,

$$\nabla \circ \Psi|_j = \frac{\Phi_j}{\Delta V_j} \sum_{i=1}^{\text{nface}} \Delta S_j^i \circ \tilde{\Psi}_i, \quad (18)$$

which attempts to exclude the occurrence of local extrema in the computed derivatives (see Murthy and Mathur [15, 16] for examples of its application). To Barth and Jespersen, true second order accuracy appeared possible with smoothly varying unstructured meshes, but not with meshes containing abrupt changes in cell size. However, significant improvement over the first order scheme was observed.

In a later contribution Barth and Frederickson [17] proposed a higher order finite volume extension to Godunov's scheme for arbitrary unstructured meshes based on quadratic and higher order reconstruction, involving a generalization of equation (10),

$$\begin{aligned} \Psi(x - x_j, y - y_j, z - z_j) &= \Psi(x_j, y_j, z_j) + \left. \frac{\partial \Psi}{\partial x} \right|_j (x - x_j) + \left. \frac{\partial \Psi}{\partial y} \right|_j (y - y_j) \\ &+ \left. \frac{\partial \Psi}{\partial z} \right|_j (z - z_j) + \frac{1}{2} \left. \frac{\partial^2 \Psi}{\partial x^2} \right|_j (x - x_j)^2 + \frac{1}{2} \left. \frac{\partial^2 \Psi}{\partial y^2} \right|_j (y - y_j)^2 \\ &+ \frac{1}{2} \left. \frac{\partial^2 \Psi}{\partial z^2} \right|_j (z - z_j)^2 + \left. \frac{\partial^2 \Psi}{\partial x \partial y} \right|_j (x - x_j)(y - y_j) + \left. \frac{\partial^2 \Psi}{\partial x \partial z} \right|_j (x - x_j)(z - z_j) \\ &+ \left. \frac{\partial^2 \Psi}{\partial y \partial z} \right|_j (y - y_j)(z - z_j) + \dots \end{aligned} \quad (19)$$

or equivalently,

$$\Psi^k(x - x_j, y - y_j, z - z_j) = \sum_{l+m+n \leq k} \alpha_{(l,m,n)} P_{(l,m,n)}(x - x_j, y - y_j, z - z_j). \quad (20)$$

In the preceding equation, k denotes the degree of the polynomial,

$$P_{(l,m,n)}(x - x_j, y - y_j, z - z_j) = (x - x_j)^l (y - y_j)^m (z - z_j)^n \quad (21)$$

the basis of the polynomial, and $\alpha_{(l,m,n)}$ the polynomial coefficients which are to be reconstructed given the integral cell averages in all cells. The cell averages are computed according to equation (11), and subsequently used to compute the polynomial coefficients as

$$\alpha_{(l,m,n)} = \sum_{j=1}^{\text{ncells}} W_{(l,m,n)} \bar{\Psi}(x_j, y_j, z_j), \quad (22)$$

where $W_{(l,m,n)}$ are weight factors pre-computed from geometrical properties of the mesh.

Because of difficulties encountered with the implementation of the method by Barth and Jespersen [14] in three dimensions, Frink [18, 19] developed a simpler higher order method. This approach embodies a coalescence of surrounding cell information to the vertices of the parent cell, followed by the application of the discrete Green-Gauss theorem. A weighted average of the cell-centered solution quantities is taken to be the value of the vertices spanning the parent cell. The contribution to a vertex belonging to the parent cell is assumed to be inversely proportional to the distance of the centroid of each surrounding cell. This

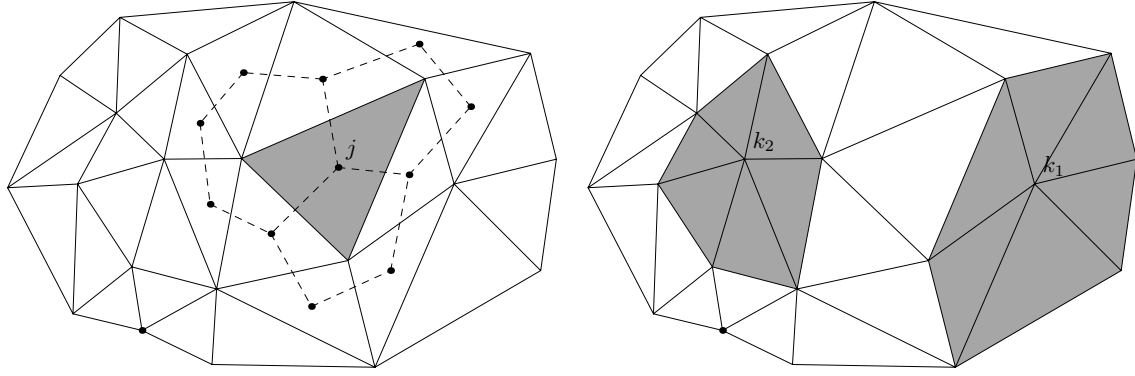


Figure 2. Computational stencil after Barth and Jespersen [14] involving the centroids of all neighboring cells that share a common vertex with the parent cell (left) and computational stencils used by the Least-Squares Gradient Reconstruction method (right).

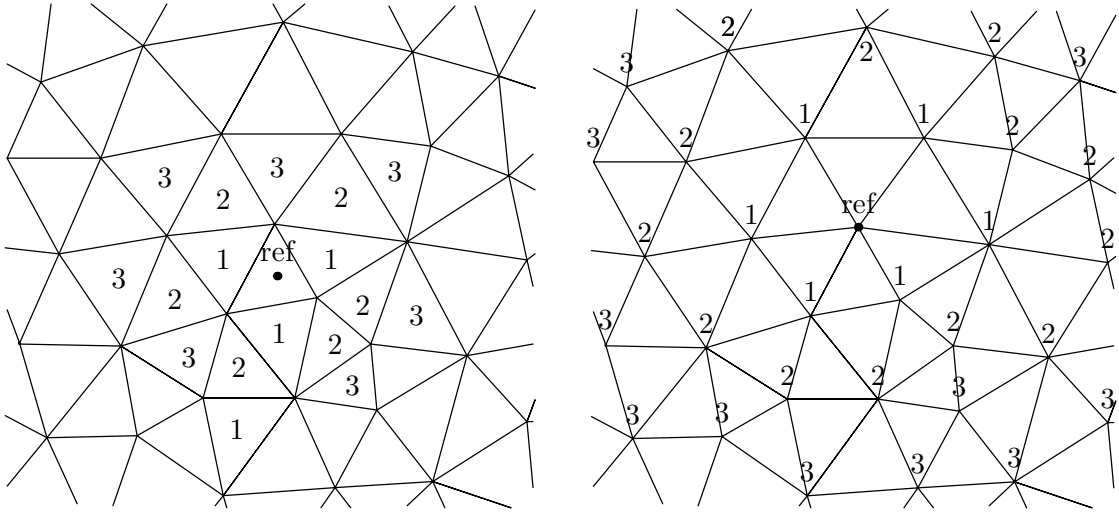


Figure 3. Cell-centered (left) and vertex-centered (right) control volumes after Ollivier-Gooch & Van Althena [21]. Nearby-neighbors are ranked according to the relative topological proximity with respect to a reference node or cell.

proportionality is taken into account by means of Shepard's formula [20],

$$\Psi_k = \sum_{i=1}^{\text{ncell}} (\Psi_i / r_i) \Big/ \sum_{i=1}^{\text{ncell}} (1/r_i), \quad (23)$$

where $r_i = [(x_i - x_k) + (y_i - y_k) + (z_i - z_k)]^{1/2}$, the index k corresponds to the cell vertex, and, the index i refers to the surrounding cell-centered values. Higher order accuracy could be achieved by expanding Ψ in a Taylor series to the faces, once the gradient has been computed in a cell. The use of a limiter appeared unnecessary to capture shocks without oscillations. This behavior is ascribed to the possibility that the application of this averaging procedure across discontinuities introduces additional dissipation and a reduction in accuracy, as is characteristic to limiters.

To overcome implementation difficulties of reconstruction-evolution methods with arbitrary unstructured meshes, Ollivier-Gooch & Van Althena [21], proposed a scheme based on least-squares reconstruction of the solution from cell-averaged data. The key idea is to

replace the volume averaged value of the solution (i.e. $\bar{\Psi}(x_j, y_j, z_j)$ on the left hand side of equation (11)) by a Taylor expansion (i.e. the right hand side of equation (10)). This replacement results in a polynomial, with $\Psi(x_j, y_j, z_j)$ being the reconstructed solution, and $\partial^{l+m+n}\Psi/\partial x^l y^m z^n|_j$ being its partial derivatives, as coefficients to be determined in the least-squares sense. Once the coefficients are known, values of the reconstructed solution can be computed anywhere within a cell-centered or vertex-centered control volume (see Figure 3). Support by neighboring control volumes is implemented as follows. With i denoting the index of an arbitrary control volume, and j being the index of the reference control volume where reconstruction is supposed to be effective, the volume average of Ψ (see equation (11)) may be expanded as [21, 22]:

$$\begin{aligned} \frac{1}{\Delta V_j} \iint_{\Delta V_j} \Psi(x - x_i, y - y_i, z - z_i) dV = \\ \Psi(x_i, y_i, z_i) + \frac{\partial \Psi}{\partial x} \Big|_i \frac{1}{\Delta V_j} \iint_{\Delta V_j} (x - x_i) dV + \frac{\partial \Psi}{\partial y} \Big|_i \frac{1}{\Delta V_j} \iint_{\Delta V_j} (y - y_i) dV \\ + \frac{\partial \Psi}{\partial z} \Big|_i \frac{1}{\Delta V_j} \iint_{\Delta V_j} (z - z_i) dV + \frac{\partial^2 \Psi}{\partial x^2} \Big|_i \frac{1}{2\Delta V_j} \iint_{\Delta V_j} (x - x_i)^2 dV \\ + \frac{\partial^2 \Psi}{\partial x \partial y} \Big|_i \frac{1}{\Delta V_j} \iint_{\Delta V_j} (x - x_i)(y - y_i) dV + \dots \end{aligned} \quad (24)$$

Notice that when $j = i$, this equation becomes

$$\begin{aligned} \frac{1}{\Delta V_i} \iint_{\Delta V_i} \Psi(x - x_i, y - y_i, z - z_i) dV = \Psi(x_i, y_i, z_i) \\ + \frac{\partial \Psi}{\partial x} \Big|_i \bar{x}_i + \frac{\partial \Psi}{\partial y} \Big|_i \bar{y}_i + \frac{\partial \Psi}{\partial z} \Big|_i \bar{z}_i + \frac{1}{2} \frac{\partial^2 \Psi}{\partial x^2} \Big|_i (\bar{x}^2)_i + \frac{\partial^2 \Psi}{\partial x \partial y} \Big|_i (\bar{xy})_i + \dots \end{aligned} \quad (25)$$

where

$$(\bar{x}^l y^m z^n)_i = \frac{1}{\Delta V_i} \iint_{\Delta V_i} (x - x_i)^l (y - y_i)^m (z - z_i)^n dV. \quad (26)$$

Next, $(x - x_i)$, $(y - y_i)$, and $(z - z_i)$ are replaced by $(x - x_j) + (x_j - x_i)$, $(y - y_j) + (y_j - y_i)$, and $(z - z_j) + (z_j - z_i)$, respectively. After this substitution equation (24) transforms into

$$\begin{aligned} \frac{1}{\Delta V_j} \iint_{\Delta V_j} \Psi(x - x_i, y - y_i, z - z_i) dV = \Psi(x_i, y_i, z_i) \\ + \frac{\partial \Psi}{\partial x} \Big|_i (\hat{x})_{ij} + \frac{\partial \Psi}{\partial y} \Big|_i (\hat{y})_{ij} + \frac{\partial \Psi}{\partial z} \Big|_i (\hat{z})_{ij} + \frac{1}{2} \frac{\partial^2 \Psi}{\partial x^2} \Big|_i (\hat{x}^2)_{ij} + \frac{\partial^2 \Psi}{\partial x \partial y} \Big|_i (\hat{xy})_{ij} + \dots \end{aligned} \quad (27)$$

where the geometric terms are of the general form:

$$\begin{aligned}
(\widehat{x^l y^m z^n})_{ij} &= \frac{1}{\Delta V_j} \iiint_{\Delta V_j} [(x - x_j) + (x_j - x_i)]^l [(y - y_j) + (y_j - y_i)]^m [(z - z_j) + (z_j - z_i)]^n dV \\
&= \sum_{r=0}^n \sum_{q=0}^m \sum_{p=0}^l \binom{n}{r} \binom{m}{q} \binom{l}{p} (x_j - x_i)^l (y_j - y_i)^m (z_j - z_i)^n \left(\overline{x^{l-p} y^{m-q} z^{n-r}} \right)_j.
\end{aligned} \tag{28}$$

Equation (27) is subsequently cast into a linear least-squares problem:

$$\begin{bmatrix} 1 & \bar{x}_i & \bar{y}_i & \bar{z}_i & \bar{x^2}_i & \dots \\ w_{i1} & w_{i1}\hat{x}_{i1} & w_{i1}\hat{y}_{i1} & w_{i1}\hat{z}_{i1} & w_{i1}\hat{x^2}_{i1} & \dots \\ w_{i2} & w_{i2}\hat{x}_{i2} & w_{i2}\hat{y}_{i2} & w_{i2}\hat{z}_{i2} & w_{i2}\hat{x^2}_{i2} & \dots \\ w_{i3} & w_{i3}\hat{x}_{i3} & w_{i3}\hat{y}_{i3} & w_{i3}\hat{z}_{i3} & w_{i3}\hat{x^2}_{i3} & \dots \\ \vdots & \vdots & \vdots & \vdots & \vdots & \ddots \\ w_{iN} & w_{iN}\hat{x}_{iN} & w_{iN}\hat{y}_{iN} & w_{iN}\hat{z}_{iN} & w_{iN}\hat{x^2}_{iN} & \dots \end{bmatrix} \begin{bmatrix} \Psi \\ \frac{\partial \Psi}{\partial x} \\ \frac{\partial \Psi}{\partial y} \\ \frac{\partial \Psi}{\partial z} \\ \frac{1}{2} \frac{\partial^2 \Psi}{\partial x \partial y} \end{bmatrix}_i = \begin{bmatrix} \bar{\Psi}_i \\ w_{i1}\bar{\Psi}_1 \\ w_{i2}\bar{\Psi}_2 \\ w_{i3}\bar{\Psi}_3 \\ \vdots \\ w_{iN}\bar{\Psi}_N \end{bmatrix} \tag{29}$$

where N denotes the number of nearby control volumes contained by the computational stencil and w_{ij} are weights that scale quadratically with the inverse distance of nearby control volume locations. Prior to the calculation of the flux integral over a reference control volume, equation (27), is least-squares fitted to a computational stencil containing sufficient nearest neighbors, as described by (29), with $\Psi(x_i, y_i, z_i)$ and its derivatives $(\partial\Psi/\partial x)_i, (\partial\Psi/\partial y)_i, \dots$, as degrees of freedom. The resulting values are then used to reconstruct the solution for the computation of vector differentiation operators using the Green-Gauss theorem.

4 Least-squares gradient reconstruction

Before outlining the least-squares gradient reconstruction method, it is helpful to expose an important contrast with the reconstruction-evolution methods reviewed in the previous section. These methods employ the discrete form of a dependent quantity, $\Psi(x - x_j, y - y_j, z - z_j)$, as the cell-integral average, $\bar{\Psi}(x - x_j, y - y_j, z - z_j)$, as defined by equation (11), which is characteristic to the finite volume method. By contrast, least-squares gradient reconstruction, as applied in the present work, represents the discrete form of the same quantity by vertex-centered samples, located at the nodal points of the mesh. This makes the method equivalent to finite differencing.

With j being the index of a reference node where spatial derivatives are to be evaluated (see the right parts of Figures 2 and 3), and i denoting its nearby-neighbors, a least-squares

gradient reconstruction may be established by restating equation (19) as

$$\begin{aligned}
\Psi(x_i - x_j, y_i - y_j, z_i - z_j) - \Psi(x_j, y_j, z_j) &= \frac{\partial \Psi}{\partial x} \Big|_j (x_i - x_j) + \frac{\partial \Psi}{\partial y} \Big|_j (y_i - y_j) \\
&+ \frac{\partial \Psi}{\partial z} \Big|_j (z_i - z_j) + \frac{1}{2} \frac{\partial^2 \Psi}{\partial x^2} \Big|_j (x_i - x_j)^2 + \frac{1}{2} \frac{\partial^2 \Psi}{\partial y^2} \Big|_j (y_i - y_j)^2 \\
&+ \frac{1}{2} \frac{\partial^2 \Psi}{\partial z^2} \Big|_j (z_i - z_j)^2 + \frac{\partial^2 \Psi}{\partial x \partial y} \Big|_j (x_i - x_j)(y_i - y_j) + \frac{\partial^2 \Psi}{\partial x \partial z} \Big|_j (x_i - x_j)(z_i - z_j) \\
&+ \frac{\partial^2 \Psi}{\partial y \partial z} \Big|_j (y_i - y_j)(z_i - z_j) + \dots
\end{aligned} \tag{30}$$

In compact form, this expression becomes

$$\mathbf{A} \cdot \boldsymbol{\beta} = \mathbf{f}, \quad \mathbf{A} \in \mathbb{R}^{M \times N}, \boldsymbol{\beta} \in \mathbb{R}^{N \times 1}, \mathbf{f} \in \mathbb{R}^{M \times 1} \tag{31}$$

where N denotes the number of partial derivatives of Ψ at the reference node, $M(\geq N)$ denotes the number of nearby neighbors,

$$\mathbf{A} = \begin{bmatrix} (x_1 - x_j) & (y_1 - y_j) & \cdots & (x_1 - x_j)^l (y_1 - y_j)^m (z_1 - z_j)^n \\ (x_2 - x_j) & (y_2 - y_j) & \cdots & (x_2 - x_j)^l (y_2 - y_j)^m (z_2 - z_j)^n \\ \vdots & \vdots & \ddots & \vdots \\ (x_i - x_j) & (y_i - y_j) & \cdots & (x_i - x_j)^l (y_i - y_j)^m (z_i - z_j)^n \\ \vdots & \vdots & \ddots & \vdots \\ (x_M - x_j) & (y_M - y_j) & \cdots & (x_M - x_j)^l (y_M - y_j)^m (z_M - z_j)^n \end{bmatrix}, \tag{32}$$

$$\boldsymbol{\beta} = \begin{bmatrix} \frac{\partial \Psi}{\partial x} \\ \frac{\partial \Psi}{\partial y} \\ \frac{\partial \Psi}{\partial z} \\ \frac{1}{2} \frac{\partial^2 \Psi}{\partial x^2} \\ \vdots \end{bmatrix} \quad \text{and} \quad \mathbf{f} = \begin{bmatrix} \Psi(x_1 - x_j, y_1 - y_j, z_1 - z_j) - \Psi(x_j, y_j, z_j) \\ \vdots \\ \Psi(x_i - x_j, y_i - y_j, z_i - z_j) - \Psi(x_j, y_j, z_j) \\ \vdots \\ \Psi(x_M - x_j, y_M - y_j, z_M - z_j) - \Psi(x_j, y_j, z_j) \end{bmatrix} \tag{33}$$

where $l + m + n \equiv N$, and N assumes discrete values of 3, 9, 27, 81, ..., for first, second, third, fourth, ..., -order accurate spatial derivatives. The spatial derivatives are obtained by seeking the solution of $\boldsymbol{\beta}$, containing the spatial derivatives, in equation (30), involving sufficient nearby-neighbors (i.e. $M \geq N$).

Because M has to be greater than, or equal to N to avoid redundancy in the least-squares solution, the data matrix \mathbf{A} has a rectangular structure, and the solution of equation (30) must be sought in the least-squares sense i.e. finding an estimate of $\boldsymbol{\beta}$ that renders

$$\min \| \mathbf{A} \boldsymbol{\beta} - \mathbf{f} \|_2 \tag{34}$$

Since the accuracy of the solution computed by means of the classical approach based on the

normal equations is known to depend on the square of the condition [23], it was decided to solve the full-rank problem by means of QR-factorization involving Householder reflections. Details of its motivation and implementation may be found in Businger & Golub [24, 25].

Boundary conditions are implemented as follows. In case of Dirichlet conditions, $\Psi(x_i - x_j, y_i - y_j, z_i - z_j)$ and $\Psi(x_j, y_j, z_j)$ at boundary nodes (any node composing a control volume may reside on the boundary) are clamped to a fixed value. Neumann conditions are imposed by means of a constrained optimization. This is accomplished by restating equation (30) as

$$\begin{aligned} & [\Psi(x_i - x_j, y_i - y_j, z_i - z_j) - \Psi(x_j, y_j, z_j)] \\ & - \frac{\partial \Psi}{\partial x} \Big|_j^{\text{fixed}} (x_i - x_j) - \frac{\partial \Psi}{\partial y} \Big|_j^{\text{fixed}} (y_i - y_j) - \frac{\partial \Psi}{\partial z} \Big|_j^{\text{fixed}} (z_i - z_j) = \\ & \frac{1}{2} \frac{\partial^2 \Psi}{\partial x^2} \Big|_j (x_i - x_j)^2 + \frac{1}{2} \frac{\partial^2 \Psi}{\partial y^2} \Big|_j (y_i - y_j)^2 + \frac{1}{2} \frac{\partial^2 \Psi}{\partial z^2} \Big|_j (z_i - z_j)^2 \\ & + \frac{\partial^2 \Psi}{\partial x \partial y} \Big|_j (x_i - x_j)(y_i - y_j) + \frac{\partial^2 \Psi}{\partial x \partial z} \Big|_j (x_i - x_j)(z_i - z_j) + \frac{\partial^2 \Psi}{\partial y \partial z} \Big|_j (y_i - y_j)(z_i - z_j) + \dots \end{aligned} \tag{35}$$

and to fix the components of the gradient of Ψ .

5 Assessment of time-integration schemes on stiff problems

5.1 Integration of stiff problems

Stiffness is a phenomenon often encountered with systems of ordinary differential equations in chemical applications. From a practical point of view there exists a step-size constraint which makes the numerical solution with conventional integration methods nearly impossible. Since the discovery of numerical instability as the cause of this constraint, two distinct approaches have been explored for the numerical solution of stiff equations. The first approach aims at removing stiffness by the use of preliminary mathematical transformations so that the solution of the transformed system becomes feasible with conventional integration methods. The second approach, which is the one adopted in the present work, focuses on the development of numerical integration methods, suitable for stiff systems. As this development has remained the subject of ongoing research, there is always the issue of selecting the best available method.

The most important criterion in the choice of a method is set by the observation that the numerical instability is connected to the requirement that local transient components which, although of negligible amplitude with respect to the overall solution, must be resolved on the smallest time scales. Insufficient temporal resolution, or the inability to resolve these amplitudes with sufficient accuracy, inevitably leads to a wrong solution or a rapid overflow of the floating point dynamic range. The onset and growth of such instability is illustrated by the sub-figure containing a magnification of ψ_2 in the lower part of Figure 4. A consequential issue concerns the ability to adapt the step size to the local behavior of the solution. Integration methods for stiff systems are deemed impractical in the absence of such capability. For example, the solution of a stiff system containing local transient components

with a characteristic time scale of 10^{-30} of the integration domain would require at least 10^{30} time steps without solution adaptive time-steps for a meaningful solution. Obviously, any stiff integrator, no matter how accurate and stable, should possess the capability to increase and decrease the step-size while preserving accuracy within a predefined error tolerance.

To monitor the performance of a particular integration method, it is common practice to observe the computer-time required to solve the problem, the number of function evaluations, the number of Jacobian evaluations and the number of time steps. An extensive comparison between various methods for the integration of stiff systems was made by Enright, Hull & Lindberg [26], Enright & Hull [27] and Enright & Pryce [28]. Methods investigated by these authors on the basis of these criteria were:

- three methods based on backward differentiation formulas, namely, those of Gear (DIFSUB) [29, 30], Hindmarsh (GEAR.REV3) [31] and Byrne & Hindmarsh (EPISODE) [32],
- their own version of a method based on the trapezoidal rule with extrapolation as discussed in Enright *et al.* [26] (TRAPEX),
- their own version of a method based on the fourth-order implicit Runge-Kutta formula by Butcher [33], as discussed in Enright *et al.* [26] (IMPRK),
- a generalized Runge-Kutta method by Lawson & Ehle [34] (GENRK), and,
- a variable order second derivative multistep method by Enright (DBASIC) *et al.* [35]

Specific test problems were collected from real examples in the literature and through private communications. These involved standard kinetic problems, kinetic problems with oscillatory solutions, and reactor problems. The methods were implemented into a driver program and subsequently applied to the test problems. Of all methods tested, only those based on backward differentiation formulas (DIFFSUB, GEAR.REV3 and EPISODE) and the one based on second derivative multistep formulas (SDBASIC) were found suitable. The other methods tested, GENRK and IMPRK, were found to be unreliable and inefficient, and therefore seemed to be unsuitable for stiff problems arising in chemistry. SDBASIC was observed to be the most reliable on the test problems, but at the same time less efficient than those based on backward differentiation formulas. The latter were consistently seen to be about three times more efficient than SDBASIC. It is for this reason that these authors conclude their investigation with the recommendation to begin with a method based on backward differentiation formulas, such as GEAR.REV3, and if trouble arises, to switch to a second derivative method such as SDBASIC.

5.2 Comparison of time-integration methods on stiff problems

The extensive application of backward differentiation formulas in production codes has revealed certain weaknesses arising from both the formulas and their implementations. Enright & Hull [27] pointed out that an inherent flaw of backward differentiation formulas is that they become very inefficient on stiff problems with eigenvalues of the Jacobian matrix close to the imaginary axis. Shampine [36] pointed out that, owing to implementation difficulties of the backward differentiation formulas, the Jacobian matrix is employed in a simplified Newton iteration for the evaluation of the implicit formulas and proposed a Rosenbrock formula as

an alternative. Although it is true that the Jacobian matrix serves merely as an aid in the solution process involving backward differentiation formulas, and a terrible approximation would suffice, this might not be the case with stiff problems. It was also pointed out by Shampine that it is common for production codes to accept problems in autonomous form, i.e. system (39) without t on the right hand side, thereby avoiding the special role of the independent variable. Systems containing the independent variable on the right hand side are usually being converted to the autonomous form by adding a new equation for the independent variable as if it were a dependent variable. In an earlier contribution Shampine [37] demonstrated that this conversion makes a non-linear problem out of a linear one. To avoid obscure consequences, he proposed a formulation of the Rosenbrock method that requires no transformation into an autonomous system.

Following Shampine's proposal for an alternative, and taking notice of the recommendation by Enright *et al.* it was decided to compare the performance of the Rosenbrock method with that of various contemporary implementations involving backward differentiation formulas on three test problems, namely, D2 (chemical kinetics, after Robertson [38]), D4 (chemical kinetics, after Gear [39]) and F1 (catalytic fluid bed, after Luss & Amundson [40] and Lapidus *et al.* [41]) by Enright & Pryce [28]. More specifically, the problems investigated were:

$$\begin{aligned} \frac{d\psi_1}{dt} &= -0.04\psi_1 + 10^4\psi_2\psi_3 & \psi_1(0) &= 1.0 \\ \frac{d\psi_2}{dt} &= 0.04\psi_1 - 10^4\psi_2\psi_3 - 3.0 \cdot 10^7\psi_2^2 & \psi_2(0) &= 0.0 \\ \frac{d\psi_3}{dt} &= 3.0 \cdot 10^7\psi_2^2 & \psi_3(0) &= 0.0, \end{aligned} \quad (36)$$

$$\begin{aligned} \frac{d\psi_1}{dt} &= -0.0013\psi_1 - 1000\psi_1\psi_3 & \psi_1(0) &= 1.0 \\ \frac{d\psi_2}{dt} &= -2500\psi_2\psi_3 & \psi_2(0) &= 1.0 \\ \frac{d\psi_3}{dt} &= 0.0013\psi_1 - 1000\psi_1\psi_3 - 2500\psi_2\psi_3 & \psi_3(0) &= 0.0, \end{aligned} \quad (37)$$

and

$$\begin{aligned} \frac{d\psi_1}{dt} &= 1.3(\psi_3 - \psi_1) + 10400k\psi_2 & \psi_1(0) &= 761.0 \\ \frac{d\psi_2}{dt} &= 1880[\psi_4 - \psi_2(1 + k)] & \psi_2(0) &= 0.0 \\ \frac{d\psi_3}{dt} &= 1752 - 269\psi_3 + 267\psi_1 & \psi_3(0) &= 600.0 \\ \frac{d\psi_4}{dt} &= 0.1 + 320\psi_2 - 321\psi_4 & \psi_4(0) &= 0.1 \end{aligned} \quad (38)$$

with $k = \exp(20.7 - 1500/\psi_1)$.

The performance of the backward differentiation formulas was tested by means of the driver programs LSODE [42] (the time-integrator of CHEMKIN II) and VODE [43] (the time-integrator of CHEMKIN III). The right-hand sides and Jacobian matrices were supplied

analytically, and the Adams-Moulton ($2^{nd}, 5^{th}$ -order) and Gear ($2^{nd}, 5^{th}$ -order) method with adaptive time-stepping were applied in case of LSODE. With VODE, a variable order Gear method was applied. The order of the method was seen to vary between 2 and 5 during the solution of the problems. For the Rosenbrock method (i.e. the 4^{th} -order Shampine implementation), a separate algorithm was developed to enable adaptive time-stepping on the basis of a methodology proposed by Press *et al.* [44]. The same algorithm was used to drive a 5^{th} -order explicit Runge-Kutta method for the sake of reference. The results of this comparison are summarized in Table 3 and the solutions are illustrated by Figure 4.

The Adams-Moulton and Gear methods applied in the present work, as well as implementation details in LSODE to enable adaptive time-stepping to meet a certain predefined error tolerance, are described by Radhakrishnan [42]. Implementation details and the stepsize-control strategy of the variable order Gear method in VODE are given by Brown, Byrne & Hindmarsh [43]. Only the Runge-Kutta method and the Rosenbrock method are described briefly here. For a system of ordinary differential equations,

$$\frac{d\psi}{dt} = \mathbf{f}(t, \psi), \quad (39)$$

the Runge-Kutta method expresses the solution at a next time-step, ψ^{n+1} , as the sum of the current solution ψ^n and a linear combination of a set of corrections, \mathbf{k}_i . The corrections are found by solving

$$\begin{aligned} \mathbf{k}_1 &= h\mathbf{f}(t^n, \psi^n) \\ \mathbf{k}_2 &= h\mathbf{f}(t^n + a_2 h, \psi^n + b_{21}\mathbf{k}_1) \\ &\dots \\ \mathbf{k}_6 &= h\mathbf{f}(t^n + a_6 h, \psi^n + b_{61}\mathbf{k}_1 + b_{62}\mathbf{k}_2 \dots + b_{65}\mathbf{k}_5), \end{aligned} \quad (40)$$

where h denotes the step-size. Next, a fifth-order and a fourth-order accurate estimate of the solution are found as:

$$\psi^{n+1} = \psi^n + \sum_{i=1}^6 c_i \mathbf{k}_i + \mathcal{O}(h^6) \quad (41)$$

and

$$\tilde{\psi}^{n+1} = \psi^n + \sum_{i=1}^6 c_i^* \mathbf{k}_i + \mathcal{O}(h^5). \quad (42)$$

The constants a_i , b_{ij} , c_i and c_i^* in the above equations are given in Table 1. Adaptive step-size control is accomplished by employing an error estimate based on the latter two constants,

$$\epsilon = \psi^{n+1} - \tilde{\psi}^{n+1} = \sum_{i=1}^6 (c_i - c_i^*) \mathbf{k}_i, \quad (43)$$

following a strategy proposed by Press *et al.* [44]:

$$h_{\text{next}} = \begin{cases} S h_{\text{try}} \left| \frac{\epsilon_{\text{next}}}{\epsilon_{\text{try}}} \right|^a & \text{if } \epsilon_{\text{next}} \geq \epsilon_{\text{try}} \\ S h_{\text{try}} \left| \frac{\epsilon_{\text{next}}}{\epsilon_{\text{try}}} \right|^b & \text{if } \epsilon_{\text{next}} < \epsilon_{\text{try}} \end{cases}. \quad (44)$$

Here, ϵ_{next} denotes the desired accuracy, ϵ_{try} the accuracy of the “worst offender” equation, $S=0.9$, $a=1/5$, and $b=1/4$. The reader may consult to Press *et al.* for the precise motivation of this strategy and further implementation details.

Like an explicit Runge-Kutta method, a Rosenbrock method also expresses the solution at a next time step as the sum of the solution at the current time step and a linear combination of corrections. For the system (39), these corrections are found by solving the implicit

Table 1. Parameters for Runge-Kutta Method

i	a_i	b_{ij}					c_i	c_i^*
1							37/378	2825/27648
2	1/5	1/5					0	0
3	3/10	3/40	9/40				250/621	18575/48384
4	3/5	3/10	-9/10	6/5			125/594	13525/55296
5	1	-11/54	5/2	-70/27	35/27		0	277/14336
6	7/8	1631/55296	175/512	575/13824	44275/110592	253/4096	512/1771	1/4
$j =$		1	2	3	4	5		

Table 2. Problem independent constants γ , c_i , α_{ij} and γ_{ij} of the Rosenbrock method

	$\gamma = 0.395$ (Kaps & Rentrop)	$\gamma = 0.231$ (Kaps & Rentrop)	$\gamma = 1/2$ (Shampine)
γ_{21}	-0.767672395484	-0.270629667752	-4
γ_{31}	-0.851675323742	0.311254483294	186/25
γ_{32}	0.522967289188	0.852445628482·10 ⁻²	6/5
γ_{41}	0.288463109545	0.282816832044	-56/125
γ_{42}	0.880214273381·10 ⁻¹	-0.457959483281	-27/125
γ_{43}	-0.337389840627	-0.111208333333	-1/5
α_{21}	0.438	0.462	1
α_{31}	0.796920457938	-0.815668168327·10 ⁻¹	24/25
α_{32}	0.730795420615·10 ⁻¹	0.961775150166	3/25
b_2	—	—	1
b_3	—	—	3/5
b_4	—	—	3/5
β_1	—	—	1/2
β_2	—	—	-3/2
β_3	—	—	121/50
β_4	—	—	29/250
3^{rd} -order accuracy			
c_1	0.346325833758	-0.717088504499	98/108
c_2	0.285693175712	0.177617912176·10 ⁺¹	11/72
c_3	0.367980990530	-0.590906172617·10 ⁻¹	25/216
4^{th} -order accuracy			
c_1	0.199293275701	0.217487371653	19/18
c_2	0.482645235674	0.486229037990	1/4
c_3	0.680614886256·10 ⁻¹	0.0	25/216
c_4	0.25	0.296283590357	125/216

system:

$$\left[\mathbf{I} - \gamma h \frac{\partial \mathbf{f}}{\partial \boldsymbol{\psi}} \Big|_{\boldsymbol{\psi}^n} \right] \cdot \mathbf{k}_i = h \mathbf{f} \left(\boldsymbol{\psi}^n + \sum_{j=1}^{i-1} \alpha_{ij} \mathbf{k}_j \right) + h \frac{\partial \mathbf{f}}{\partial \boldsymbol{\psi}} \Big|_{\boldsymbol{\psi}^n} \cdot \sum_{j=1}^{i-1} \gamma_{ij} \mathbf{k}_j \quad i = 1 \dots s, \quad (45)$$

where γ , c_i , α_{ij} and γ_{ij} are problem independent constants. Their values are summarized in Table 2. Two formulations could be found in the literature for the practical implementation of equation (45). For autonomous systems, Kaps & Rentrop [45] proposed to express the solution as

$$\boldsymbol{\psi}^{n+1} = \boldsymbol{\psi}^n + \sum_{i=1}^s c_i \mathbf{k}_i \quad (46)$$

and to obtain the corrections by restating equation (45) as:

$$\begin{aligned} \mathbf{E}_\psi \cdot \mathbf{k}_1 &= h \mathbf{f}(\boldsymbol{\psi}^n) \\ \mathbf{E}_\psi \cdot (\mathbf{k}_2 + \tilde{\gamma}_{21} \mathbf{k}_1) &= h \mathbf{f}(\boldsymbol{\psi}^n + \alpha_{21} \mathbf{k}_1) + \tilde{\gamma}_{21} \mathbf{k}_1 \\ \mathbf{E}_\psi \cdot (\mathbf{k}_3 + (\tilde{\gamma}_{31} \mathbf{k}_1 + \tilde{\gamma}_{32} \mathbf{k}_2)) &= h \mathbf{f}(\boldsymbol{\psi}^n + \alpha_{31} \mathbf{k}_1 + \alpha_{32} \mathbf{k}_2) + (\tilde{\gamma}_{31} \mathbf{k}_1 + \tilde{\gamma}_{32} \mathbf{k}_2) \\ \mathbf{E}_\psi \cdot (\mathbf{k}_4 + (\tilde{\gamma}_{41} \mathbf{k}_1 + \tilde{\gamma}_{42} \mathbf{k}_2 + \tilde{\gamma}_{43} \mathbf{k}_3)) &= h \mathbf{f}(\boldsymbol{\psi}^n + \alpha_{31} \mathbf{k}_1 + \alpha_{32} \mathbf{k}_2) \\ &\quad + (\tilde{\gamma}_{41} \mathbf{k}_1 + \tilde{\gamma}_{42} \mathbf{k}_2 + \tilde{\gamma}_{43} \mathbf{k}_3), \end{aligned} \quad (47)$$

where $\tilde{\gamma}_{ij} = \gamma_{ij}/\gamma$. For more general systems involving partial derivatives of the right hand side of equation (39) with respect to t , Shampine [36] proposed to express the solution as

$$\boldsymbol{\psi}^{n+1} = \boldsymbol{\psi}^n + h \sum_{i=1}^s c_i \mathbf{k}_i \quad (48)$$

and to find the corrections by solving:

$$\begin{aligned} \mathbf{E}_\psi \cdot \mathbf{k}_1 &= \mathbf{f}(t^n, \boldsymbol{\psi}^n) + \beta_1 h \mathbf{E}_t \\ \mathbf{E}_\psi \cdot \mathbf{k}_2 &= \mathbf{f}(t^n + b_2 h, \boldsymbol{\psi}^n + \alpha_{21} h \mathbf{k}_1) + \gamma_{21} \mathbf{k}_1 + \beta_2 h \mathbf{E}_t \\ \mathbf{E}_\psi \cdot \mathbf{k}_3 &= \mathbf{f}(t^n + b_3 h, \boldsymbol{\psi}^n + \alpha_{31} h \mathbf{k}_1 + \alpha_{32} h \mathbf{k}_2) + \gamma_{31} \mathbf{k}_1 + \gamma_{32} \mathbf{k}_2 + \beta_3 h \mathbf{E}_t \\ \mathbf{E}_\psi \cdot \mathbf{k}_4 &= \mathbf{f}(t^n + b_4 h, \boldsymbol{\psi}^n + \alpha_{31} h \mathbf{k}_1 + \alpha_{32} h \mathbf{k}_2) + \gamma_{41} \mathbf{k}_1 + \gamma_{42} \mathbf{k}_2 + \gamma_{43} \mathbf{k}_3 + \beta_4 h \mathbf{E}_t \end{aligned} \quad (49)$$

In the preceding equations,

$$\mathbf{E}_\psi = \left[\mathbf{I} - \gamma h \frac{\partial \mathbf{f}}{\partial \boldsymbol{\psi}} \Big|_{\boldsymbol{\psi}^n} \right] \quad \text{and} \quad \mathbf{E}_t = \frac{\partial \mathbf{f}}{\partial t} \Big|_{(t^n, \boldsymbol{\psi}^n)} \quad (50)$$

Automatic step-size adjustment was accomplished using the strategy by Press *et al.* [44], i.e. equation (44), with $a=1/4$ and $b=1/3$. The linear systems constituted by each equation of system (49) were solved by means of LU-decomposition and back-substitution using the routines `ludcmp` and `lubksb` by the same authors.

As expected, the Runge-Kutta method turned out to be the least efficient on the first two test problems. On the first problem, for example, more than ten million function evaluations were necessary to compute the solution over a fraction ($0-10^{-3}$) of the whole integration domain ($0-10^8$). Assuming that the computational cost remains the same, this implies that about 10^{18} function evaluations would be required for the entire problem. On the third

problem, however, the LSODE implementation of the Adams-Moulton and Gear methods suffered a corrector convergence error on the first time-step, while Runge-Kutta method progressed further until the stepsize adjustment strategy was rendered useless by the onset and subsequent growth of numerical instability.

In all test-cases the Rosenbrock method was seen to be more efficient than the LSODE implementation of the Adams-Moulton and Gear methods in terms of time steps, function evaluations and Jacobian matrix evaluations. Because the first two problems are stiff and knowing that the Adams-Moulton method is intended for non-stiff problems while the Gear method is meant for stiff ones, it would be reasonable to expect that the former would be outperformed by the latter. This expectation was confirmed by the test results of the first problem, but not by those of the second problem. In the first problem both Gear methods (second and fifth order) outperformed the Adams-Moulton methods. With the second problem the opposite appears to have happened: both Gear methods were outperformed by the second order Adams-Moulton method. It is also seen that the accuracy of the Adams-Moulton method does not improve with increasing order. In the first problem, for example, an increase in the order from two to five makes the method more demanding by a factor of about a hundred in terms of time-steps, function evaluations and Jacobian matrix computations. In the second problem, it is seen that, while the number of Jacobian matrix computations remain almost the same, more than twice the initial number of time-steps and function evaluations are required to achieve the same accuracy.

Table 3. Comparison of methods

Problem A						
	ϵ_{rel}	nsteps	nfunc	njac	h_0	interval
Runge-Kutta (5 th -order)	10^{-4}	1833759	10679149	0	10^{-15}	[0.0– 10^{-3}]
[†] Adams-Moulton (2 nd -order)	10^{-4}	3515	3988	208	10^{-5}	[0.0– 10^8]
[†] Adams-Moulton (5 th -order)	10^{-4}	355852	384072	17862	10^{-5}	[0.0– 10^8]
[†] Gear (2 nd -order)	10^{-4}	601	696	72	10^{-5}	[0.0– 10^8]
[†] Gear (5 th -order)	10^{-4}	346	422	70	10^{-5}	[0.0– 10^8]
[‡] Gear (variable-order)	10^{-4}	289	376	71	10^{-5}	[0.0– 10^8]
Rosenbrock (4 th -order)	10^{-4}	81	243	81	10^{-5}	[0.0– 10^8]
Problem B						
	ϵ_{rel}	nsteps	nfunc	njac	h_0	interval
Runge-Kutta (5 th -order)	10^{-4}	55166	321259	0	$2.9 \cdot 10^{-4}$	[0.0–50.0]
[†] Adams-Moulton (2 nd -order)	10^{-4}	69	86	22	$2.9 \cdot 10^{-4}$	[0.0–50.0]
[†] Adams-Moulton (5 th -order)	10^{-4}	151	217	23	$2.9 \cdot 10^{-4}$	[0.0–50.0]
[†] Gear (2 nd -order)	10^{-4}	90	108	25	$2.9 \cdot 10^{-4}$	[0.0–50.0]
[†] Gear (5 th -order)	10^{-4}	87	108	21	$2.9 \cdot 10^{-4}$	[0.0–50.0]
[‡] Gear (variable-order)	10^{-4}	73	97	31	$2.9 \cdot 10^{-4}$	[0.0–50.0]
Rosenbrock (4 th -order)	10^{-4}	28	84	28	$2.9 \cdot 10^{-4}$	[0.0–50.0]
Problem C						
	ϵ_{rel}	nsteps	nfunc	njac	h_0	interval
Runge-Kutta (5 th -order)	10^{-4}	829896	4832925	0	10^{-15}	[0.0– 10^{-5}]
[†] Adams-Moulton (2 nd ,5 th -order)		corrector convergence error!			10^{-15}	—
[†] Gear (2 nd ,5 th -order)		corrector convergence error!			10^{-15}	—
[‡] Gear (variable-order)	10^{-4}	169	267	72	10^{-15}	[0.0– 10^4]
Rosenbrock (4 th -order)	10^{-4}	130	390	130	10^{-15}	[0.0– 10^4]

[†] LSODE/CHEMKIN II.

[‡] VODE/CHEMKIN III, without Jacobian saving strategy, calculation performed by L.M.T. Somers from Eindhoven Univ.

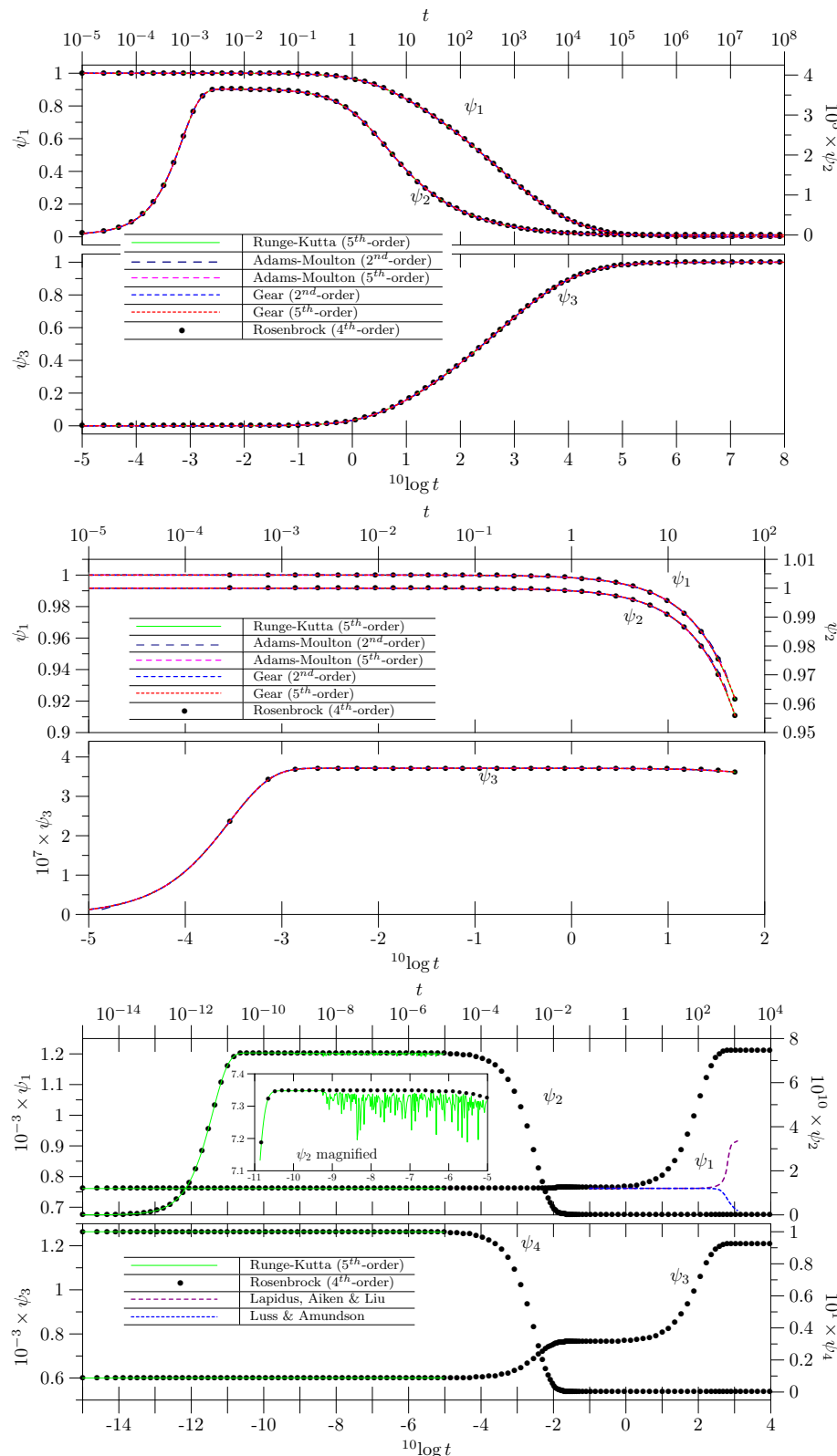


Figure 4. Top: Problem D2 by Enright & Pryce [28], Middle: Problem D4 by Enright & Pryce [28], Bottom: Problem F1 by Enright & Pryce [28].

In order to find out whether the under-performance of the backward differentiation formulas was inherent to their nature or due to their implementation and stepsize control strategy, it was decided to apply a different implementation (VODE) to the test problems. Only the Gear method was selected and applied without a Jacobian saving strategy. The performance is compared in terms of the number of time steps, Jacobian and function evaluations. On the first test problem, the Rosenbrock method requires 14% more Jacobian evaluations, but at the same time 20% less function evaluations and 72% fewer time steps. On the second problem the Rosenbrock method is seen to outperform the variable-order Gear method in terms of time steps, function evaluations and Jacobian evaluations. the number of Jacobian and function evaluations is about the same with both methods. In the third problem, the Rosenbrock method is outperformed by the Gear method: the latter requires 32% fewer function evaluations and 45% fewer Jacobian evaluations, although the number of time steps appears to be 30% larger.

6 Application of Least-squares gradient reconstruction in conjunction with the Runge-Kutta method to a three-dimensional diffusion problem

As stated in the Introduction, the diffusion equation,

$$\frac{\partial c(x, y, z, t)}{\partial t} = \mathbb{D} \left[\frac{\partial^2 c(x, y, z, t)}{\partial x^2} + \frac{\partial^2 c(x, y, z, t)}{\partial y^2} + \frac{\partial^2 c(x, y, z, t)}{\partial z^2} \right], \quad (51)$$

was solved numerically on the three-dimensional cartesian unstructured mesh shown in Figure 5 for the problem of an instantaneous spherical surface source. A fixed amount M ($= 1$ kg) of a substance is equally distributed and suddenly released over a concentric spherical surface of a radius r_0 ($= 2$ cm), within a spherical domain of a radius R ($= 3$ cm). The diffusion coefficient of the species in the medium is denoted by \mathbb{D} ($= 10^{-5}$ m 2 s $^{-1}$). Since the diffusion process is radial, equation (51) may be restated in a simplified form using spherical coordinates,

$$\frac{\partial c(r, t)}{\partial t} = \mathbb{D} \frac{1}{r^2} \frac{\partial}{\partial r} \left[r^2 \frac{\partial c(r, t)}{\partial r} \right], \quad (52)$$

where the radial coordinate r denotes the distance of an arbitrary point in space from the common center of the spherical surface source and the spherical domain. For a zero Neumann condition on the boundary of the domain, Carslaw and Jaeger [46] provide the following analytical solution:

$$c(r, t) = \frac{3}{4\pi R^3} + \frac{1}{2\pi R r_0 r} \sum_{n=1}^{\infty} \left(1 + \frac{1}{R^2 \alpha_n^2} \right) \sin(r\alpha_n) \sin(r_0\alpha_n) \exp(-\mathbb{D}\alpha_n^2 t), \quad (53)$$

where the α_n are the positive roots of

$$\tan(R\alpha_n) - R\alpha_n = 0. \quad (54)$$

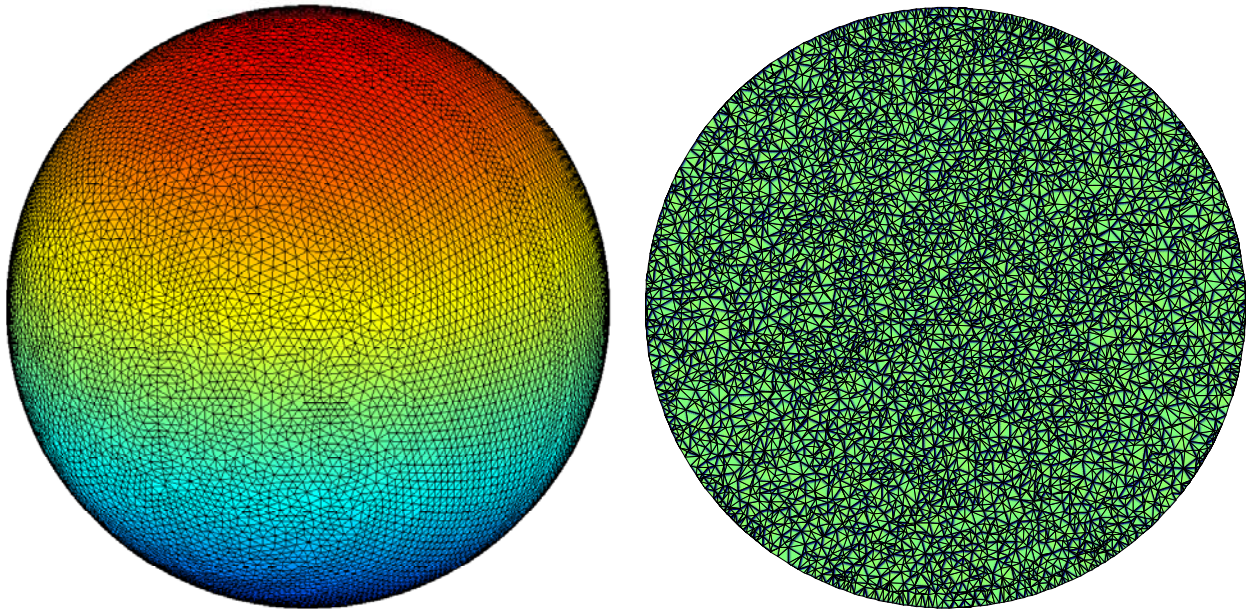


Figure 5. The surface mesh (left) and a plane intersection at $z=0$ of the volume mesh (right) of the spherical domain.

The analytical solution and the second order spatial derivative, as it appears on the right hand side of equation (52),

$$\frac{1}{r^2} \frac{\partial}{\partial r} \left[r^2 \frac{\partial c(r, t)}{\partial r} \right] = -\frac{1}{2\pi R r_0 r} \sum_{n=1}^{\infty} \alpha_n^2 \left(1 + \frac{1}{R^2 \alpha_n^2} \right) \sin(r\alpha_n) \sin(r_0\alpha_n) \exp(-\mathbb{D}\alpha_n^2 t) \quad (55)$$

are shown in Figure 6.

The problem of an instantaneous spherical surface source was simulated by imposing equation (53) with $t = 0.4$ s as the initial condition. Solutions at later times were calculated by integrating the spatial derivatives using the fifth-order Runge-Kutta method described in the previous section. Instead of adaptive step-sizing, stability was ensured by fixing the time-step at a tenth of

$$h_{\text{diff}} = \frac{\Delta^2}{\beta \mathbb{D}} \quad (56)$$

where Δ denotes the shortest distance between a face and its opposite vertex, and $\beta = 6$. The value of β was taken following pages 343–344 by Hirsch [47], who suggests that $\beta \geq 6$ for an explicit second order discretization, instead of $\beta \geq 2$, arising from the Von Neumann stability analysis. A conservative step-size constraint was imposed to ensure that no oscillations would arise due to numerical instability of the time-integration scheme. These would mistakenly be attributed to the application of the Green-Gauss theorem. The motivation for the severeness of the time constraint was that, while least-squares gradient reconstruction involving equation (30), up to the tenth term, is second order accurate, the accuracy associated with the Green-Gauss theorem is not unique because of the arbitrariness in the number of cells composing a vertex-based control volume. The spatial derivatives were calculated in two distinct ways:

- (i) The discrete Green-Gauss theorem was applied twice, once to get the first derivatives, and once more to obtain the second derivatives from the first derivatives, while the

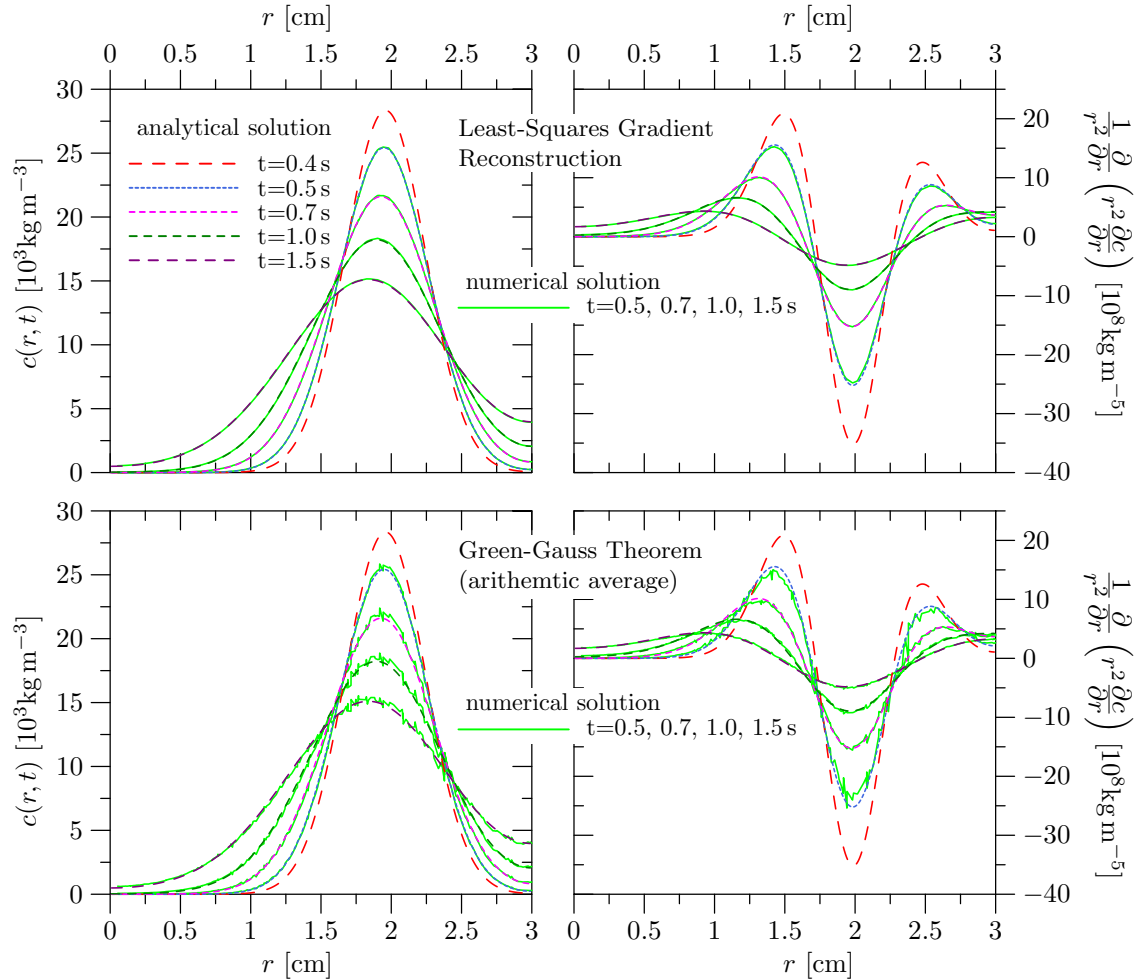


Figure 6. Comparison between the numerical and the analytical solution.

average value at the face was calculated by means of equation (4). The numerical solution and the numerical derivatives at consecutive times of 0.5, 0.7, 1.0, and 1.5 seconds are shown in the lower part of Figure 6.

- (ii) Equation (30), up to the ninth term, was least-squares fitted to sufficient nearby neighbors (at least nine) of the j -th nodal point with the spatial derivatives as degrees of freedom. The nearby neighbors are chosen such that the parent node is enclosed by a convex hull of faces of equal topological proximity. For, example, when the j -th parent node is surrounded by nine or more first-level neighbor nodes, only these are used in the least-squares fitting. When the parent node is surrounded by less than nine first-level neighbor nodes, all second-level neighbors are included as well, and this continues with still higher neighbors until redundancy is ruled out. The numerical solution and derivatives are shown in the upper part of Figure 6.

The lower part of Figure 6 shows that the application of the Green-Gauss theorem with the arithmetic mean as the average value at the face inevitably leads to high frequency oscillations in the numerical spatial derivatives and hence in the numerical solution. The upper part of the figure shows that this oscillation is absent when least-squares gradient reconstruction is applied. Moreover, with the latter method better agreement may be observed between the numerical and the analytical solution. With the least-squares gradient reconstruction

method being second order accurate in the present application, this observation implies that the Green-Gauss theorem has a spatial accuracy of less than second order when the average value at the cell faces is computed according to equation (4). According to equation (9) this accuracy can be no more than first order.

7 Application of least-squares gradient reconstruction in conjunction with the Rosenbrock method to the one-dimensional Euler equations involving exothermic chemical reaction

7.1 Time-marching schemes

The idea of combining least-squares gradient reconstruction with a Rosenbrock method was inspired by the fact that explicit time-marching algorithms are considered to be the method of choice for the computation of compressible flows. Jameson, Baker & Weatherhill [48] have demonstrated that flow fields around complex geometries can be computed by solving the Euler equations on an unstructured tetrahedral mesh with an explicit four-stage Runge-Kutta method. This approach was extended by Dawes [49, 50] to handle the full three-dimensional, compressible, Reynolds-averaged Navier-Stokes equations with $k - \epsilon$ turbulence modelling on an unstructured mesh. The potential of the extended method was demonstrated by resolving the flow field in turbomachinery. Time-marching was accomplished by an explicit two-step Runge-Kutta algorithm with residual smoothing [51]. The accuracy was improved by implementing solution adaptive mesh refinement in regions that were judged to need it, and by low Reynolds number damping of the eddy viscosity following Lam & Bremhorst [52].

In a later contribution, Watterson, Connell, Savill & Dawes [53] extended the approach to handle a transient flame front in the course of a confined explosion. The ability to refine and coarsen the mesh dynamically was employed to resolve moving flow features such as flame fronts and wakes passing through the computational domain. The simplest possible combustion modelling [54] was implemented by incorporating an additional transport equation for a reaction progress variable with its source term described by an eddy-breakup model. This development was taken further by Birkby, Cant & Savill [55], in an attempt to overcome deficiencies of the combustion model, such as its insensitivity to mixture composition and fuel type and the inability to predict correct burning rates near walls. An additional transport equation for the mixture fraction was included to allow for non-uniform initial fuel distributions. The source term of the reaction progress variable was modelled as being the product of the laminar burning velocity and a flame surface density. The flame surface density was expressed in terms of a turbulent flame thickness, which in turn depends on the turbulence intensity, the laminar burning velocity, and the laminar flame thickness. The use of computationally expensive flamelet libraries was avoided by employing an empirical correlation which expresses the laminar burning velocity as a function of chemical composition, pressure and temperature.

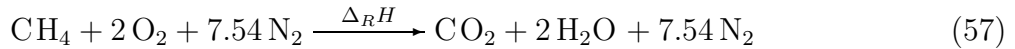
Despite demonstrations of the ability of explicit time-marching methods to deal with challenging problems involving compressible flows, their application to low subsonic Mach number flows remains a matter of concern. This concern stems from the fact that the convective terms of the equations describing fluid flow become stiff when the flow speed is

comparatively small with respect to the sonic velocity. When the velocity of the entire flow field is low, compressibility effects become negligible, and difficulties arising from stiffness are averted by switching to the incompressible equations describing fluid flow. In these situations pressure based algorithms have become the method of choice. The most widely applied pressure based algorithms combine the finite volume method with a segregated solution strategy and pressure-velocity coupling involving a pressure correction equation [56–60]. However, a large number of flow problems, like high-speed flows with embedded regions of low velocity, or, low-speed flows with temperature differences caused by strong heat addition, involve low Mach number regions as well as decidedly compressible ones. In such cases compressible equations have to be used throughout the entire computational domain and the stiffness arising from the convective terms must be dealt with.

The various attempts made to extend compressible schemes to handle low-subsonic regions may be categorized as those relying on the pseudo-compressibility concept [61–65], those which use a perturbed form of the governing equations, such that physical acoustic waves are replaced by pseudo-acoustic modes whose speeds are comparable to the particle velocity [66–69], and those which pre-multiply the time-derivative by a matrix that scales the eigenvalues to the same order of magnitude [70]. All these methods have in common that they rest on a mathematical treatment of the governing equations so that conventional time-integration methods become suitable for the time-marching process. Attempts to extend time-marching procedures by using a stiff integration method instead of conventional ones whose success or failure depends on a mathematical pre-treatment of the governing equations, are unknown to the present authors. With this in mind, it was decided to combine the least-squares gradient reconstruction method with the Shampine implementation of the Rosenbrock method and to apply it to the Euler equations with an exothermic chemical reaction present.

7.2 Position of the problem

A gas mixture composed of methane (CH_4), oxygen (O_2) and nitrogen (N_2) enters a one-dimensional domain, $x_L \leq x \leq x_R$, from the left side with a velocity v_x^o . Carbon dioxide (CO_2) and water (H_2O) are being produced by the exothermic chemical reaction



whereby the total amount of molecules remains conserved. The amount of heat released per mass unit of CH_4 is denoted by $\Delta_R H$. The reactant mixture is assumed to be stoichiometric so that the product mixture consists of CO_2 , H_2O and N_2 only. The governing equations

describing the problem are taken to be the reactive Euler equations

$$\frac{\partial \rho}{\partial t} + \frac{\partial}{\partial x} [\rho v_x] = 0 \quad (58)$$

$$\frac{\partial (\rho v_x)}{\partial t} + \frac{\partial}{\partial x} [p + \rho v_x v_x] = 0 \quad (59)$$

$$\frac{\partial (\rho Y_1)}{\partial t} + \frac{\partial}{\partial x} [\rho v_x Y_1] = \omega_{Y_1} \quad (60)$$

$$\frac{\partial (\rho Y_2)}{\partial t} + \frac{\partial}{\partial x} [\rho v_x Y_2] = \omega_{Y_2} \quad (61)$$

...

$$\frac{\partial (\rho Y_{N_s})}{\partial t} + \frac{\partial}{\partial x} [\rho v_x Y_{N_s}] = \omega_{Y_{N_s}} \quad (62)$$

$$\frac{\partial (\rho E_t)}{\partial t} + \frac{\partial}{\partial x} [pv_x + \rho v_x E_t] = \omega_Q + \omega_R \quad (63)$$

where

$$p = (\gamma - 1)[\rho E_t - \frac{1}{2}\rho v_x^2], \quad (64)$$

and $\omega_{Y_1}, \omega_{Y_2}, \dots, \omega_{Y_{N_s}}$ denoting the chemical source terms, ω_Q an external heat source, and ω_R the heat release rate due to the exothermic chemical reaction (57). The chemical source terms are modelled as

$$\omega_{Y_1} = \frac{\mathcal{M}_2}{\mathcal{M}_1} \frac{\nu''_2 - \nu'_2}{\nu'_1 - \nu'_1} \omega_{Y_2} = \dots = \frac{\mathcal{M}_{N_s}}{\mathcal{M}_1} \frac{\nu''_{N_s} - \nu'_{N_s}}{\nu'_1 - \nu'_1} \omega_{Y_{N_s}} = -A\rho^{m+n} Y_1^m Y_2^n \exp(-E_a/RT), \quad (65)$$

where $A = 2.87 \cdot 10^{15} \text{ kg}^{1-m-n} \text{ m}^{-3(1-m-n)} \text{ s}^{-1}$, $m = 2.8$, $n = 1.2$, and $E_a = 1.38 \cdot 10^5 \text{ J mol}^{-1} \text{ K}^{-1}$ [71]. The stoichiometric coefficients of the reactant and product mixture are $\nu'_1 = \nu'_{\text{CH}_4} = 1$, $\nu'_2 = \nu'_{\text{O}_2} = 2$, $\nu'_3 = \nu'_{\text{N}_2} = 7.54$, $\nu'_4 = \nu'_{\text{CO}_2} = 0$, $\nu'_5 = \nu'_{\text{H}_2\text{O}} = 0$ and $\nu''_1 = \nu''_{\text{CH}_4} = 0$, $\nu''_2 = \nu''_{\text{O}_2} = 0$, $\nu''_3 = \nu''_{\text{N}_2} = 7.54$, $\nu''_4 = \nu''_{\text{CO}_2} = 1$, $\nu''_5 = \nu''_{\text{H}_2\text{O}} = 2$, respectively. The corresponding molecular weights ($10^{-3} \text{ kg mole}^{-1}$) are $\mathcal{M}_1 = \mathcal{M}_{\text{CH}_4} = 16$, $\mathcal{M}_2 = \mathcal{M}_{\text{O}_2} = 32$, $\mathcal{M}_3 = \mathcal{M}_{\text{N}_2} = 28$, $\mathcal{M}_4 = \mathcal{M}_{\text{CO}_2} = 44$, and $\mathcal{M}_5 = \mathcal{M}_{\text{H}_2\text{O}} = 18$. The heat source term ω_R due to chemical reaction is modelled as the product of the fuel consumption rate and the heat of reaction,

$$\omega_R = \omega_{Y_1} \Delta_R H, \quad (66)$$

with $\Delta_R H = -5.0 \cdot 10^7 \text{ J kg}^{-1}$. Further in this section (Subsection 7.4) a problem shall be considered where the reactive mixture is distorted by a transient heat source. This, to explore the feasibility of using least-squares gradient reconstruction combined with the Rosenbrock method for stiff integration as a time marching scheme, and, to verify the implementation of non-reflecting boundary conditions, to be discussed in the next subsection.

7.3 Non-reflecting boundary conditions

A particular feature of equations (58) to (64) is that, while they express a change in the conserved quantities, $\rho, \rho v_x, \rho Y_1, \rho Y_2, \dots, \rho Y_{N_s}, \rho E_t$, in terms of fluxes and sources, they also constitute a complete wave description. This implies that any spatial non-uniformity (i.e. when the first derivative is nonzero) of the physical quantities has the tendency to propagate in space while preserving its initial waveform. Moreover, every non-uniformity, at any instant

of time, behaves as a propagating initial waveform. When this behavior is not accounted for, high-frequency instabilities arising from discretization errors are propagated as numerical waves through the computational domain. These are reflected at the boundaries and combine with newly generated instabilities within the domain to form numerical waves of an ever increasing amplitude and wavelength. Without proper treatment at the boundaries, this process may render the solution useless.

The accumulation of instabilities was addressed by various authors [72–75] and boundary conditions based on so called local one-dimensional inviscid relationships have been introduced to deal with the problem. This formulation relies on a fundamental difference between the transport of a quantity by a flux, and, the propagation of variations in its magnitude as a wave. The transport of the conserved quantities by convective fluxes is always coupled with the transport of matter from one point in space to another. When an initial waveform of the same quantities propagates through space, this happens without the transport of matter. Even when the physical quantity concerns the density, it is only the shape which is being “transported”. Not the quantity itself. With this in mind, and knowing that every realization of a physical quantity has a tendency to propagate itself through space with a group velocity belonging to the characteristics, it becomes possible to manipulate and control the shape of the waveform at the boundaries, such that numerical waves are no longer reflected back into the domain.

The wave description becomes apparent when equation (64) is first substituted into equations (59) and (63) so that the conservation form of the governing equations becomes,

$$\frac{\partial \rho}{\partial t} + \frac{\partial}{\partial x} [\rho v_x] = 0 \quad (67)$$

$$\frac{\partial (\rho v_x)}{\partial t} + \frac{\partial}{\partial x} [(\gamma - 1)\rho E_t - \frac{1}{2}(\gamma - 3)\rho v_x^2] = 0 \quad (68)$$

$$\frac{\partial (\rho Y_1)}{\partial t} + \frac{\partial}{\partial x} [\rho v_x Y_1] = \omega_{Y_1} \quad (69)$$

$$\frac{\partial (\rho Y_2)}{\partial t} + \frac{\partial}{\partial x} [\rho v_x Y_2] = \omega_{Y_2} \quad (70)$$

...

$$\frac{\partial (\rho Y_{N_s})}{\partial t} + \frac{\partial}{\partial x} [\rho v_x Y_{N_s}] = \omega_{Y_{N_s}} \quad (71)$$

$$\frac{\partial (\rho E_t)}{\partial t} + \frac{\partial}{\partial x} [\gamma \rho v_x E_t - \frac{1}{2}(\gamma - 1)\rho v_x^3] = \omega_Q + \omega_R \quad (72)$$

or, equivalently,

$$\frac{\partial \mathbf{U}}{\partial t} + \frac{\partial \mathbf{F}}{\partial x} = \boldsymbol{\omega} \quad (73)$$

where

$$\mathbf{F} = [\rho v_x, (\gamma - 1)\rho E_t - \frac{1}{2}(\gamma - 3)\rho v_x^2, \rho v_x Y_1, \rho v_x Y_2, \dots, \rho v_x Y_{N_s}, \gamma \rho v_x E_t - \frac{1}{2}(\gamma - 1)\rho v_x^3] \quad (74)$$

$$\mathbf{U} = [\rho, \rho v_x, \rho Y_1, \rho Y_2, \dots, \rho Y_{N_s}, \rho E_t]. \quad (75)$$

By the chain rule,

$$\frac{\partial \mathbf{F}}{\partial x} = \left[\frac{\partial \mathbf{F}}{\partial \mathbf{U}} \right] \cdot \frac{\partial \mathbf{U}}{\partial x} = \mathbf{A} \cdot \frac{\partial \mathbf{U}}{\partial x} \quad (76)$$

equation (73) assumes a quasi-linear conservation form,

$$\frac{\partial \mathbf{U}}{\partial t} + \mathbf{A} \cdot \frac{\partial \mathbf{U}}{\partial x} = \boldsymbol{\omega} \quad (77)$$

with \mathbf{A} denoting the flux-Jacobian. Because equations (74) and (75) are connected by the transformation

$$\begin{aligned} F_1 &= U_2 \\ F_2 &= (\gamma - 1)U_{3+N_s} - \frac{1}{2}(\gamma - 3)U_2^2/U_1 \\ F_3 &= U_2U_3/U_1 \\ F_4 &= U_2U_4/U_1 \\ &\dots \\ F_{N_s} &= U_2U_{2+N_s}/U_1 \\ F_{3+N_s} &= \gamma U_2U_{3+N_s}/U_1 - \frac{1}{2}(\gamma - 1)U_2^3/U_1^2, \end{aligned} \quad (78)$$

the flux jacobian becomes

$$\mathbf{A} = \frac{\partial \mathbf{F}}{\partial \mathbf{U}} = \left[\begin{array}{cccccc} 0 & 1 & 0 & 0 & \cdot & 0 & 0 \\ \frac{1}{2}(\gamma - 3)v_x^2 & (3 - \gamma)v_x & 0 & 0 & \cdot & 0 & \gamma - 1 \\ -v_xY_1 & Y_1 & v_x & 0 & \cdot & 0 & 0 \\ -v_xY_2 & Y_2 & 0 & v_x & \cdot & 0 & 0 \\ \cdot & \cdot & \cdot & \cdot & \cdot & \cdot & \cdot \\ -v_xY_{N_s} & Y_{N_s} & 0 & 0 & \cdot & v_x & 0 \\ \frac{1}{2}(\gamma - 2)v_x^3 - \frac{1}{\gamma - 1}v_xc^2 & -\frac{1}{2}(2\gamma - 3)v_x^2 + \frac{1}{\gamma - 1}c^2 & 0 & 0 & \cdot & 0 & \gamma v_x \end{array} \right], \quad (79)$$

where the sonic velocity c depends on the total energy E_t according to

$$c^2 = \gamma(\gamma - 1) [\gamma E_t - \frac{1}{2}v_x^2]. \quad (80)$$

Notice that the preceding expression results from combining equation (64) with the definition of the sonic velocity, $c^2 = \gamma RT = \gamma p/\rho$. The system (77) constitutes a complete wave description when it is hyperbolic, and, it is hyperbolic when there exists a matrix \mathbf{Q} such that

$$\mathbf{Q}^{-1} \cdot \mathbf{A} \cdot \mathbf{Q} = \boldsymbol{\Lambda}, \quad (81)$$

where $\boldsymbol{\Lambda}$ denotes a diagonal matrix containing only real eigenvalues of \mathbf{A} , \mathbf{Q} denotes a matrix whose columns are right eigenvectors of \mathbf{A} , and, \mathbf{Q}^{-1} is a matrix whose rows are left eigenvectors of \mathbf{A} . It is sufficient to mention here that such a matrix exists and its precise form is given in Appendix A.

Because of the hyperbolic nature of system (77), each point of the computational domain contains a set of left and right running waves with velocities equal to the eigenvalues (121) of the flux Jacobian. On the boundary, this implies that waves are leaving and entering the domain. Inside the domain, the solution may be computed by time integration of the system (77) because the wave amplitude variations are completely determined by information at neighboring points. At the boundary nodes, however, an auxiliary system in terms of wave amplitude variations has to be solved. The need for an auxiliary system appears to be threefold.

Firstly, there is the problem of a conflict between the specification of boundary conditions and the Riemann invariants. This becomes evident by considering what might happen to the Riemann invariants (133) when boundary conditions have to be enforced within the context of the subsonic inflow in the present problem. By judging equations (58) to (64), it would be tempting to specify Dirichlet conditions for the set $\{\rho, v_x, Y_1, \dots, Y_{N_s}, p, T\}$ by imposing constant values on the boundary during the time integration process. However, inspection of the Riemann invariants, (133) and (226), shows that this results in a conflict. Specifying $\{d\rho, dv_x, dY_1, \dots, dY_{N_s}, dp\}$ or $\{d\rho, dv_x, dY_1, \dots, dY_{N_s}, dT\}$ leads to a conflict with the first member of the Riemann invariant sets because $d\rho$ is determined by the interior flow, while dp and dv_x on the right hand side are fixed. When all these quantities are clamped to a fixed value, there will be a discrepancy between their magnitude and time-dependent information carried by the $v_x - c$ characteristic from within the domain towards the boundary. This results in the generation of non-physical wave amplitude variations.

Secondly, there is the issue of over- and under-specification of the boundary conditions. Imposing the full sets $\{d\rho, dv_x, dY_1, \dots, dY_{N_s}, dp\}$ or $\{d\rho, dv_x, dY_1, \dots, dY_{N_s}, dT\}$ leads to an over-specification according to (133) and (226), and a conflict with the first member of the Riemann invariant sets, as explained before. Focusing on the Riemann invariant set (133), this leaves $\{d\rho, dv_x, dY_1, \dots, dY_{N_s}\}$ or $\{d\rho, dY_1, \dots, dY_{N_s}, dp\}$ or $\{dv_x, dY_1, \dots, dY_{N_s}, dp\}$ as remaining possibilities. Smaller sets of boundary conditions constitute a degree of under-specification which definitely leads to ill-posedness. With the first set, $\{d\rho, dv_x, dY_1, \dots, dY_{N_s}\}$, it is seen that all members of (133) are fully specified, except for the first and last one, which are only partially specified (they retain dp as a degree of freedom). The second set, $\{d\rho, dY_1, \dots, dY_{N_s}, dp\}$, also fully specifies all members of (133), except for the first and last one, because they retain dv_x as a degree of freedom. The third set $\{dv_x, dY_1, \dots, dY_{N_s}, dp\}$ partially specifies the second member of (133) and fully specifies all other members. Because the first member is governed by the interior flow, and due to the absence of a degree of freedom to compensate the difference between the value at the boundary and information conveyed from the interior by the $v_x - c$ characteristic, this set leads to a conflict and must be discarded. Owing to the degree of freedom allowed by the first two sets in the first member of the Riemann invariants, these remain as suitable candidates to impose inflow boundary conditions.

Thirdly, there is a necessity for a mechanism to manipulate the wave amplitude variations. This, to overcome the hurdle of having to specify boundary conditions by constraining only the degrees of freedom in the Riemann invariants to prevent a conflict with information arriving from the interior of the domain, and at the same time, to avoid over- or under-specification of the boundary conditions. Such a mechanism is constituted by two seemingly different auxiliary systems, namely, equations (157) to (174) in Appendix B, and equations (189) and (206) in appendix C. Its derivation rests on the establishment of wave amplitude variations, see equation (148), whose magnitude is determined by information in terms of the primitive variables, i.e. (134) or (175), transmitted by the characteristics. The left hand side of the conservation form (77), is reformulated in terms of these wave amplitude variations, i.e. equations (158)–(162) and (190)–(194), and supplemented with additional relationships to implement Dirichlet and Neumann conditions, (163)–(174) and (195)–(206). At interior nodes, the conservation form is solved as usual. Boundary nodes are treated by solving the auxiliary system as follows.

The inflow boundary may be defined by imposing Dirichlet conditions on the members of the set $\{d\rho, dY_1, \dots, dY_{N_s}, dp\}$ through equations (163)–(168), and hence by constraining the

auxiliary system (158)–(162). To prevent information from being conveyed from the exterior towards the boundary by the v_x and $v_x + c$ characteristics, and to keep $\{\rho, Y_1, \dots, Y_{N_s}, p\}$ at a constant value at the same time, we set $\mathcal{L}_2 = 0, \mathcal{L}_3 = 0, \dots, \mathcal{L}_{N_s+2} = 0$ and $\mathcal{L}_{3+N_s} = \mathcal{L}_1$. \mathcal{L}_1 is computed from the interior flow using equation (149). When applied to the problem of the distortion by a transient heat source, described in the next subsection (see Figure 7), it is seen that all quantities, except v_x and ρv_x , remain constant at the inflow. A well-posed outflow boundary may be defined by imposing constant pressure at the right boundary of the domain. To prevent exterior information from entering the domain through the boundary by $v_x - c$ characteristic, while keeping p constant, we set $\mathcal{L}_1 = \mathcal{L}_{3+N_s}$. \mathcal{L}_{3+N_s} is computed from the interior flow using equation (155). All quantities at the outflow boundary (see Figure 7), except v_x and ρv_x , are seen to be constant. At later times (i.e. 80, 90, 100 μ s) these quantities are also seen to be reflected at both boundaries. As stated previously, this behavior may result in an unacceptable accumulation of discretization errors. To prevent this from happening it becomes necessary to implement non-reflecting boundary conditions.

Non-reflecting inflow conditions may be imposed by setting $\mathcal{L}_2 = 0, \mathcal{L}_3 = 0, \dots, \mathcal{L}_{N_s+2} = 0, \mathcal{L}_{N_s+3} = 0$, and to compute \mathcal{L}_1 from the interior flow using equation (149). Letting $\mathcal{L}_2 = 0, \mathcal{L}_3 = 0, \dots, \mathcal{L}_{N_s+2} = 0, \mathcal{L}_{N_s+3} = 0$, prevents exterior information from entering the domain through the $v_x + c$ and v_x characteristics, and the computation of \mathcal{L}_1 from interior data averts a conflict between information conveyed by $v_x - c$ characteristic and the Riemann invariants. Although there is no proof for well-posedness of this procedure (see Table III of Poinsot & Lele [74]), it has been observed to be adequate. Figure 8 shows that acoustic wave reflections are absent at the inflow boundary. Similarly, non-reflecting outflow conditions may be imposed by setting $\mathcal{L}_1 = 0$ and by computing $\mathcal{L}_2, \mathcal{L}_3, \dots, \mathcal{L}_{N_s+2}, \mathcal{L}_{N_s+3}$ from interior data. However, this leads to an ill-posed problem because pressure information is not being conveyed back into the domain by wave reflection. To ensure well-posedness, it is common practice to allow partial reflection by setting

$$\mathcal{L}_1 = K(p - p_\infty) \quad (82)$$

where K denotes a reflection coefficient, p the instantaneous pressure at the boundary, and p_∞ the pressure at infinity on the downstream side. Moreover, various authors [74, 76] have proposed to model the reflection coefficient as

$$K = \sigma [1 - \text{Ma}^2] c/L \quad (83)$$

where Ma is taken to be the maximum Mach number in the domain, L denotes a characteristic length scale that corresponds to the size of the domain, and σ a model constant. The optimum value of σ appears to be problem dependent and lies in the range between 0.25 and 0.7. Values below 0.25 lead to solution drifting, and values above 0.7 lead to large flow oscillations [74]. At the outflow boundary in Figure 8, the reflection coefficient was taken to be zero for the purpose of demonstrating complete suppression of acoustic wave reflection.

7.4 Distortion by a transient heat source

In this problem, a stoichiometric methane-oxygen-nitrogen mixture ($Y_{\text{CH}_4} = 0.058$, $Y_{\text{O}_2} = 0.232$, and $Y_{\text{N}_2} = 0.710$) is distorted by a transient heat source. The pressure and temperature of the mixture within the domain, $-0.03 \text{ m} \leq x \leq 0.03 \text{ m}$, are initially at $p = 10^5 \text{ N m}^2$ and $T = 300 \text{ K}$. The initial velocity of the flowing system, v_x° , is equal to 0.3 m s^{-1} . The transient

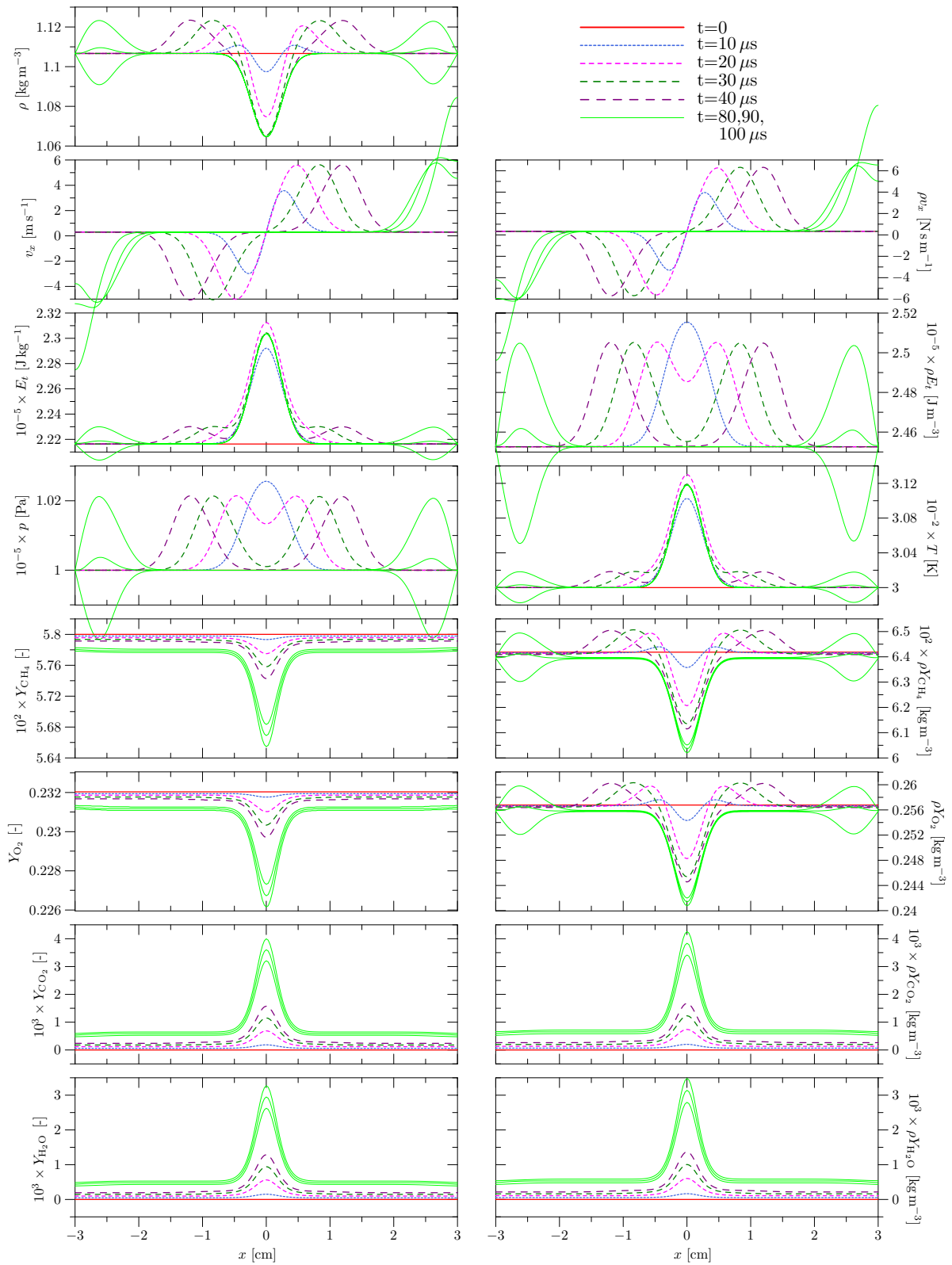


Figure 7. Numerical solution for density, velocity, total energy, pressure, temperature, and species mass fractions at different times with Dirichlet boundary conditions at the inlet and outlet.

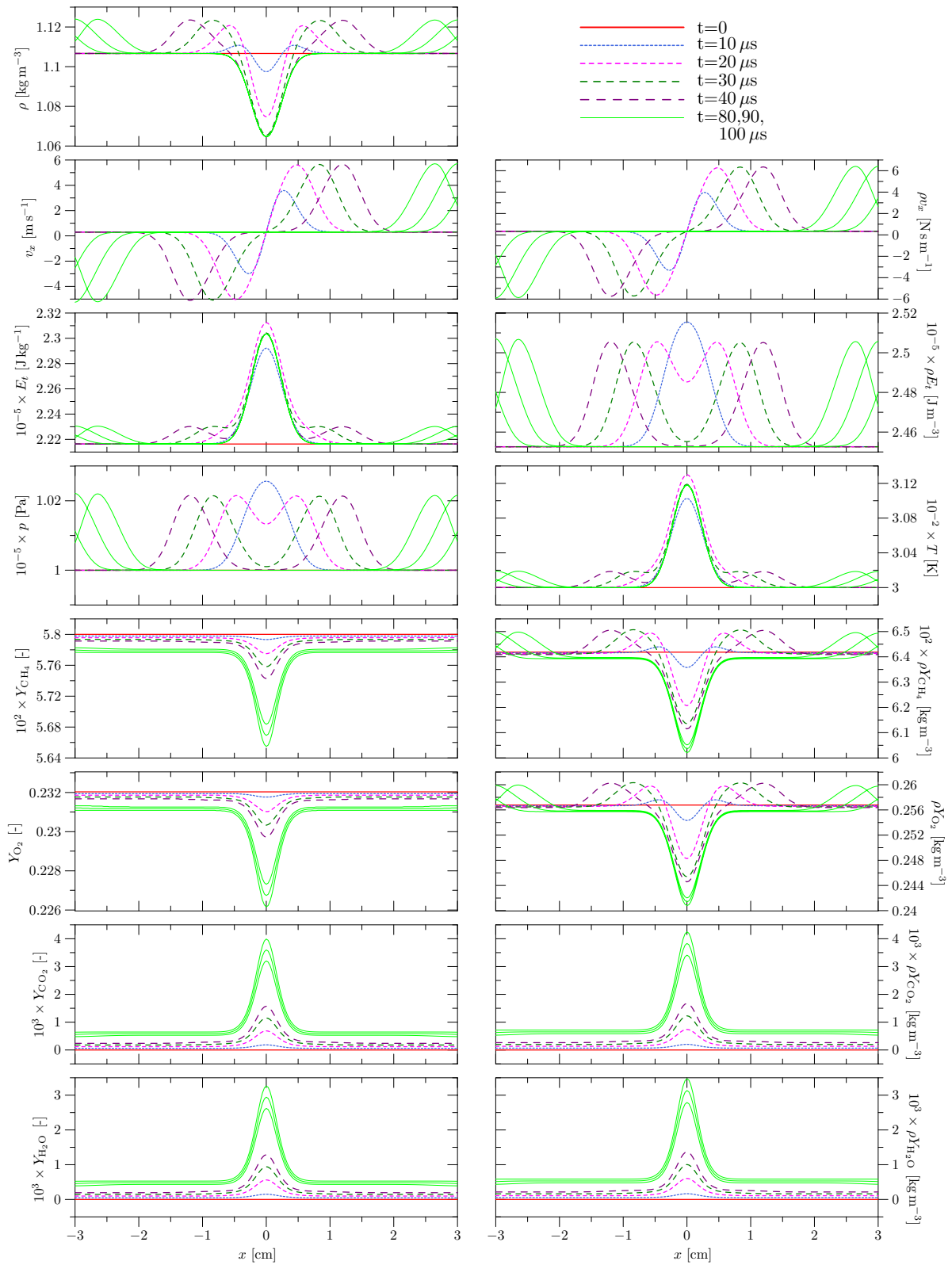


Figure 8. Numerical solution for density, velocity, total energy, pressure, temperature, and species mass fractions at different times with non-reflecting boundary conditions at the inlet and outlet.

heat source has a Gaussian distribution in space and decays quadratically in time according to

$$\omega_Q = a \exp(-bx^2) \left[1 - \frac{t^2}{\tau^2} \right] \quad (84)$$

with $\tau = 20 \cdot 10^{-6}$, $a = 10^9$ and $b = 10^5$ (a determines the strength of the superimposed wave and τ determines its stiffness). To prevent the mixture from igniting all over the domain the chemical source term (65) was modified into

$$\omega_R = \omega_{Y_1} = -c A \rho^{m+n} Y_1^m Y_2^n \exp(-E_a/RT) \quad (85)$$

where $c=10^{13}$ serves to amplify the chemical source terms. This large value appeared necessary to generate a significant effect in the species mass fractions within the short time span between the onset of the ignition source and the moment when waves arrive at the boundaries. To compensate this amplification, the heat of reaction in equation (66) was taken to be $\Delta_R H = -5.0 \cdot 10^{-6} \text{ J kg}^{-1}$. This, to prevent the mixture from igniting all over the entire computational domain. The specific heats, \hat{C}_P and \hat{C}_V , were assumed constant and equal to the mixture average of the specific heats of the reactant species at 300 K. Hence, $\hat{C}_P=1040 \text{ J kg}^{-1} \text{ K}^{-1}$ and $\hat{C}_V=739 \text{ J kg}^{-1} \text{ K}^{-1}$.

A specific amount of artificial diffusion, $\epsilon=10^{-2} \text{ m}^2 \text{ s}^{-1}$, was added to the governing equations (77) as

$$\frac{\partial \mathbf{U}}{\partial t} + \mathbf{A} \cdot \frac{\partial \mathbf{U}}{\partial x} = \mathbf{A} \cdot \mathbf{d} + \boldsymbol{\omega} \quad (86)$$

with

$$\mathbf{d} = \epsilon \Delta x \left[\frac{\partial^2 \rho}{\partial x^2}, \frac{\partial^2 (\rho v_x)}{\partial x^2}, \frac{\partial^2 (\rho Y_1)}{\partial x^2}, \dots, \frac{\partial^2 (\rho Y_{N_s})}{\partial x^2}, \frac{\partial^2 (\rho E_t)}{\partial x^2} \right]. \quad (87)$$

This particular formulation is based on the argument that the amount of artificial diffusion should not only scale with the magnitude of the local gradients and the local grid spacing Δx , but also with the strength of the flux Jacobian. The spatial derivatives were computed with second order accuracy by means of the least-squares gradient reconstruction method described in Section 4. Spatial derivatives at interior nodes were computed by involving the left and right neighbor node. On the boundaries, this was done using the two nearest neighbors within the domain. The accuracy of the spatial derivatives was the same at the interior and the boundary nodes. Time-integration was accomplished by means of the Rosenbrock method described in Subsection 5.2. The mesh consisted of 201 equally distributed vertices and a solution dependent time-step equal to half of

$$h_{\text{conv}} = \frac{\Delta}{1 + |v_x| + c}, \quad (88)$$

where Δ denotes the mesh spacing, was used to ensure stability. Adaptive step size control, as described by equation (44), appeared to be unnecessary.

The solutions obtained at different times ($t=10, 20, 30, 40, 80, 90$, and $100 \mu\text{s}$) are shown in Figures 7 and 8. Prior to the onset of the ignition source, i.e. at $t=0$, all quantities have a constant magnitude across the domain. In the first set of solutions, i.e. at $t=0 \mu\text{s}$, some quantities ($\rho, E_t, \rho E_t$) exhibit the Gaussian shape of the superimposed ignition source, while others ($T, \rho, \rho v_x, \rho Y_{\text{CH}_4}, \rho Y_{\text{O}_2}$) propagate as left and right running waves. It may be verified

that the crests and troughs of these waveforms propagate with velocities belonging to the characteristics. At subsequent times all quantities, except for Y_{CH_4} , Y_{O_2} , Y_{CO_2} , $Y_{\text{H}_2\text{O}}$, ρY_{CO_2} and $\rho Y_{\text{H}_2\text{O}}$ are seen to propagate as left and right running waves. In case of the species mass fractions, the waveform cancels out by the division $\rho Y_i / \rho$, and in case of Y_{CO_2} and $\rho Y_{\text{H}_2\text{O}}$ the amplitude of the waveform is suppressed by the fact that the species mass fractions are zero. At later times, i.e. $t = 80, 90, 100 \mu\text{s}$, Figure 7 exhibits wave reflection at the boundaries, while Figure 8 shows that the same waves leave the domain without being reflected. This confirms that the non-reflecting inflow and outflow boundary conditions, described in the previous subsection, are properly implemented.

8 Application of least-squares gradient reconstruction in conjunction with the Rosenbrock method to the one-dimensional Navier-Stokes equations involving exothermic chemical reaction

8.1 Position of the problem

The problem considered in this section is essentially the same as described in Subsection 7.2, except that the governing equations are taken to be the reactive Navier-Stokes equations,

$$\frac{\partial \rho}{\partial t} + \frac{\partial}{\partial x} [\rho v_x] = 0 \quad (89)$$

$$\frac{\partial (\rho v_x)}{\partial t} + \frac{\partial}{\partial x} [p + \rho v_x v_x] = \frac{\partial}{\partial x} \left[\frac{4}{3} \rho \nu \frac{\partial v_x}{\partial x} \right] \quad (90)$$

$$\frac{\partial (\rho Y_1)}{\partial t} + \frac{\partial}{\partial x} [\rho v_x Y_1] = \frac{\partial}{\partial x} \left[\rho \mathbb{D} \frac{\partial Y_1}{\partial x} \right] + \omega_{Y_1} \quad (91)$$

$$\frac{\partial (\rho Y_2)}{\partial t} + \frac{\partial}{\partial x} [\rho v_x Y_2] = \frac{\partial}{\partial x} \left[\rho \mathbb{D} \frac{\partial Y_2}{\partial x} \right] + \omega_{Y_2} \quad (92)$$

...

$$\frac{\partial (\rho Y_{N_s})}{\partial t} + \frac{\partial}{\partial x} [\rho v_x Y_{N_s}] = \frac{\partial}{\partial x} \left[\rho \mathbb{D} \frac{\partial Y_{N_s}}{\partial x} \right] + \omega_{Y_{N_s}} \quad (93)$$

$$\frac{\partial (\rho E_t)}{\partial t} + \frac{\partial}{\partial x} [p v_x + \rho v_x E_t] = \frac{\partial}{\partial x} \left[\lambda \frac{\partial T}{\partial x} \right] + \omega_R, \quad (94)$$

with p defined according to equation (64), and the source terms according to equations (65) and (66). Notice that the molecular dissipation term is absent in equation (94) and that equal diffusivities are assumed. Physical properties, such as molecular weights and the heat of reaction are the same as in Subsection 7.2. Additional physical properties due to the viscous terms, i.e. the kinematic viscosity, the molecular diffusion coefficient, and the thermal conductivity, are respectively taken to be: $\nu = \mathbb{D} = 10^{-5} \text{ m}^2 \text{s}^{-1}$, and, $\lambda = 0.02 \text{ W m}^{-1} \text{ K}^{-1}$. The specific heats, \hat{C}_P and \hat{C}_V , are assumed constant and equal to the mixture average of the specific heats of the product species at 1500 K. Hence, $\hat{C}_P = 1425 \text{ J kg}^{-1} \text{ K}^{-1}$ and $\hat{C}_V = 1124 \text{ J kg}^{-1} \text{ K}^{-1}$.

8.2 The chemical time scale and adaptive stepsize adjustment

In the previous two sections, numerical solutions could be obtained by assuming a constant time step according to equation (56), and a solution dependent time step according to equation (88). With the diffusion problem stability depends on the mesh spacing only. In case of the transient heat pulse, stability additionally depends on the solution itself, but it appeared to be sufficient to pre-compute a solution dependent time step based on the stability criterion connected with the convective terms. Because of the weakened source terms and the comparatively small variation in the temperature and species mass fractions, there was no need to take the chemical time scales into account. These were substantially larger than those dictated by equation (88). However, without the attenuation of the heat release rate, it becomes necessary to account for the chemical time scale as well.

An estimate of the chemical time scale may be found as follows. First, equations (91) to (93) are rewritten into

$$\frac{\partial Y_{\text{CH}_4}}{\partial t} + \frac{1}{\rho} \frac{\partial}{\partial x} [\rho v_x Y_{\text{CH}_4}] = \frac{1}{\rho} \frac{\partial}{\partial x} \left[\rho \mathbb{D} \frac{\partial Y_{\text{CH}_4}}{\partial x} \right] + \frac{1}{\rho} \omega_{Y_{\text{CH}_4}} \quad (95)$$

$$\frac{\partial Y_{\text{O}_2}}{\partial t} + \frac{1}{\rho} \frac{\partial}{\partial x} [\rho v_x Y_{\text{O}_2}] = \frac{1}{\rho} \frac{\partial}{\partial x} \left[\rho \mathbb{D} \frac{\partial Y_{\text{O}_2}}{\partial x} \right] + \frac{1}{\rho} \omega_{Y_{\text{O}_2}} \quad (96)$$

$$\frac{\partial Y_{\text{N}_2}}{\partial t} + \frac{1}{\rho} \frac{\partial}{\partial x} [\rho v_x Y_{\text{N}_2}] = \frac{1}{\rho} \frac{\partial}{\partial x} \left[\rho \mathbb{D} \frac{\partial Y_{\text{N}_2}}{\partial x} \right] + \frac{1}{\rho} \omega_{Y_{\text{N}_2}} \quad (97)$$

$$\frac{\partial Y_{\text{CO}_2}}{\partial t} + \frac{1}{\rho} \frac{\partial}{\partial x} [\rho v_x Y_{\text{CO}_2}] = \frac{1}{\rho} \frac{\partial}{\partial x} \left[\rho \mathbb{D} \frac{\partial Y_{\text{CO}_2}}{\partial x} \right] + \frac{1}{\rho} \omega_{Y_{\text{CO}_2}} \quad (98)$$

$$\frac{\partial Y_{\text{H}_2\text{O}}}{\partial t} + \frac{1}{\rho} \frac{\partial}{\partial x} [\rho v_x Y_{\text{H}_2\text{O}}] = \frac{1}{\rho} \frac{\partial}{\partial x} \left[\rho \mathbb{D} \frac{\partial Y_{\text{H}_2\text{O}}}{\partial x} \right] + \frac{1}{\rho} \omega_{Y_{\text{H}_2\text{O}}} \quad (99)$$

and supplemented by

$$\frac{\partial T}{\partial t} + \frac{1}{\rho} \frac{\partial}{\partial x} [\rho v_x T] = \frac{1}{\rho \hat{C}_V} \frac{\partial}{\partial x} \left[\lambda \frac{\partial T}{\partial x} \right] + \frac{1}{\rho \hat{C}_V} \omega_R \quad (100)$$

or

$$\frac{\partial T}{\partial t} + \frac{1}{\rho} \frac{\partial}{\partial x} [\rho v_x T] = \frac{1}{\rho \hat{C}_P} \frac{\partial}{\partial x} \left[\lambda \frac{\partial T}{\partial x} \right] + \frac{1}{\rho \hat{C}_P} \omega_R \quad (101)$$

where a distinction is made between a constant volume process (i.e. the density remains constant) and a constant pressure process. In the former case it is helpful to imagine a rigid spherical enclosure filled with reactant species. Starting from an initial temperature T_0 , the mixture is allowed to react uniformly until all reactants are converted into products. Because the volume remains constant, the density remains constant throughout the entire process, while the pressure and temperature increase progressively until the reactants are consumed. The final temperature of the system becomes

$$T_f = T_0 + \Delta_R H Y_{\text{CH}_4}^0 / \hat{C}_V. \quad (102)$$

The latter occurs when the reactants would be enclosed within a soap bubble, instead of a rigid enclosure. Because of the ability of the system to adapt its size to changes caused by chemical reaction, pressure remains constant, while temperature increases progressively, and

density decreases progressively, when the reactants are being converted into products. The resulting final temperature becomes

$$T_f = T_0 + \Delta_R H Y_{\text{CH}_4}^0 / \hat{C}_P, \quad (103)$$

which is significantly less than that indicated by equation (102). Obviously this is due to the fact that no work is done on the surroundings when the size of the enclosure remains fixed.

Next, equations (100) or (101) without the convective and diffusive terms are to be evaluated as follows. Taking equation (100) as an example, it is seen that

$$\frac{\partial T}{\partial t} = -\frac{\Delta_R H}{\hat{C}_V} A \rho^{m+n-1} Y_{\text{CH}_4}^m Y_{\text{O}_2}^n \exp\left(-\frac{E_a}{RT}\right) \quad (104)$$

$$= -\frac{\Delta_R H}{\hat{C}_V} A \rho^{m+n-1} Y_{\text{CH}_4}^m Y_{\text{O}_2}^n \exp\left(-\frac{2E_a}{RT^*}\right) \exp\left(+\frac{E_a}{RT^{*2}}T\right) \quad (105)$$

$$= \mathcal{B} \exp\left(+\frac{E_a}{RT^{*2}}T\right) \quad (106)$$

where

$$\mathcal{B} = -\frac{\Delta_R H}{\hat{C}_V} A \rho^{m+n-1} Y_{\text{CH}_4}^m Y_{\text{O}_2}^n \exp\left(-\frac{2E_a}{RT^*}\right). \quad (107)$$

In the step from equation (104) to equation (105) use was made of the expansion,

$$\frac{1}{T} = \frac{1}{T^*} - (T - T^*) \frac{1}{T^{*2}} + (T - T^*)^2 \frac{1}{T^{*3}} - \dots \quad (108)$$

so that

$$\frac{E_a}{RT} = \frac{E_a}{R} \left[\frac{1}{T^*} - \frac{T - T^*}{T^{*2}} \right] = \frac{E_a}{RT^*} \left[2 - \frac{T}{T^*} \right] \quad (109)$$

and hence

$$\exp\left(-\frac{E_a}{RT}\right) = \exp\left(-\frac{2E_a}{RT^*}\right) \exp\left(+\frac{E_a}{RT^{*2}}T\right). \quad (110)$$

By integrating equation (106) it is seen that

$$\exp\left(-\frac{E_a}{RT^{*2}}T\right) - \exp\left(-\frac{E_a}{RT^{*2}}T^*\right) = \frac{E_a}{RT^{*2}} \mathcal{B} t \quad (111)$$

which, upon division by $\exp(-E_a/RT^*)$, leads to

$$\exp\left(-\frac{E_a}{RT^{*2}}(T - T^*)\right) = 1 - \exp\left(-\frac{E_a}{RT^*}\right) \frac{E_a}{RT^{*2}} \mathcal{B} t \quad (112)$$

$$= 1 - \frac{t}{t_d} \quad (113)$$

where

$$t_d = \frac{RT^{*2}}{E_a \mathcal{B}} \exp\left(-\frac{E_a}{RT^*}\right). \quad (114)$$

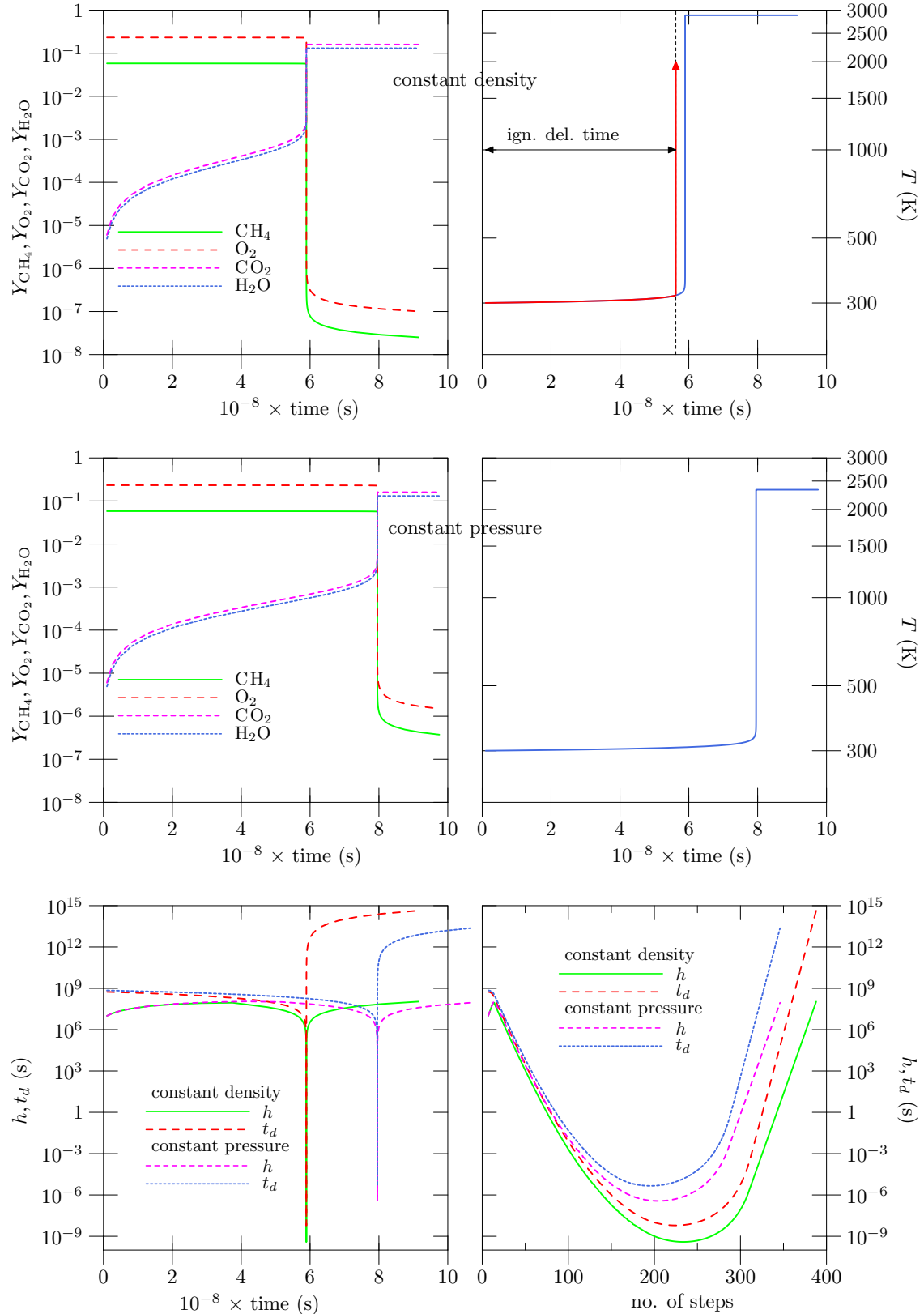


Figure 9. Numerical solution of equations (95) to (101) without convective and diffusive terms.

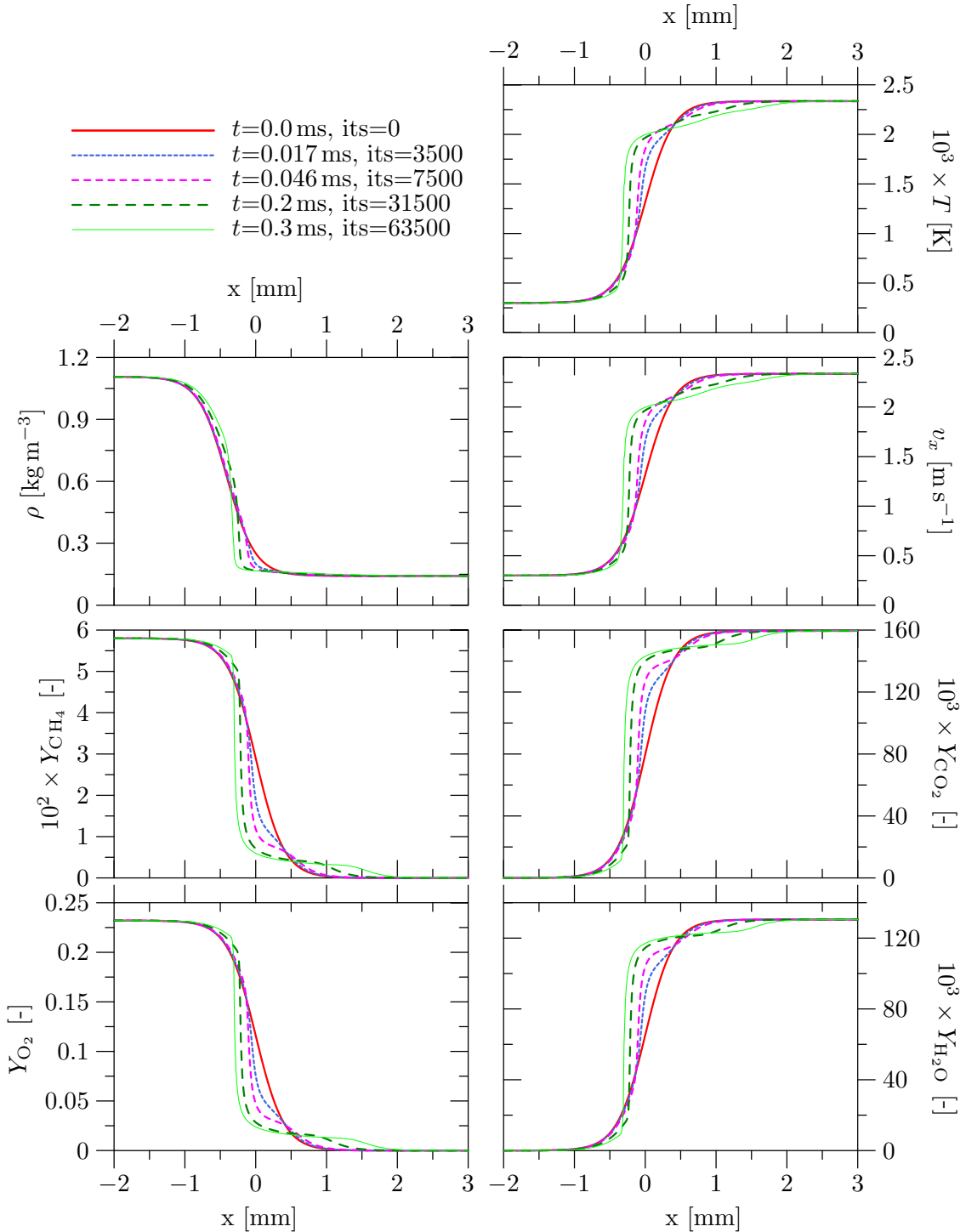


Figure 10. Numerical solution of equations (95) to (99) and (101) with convective and diffusive terms. This solution was obtained with adaptive time-steps following equation (44).

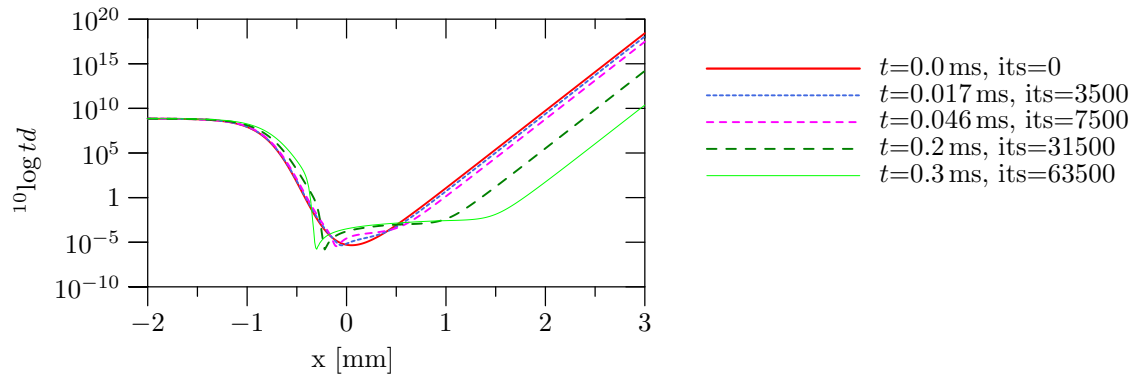


Figure 11. Behavior of the ignition delay time across the mesh.

An explicit expression for the behavior of the temperature in terms of the ignition delay time may then be obtained by taking the logarithm of both sides of equation (113):

$$T = T^* + \frac{RT^*}{E_a} \ln \left[1 - \frac{t}{t_d} \right]. \quad (115)$$

Repeating the procedure with equation (100), instead of (101), obviously leads to the same result, but with \hat{C}_P instead of \hat{C}_V in equation (107).

The numerical solution of equations (95) to (99) with equation (100), without the convective and diffusive terms, is shown in the upper part of Figure 9. A similar solution with equation (101) instead of (100) is shown in the middle part of the figure. Starting from an initial temperature $T_0 = 300$ K, and initial reactant species concentrations, $Y_{\text{CH}_4}^\circ = 0.058$ and $Y_{\text{O}_2}^\circ = 0.232$, these solutions have been obtained by means of the Rosenbrock method with adaptive stepsize adjustment. A relative error tolerance of 10^{-4} was imposed on all dependent quantities.

The significance of equation (115) is illustrated by the upper-right part of Figure 9. Its behavior is depicted by the arrow-headed curve: after a long induction period of little change, the temperature is seen to grow explosively to infinity. The instant on the time-axis when this blowup occurs is governed by the ignition delay time; a quantity whose magnitude may be computed using the same kinetic parameters that govern the actual problem. The value of the ignition delay time ($5.6 \cdot 10^8$ s) was obtained by means of equations (107) and (114), with the temperature and species mass fractions set equal to the aforementioned initial conditions. When compared with the actual behavior of the temperature, it is seen that this approximation gives a conservative estimate of the time scale of true behavior of the temperature.

Despite the attractiveness of employing equation (114) to implement solution dependent stepsize adjustment, there remains an issue of robustness. This is illustrated by the lower part of Figure 9. The lower-left sub-figure shows the behavior of the ignition delay time, t_d , and the behavior of the stepsize, h , taken by the Rosenbrock method conform equation (44) as a function of time. For the sake of clearness, the same information is plotted in the lower-right sub-figure as a function of the number of steps taken. At the beginning of the solution process t_d and h are seen to differ by less than an order of magnitude, with h on the small side. At later times this discrepancy is seen to grow to several orders of magnitude. The lack of robustness arising from the use of equation (114) stems from the fact that the choice of a time step based on the ignition delay time requires a multiplicative factor, such

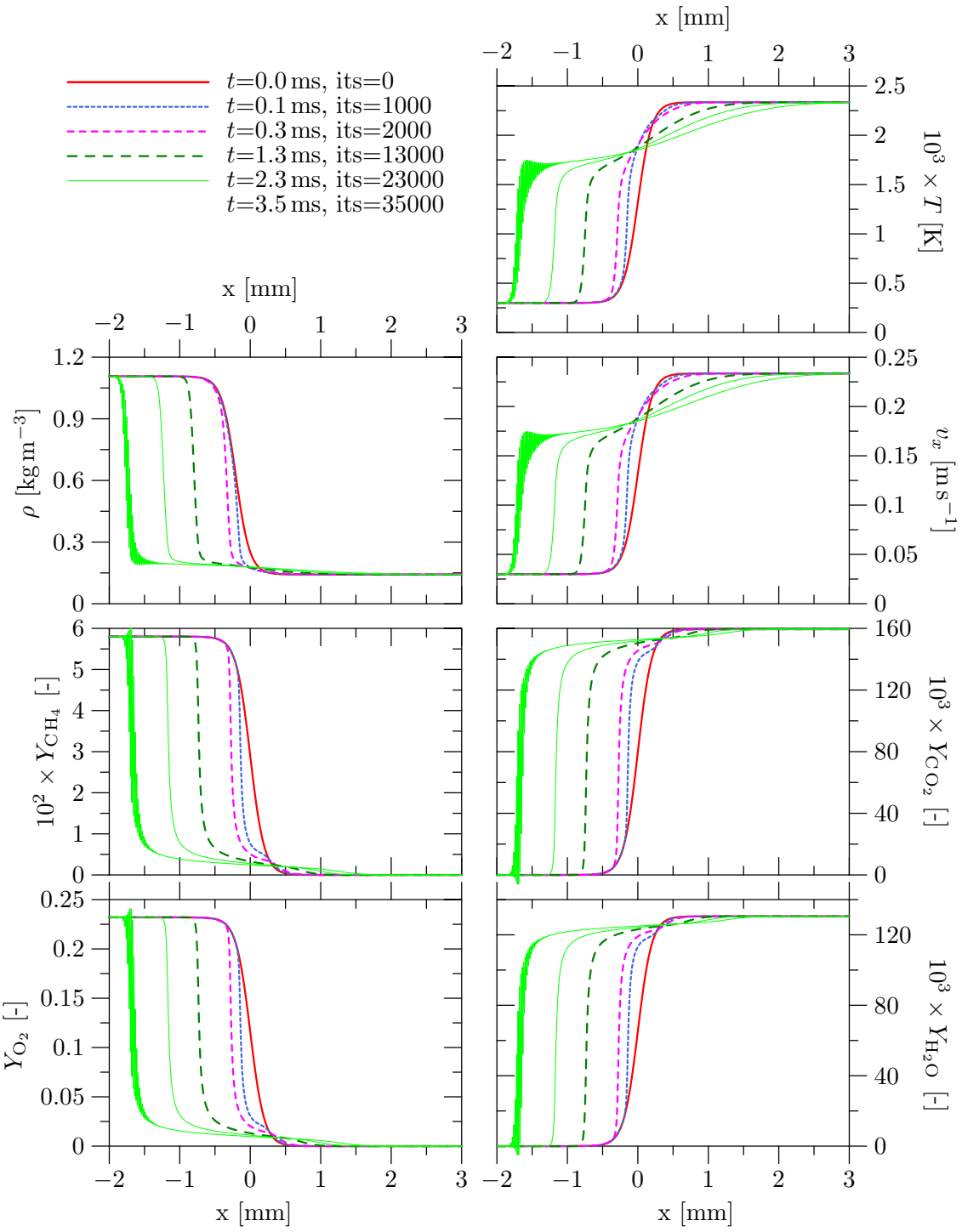


Figure 12. Numerical solution of equations (95) to (99) and (101) with convective and diffusive terms. This solution was obtained with fixed time-steps of 10^{-7} s.

that the resulting time step must be equal to or smaller than h to ensure stability. Because of the variation in the discrepancy between t_d and h in the course the solution process, the multiplicative factor cannot be chosen in a responsible manner. Equation (114) nevertheless remains essential for finding an initial estimate for the stepsize adjustment strategy according to equation (44).

It was also attempted to solve equations (95) to (99) and (101), with the convective and diffusive terms present. The computations have been performed on a domain of 1.5 cm, consisting of 1501 nodes. The inlet velocity of reactants, v_x^o , was taken to be 0.3 m s^{-1} . For all dependent variables, Dirichlet conditions were imposed at the left boundary of the domain, and zero Neumann conditions on the right boundary. Initial conditions were imposed by means of

$$\Psi = \frac{\Psi_R + \Psi_L}{2} + \frac{\Psi_R - \Psi_L}{2} \tanh\left(\frac{x - x_0}{2\delta}\right). \quad (116)$$

with $x_0 = 0.0$, $\delta = 0.1 \text{ mm}$, and where Ψ_L and Ψ_R respectively denote the values of the dependent variables belonging to the fully unreacted and the fully reacted state. Prior to each time step the density was calculated from the pressure and temperature, known from a previous time step, using the ideal gas law. The velocity, shown in Figure 10, was obtained from the fact that its product with the density, ρv_x , remained unchanged across the computational domain. Adaptive stepsize adjustment was accomplished by applying equations (56), (88), and (114) to all nodes, and to seek

$$\min(h_{\text{diff}}, h_{\text{cnvc}}, t_d) \quad (117)$$

over the entire mesh. The resulting value was subsequently used as an initial guess for the stepsize adjustment strategy according to equation (44). A relative error tolerance of 10^{-6} appeared necessary to ensure stability. This resulted in time steps in the order of 10^{-9} s . It was observed that without the evaluation of t_d , the initial guess based on h_{diff} and h_{cnvc} only, was so large that the stepsize adjustment strategy (44) failed on the first attempt already.

Figure 10 shows the solution obtained at different times. With all dependent variables, the initial part of the solution is seen to steepen as time elapses. Beyond this part, an inflection is formed which exhibits a tendency to develop further until an equilibrium state is reached. However, knowing that a typical flame time is in the order of a few milliseconds, and taking into account that more than 60000 time steps were needed to compute the first 0.3 milliseconds of the process, it becomes impractical to proceed until the establishment of a balance between convection, diffusion and reaction. By inspecting Figure 10 in conjunction with equations (107) and (114), it becomes evident that this impracticality is entirely due to the formulation of the source terms. By substituting the values of Y_{CH_4} , Y_{O_2} and T , shown in Figure 10, into equations (107) and (114) it was verified that the maximum allowable time step is physically constrained to a magnitude in the order of 10^{-5} – 10^{-6} s . This is illustrated by Figure 11. However, to ensure stability, this value was reduced to a time step in the order of 10^{-9} s by the stepsize adjustment strategy (44).

To overcome the limitation on the stepsize it was attempted to perform time-marching with larger time steps at the expense of stability. It is emphasized that this may not be regarded as good scientific practice. In fact, its feasibility rests entirely on a cheat. Larger time steps (i.e. 10^{-7} s instead of 10^{-9} s) could be accomplished by constraining the values of the all dependent quantities to their physical extrema. For example, when a timestep

larger than the one arising from equation (44) is taken, the temperature exceeds the flame temperature. To avert this situation the temperature was clamped to the flame temperature when an overshoot occurred. The values of Y_{CH_4} , Y_{O_2} , Y_{CO_2} and $Y_{\text{H}_2\text{O}}$ were similarly clamped to their respective extrema of 0.0, 0.0, 0.1595 and 0.1305 in case of an overshoot.

The behavior of the numerical solution of equations (95) to (99) and (101), obtained with these larger time steps is shown in Figure 12. In this computation, the inlet velocity of the reactants, v_x° , was taken to be 0.03 m s^{-1} to avoid overlapping and intersecting profiles (the previous value of 0.3 m s^{-1} would cause the final solution to obscure the ones obtained at earlier times). Figure 12 shows that the solution process has progressed far enough in time for the establishment of a balance between reaction, convection and diffusion in the left part of the computational domain. For example, a comparison between the solutions at $t = 1.3 \text{ ms}$ and $t = 2.3 \text{ ms}$, reveals that the shape of the initial part of the solutions undergoes little change. Beyond this initial part, the shape is seen to change significantly, which implies that many more steps are needed to reach a steady-state. However, the solution at $t = 3.5 \text{ ms}$ indicates that it makes no sense to proceed with the time-marching process because instability begins to prevail.

The solutions at $t = 1.3 \text{ ms}$ and $t = 2.3 \text{ ms}$ may be used to find an estimate of the laminar burning velocity. Based on the observation that these solutions are separated by a distance of 0.1 mm and cover a time span of 0.1 ms , they propagate to the left side with a velocity equal to 0.4 m s^{-1} . With the flow speed being equal to 0.03 m s^{-1} , this implies that the solutions propagate to the left with a burning velocity equal to 0.37 m s^{-1} . This value is close to recent experimental data on the laminar burning velocity of stoichiometric methane-air mixtures: 0.37 m s^{-1} by van Maaren, Thung & de Goey [77], 0.37 m s^{-1} by Vagelopoulos & Egolfopoulos [78], 0.36 m s^{-1} by Gu, Haq, Lawes, & Woolley [79], and 0.36 m s^{-1} by Bosschaart & de Goey [80]. The laminar flame thickness may also be estimated from the same solutions. It is seen for example, that the a change in the temperature from 300 K to about 1600 K (notice that the corresponding reactant mass fractions decrease to less than 10% of their initial value) over a distance of about 0.3 mm . Laminar flame thicknesses reported in the literature, 1.4 mm by Andrews & Bradley [81], 0.7 mm by Dixon-Lewis & Wilson [82], and 1.1 mm by Janisch [83], are seen to be about two to five times larger. Although it may be argued that our flame thickness would become larger than 0.3 mm after more time steps, it is unreasonable to expect an increase by a factor of two to five because the mass fractions of the reactant species have already fallen to a fraction of their initial value.

9 Conclusions

The potential of least-squares gradient reconstruction to avoid high frequency oscillations in the spatial derivatives, as observed with the application of the discrete Green-Gauss theorem to unstructured grids, was investigated. By considering the practical implementation of the discrete Green-Gauss theorem it became evident that these oscillations arise from an oversimplification in the computation of mean values at the faces of a control volume. Because of the relative simplicity to implement, and the relative inexpensiveness to evaluate, the average value of a quantity across the faces enclosing a control volume is taken to be the arithmetic mean of the values at the vertices spanning each face. By applying a generalized formula for the computation of the mean across a face (equation (6)) to an assumed polynomial variation of a quantity in space (equation (8)), and by comparing the result (equation

(3)) with the arithmetic mean (equation (4)), it is seen that these oscillations are absent only in the case of a linear variation. It is also seen that with nonlinear variations, this approach introduces an error which scales quadratically with the local mesh spacing. As a result, local variations in the mesh spacing are being reflected in the computed spatial derivatives as high frequency oscillations. Moreover, a comparison between equations (3) and (4) reveals that the application of the discrete Green-Gauss theorem yields an accuracy of no more than first order. The severeness of problems arising from the discrete Green-Gauss theorem is illustrated by solving the diffusion equation for an instantaneous spherical surface source as a test case. The numerical solution is shown in the lower part of Figure 6. It is seen that the magnitude of the oscillations is significant with respect to the overall solution. Also, owing to the low accuracy of the method, there exists a significant discrepancy between the numerical and the analytical solution.

Various attempts by previous researchers to overcome problems of non-smooth spatial derivatives and low accuracy arising from the Green-Gauss theorem have been reviewed (Section 3). Despite improvements, it seems to the present authors that these problems are only being mitigated by such methods. Therefore, least-squares gradient reconstruction was introduced as a fundamental remedy. The method employs a Taylor-expansion (equation (30)) of the quantities of interest around each grid point. Mesh irregularity is compensated for by choosing the separation between each nearest-neighbor and the parent vertex along the coordinate-axes as a basis of the polynomial. The polynomial coefficients are taken to be the spatial derivatives which are to be found by least-squares fitting the polynomial to sufficient nearby neighbors. To demonstrate the capability of least-squares gradient reconstruction to produce oscillation-free spatial derivatives, the diffusion equation was solved again for an instantaneous spherical surface source. True second order accuracy was achieved by least-squares fitting equation (30) up to the ninth term to at least nine nearby neighbors of each parent node. The numerical solution, shown in the upper part of Figure 6, is seen to be free of oscillations and almost indistinguishable from the analytical solution.

The introduction of least-squares gradient reconstruction raises the issue of whether or not it is feasible to establish comprehensive numerical schemes, as is the case with previous spatial discretization methods. To shed light on this matter, the method was employed as an equivalent to finite differencing and combined with two distinct time integration schemes: one for non-stiff problems and one for stiff problems. The feasibility combining least-squares gradient reconstruction with a time-integration scheme for non-stiff problems is demonstrated by applying it in conjunction with a Runge-Kutta method to a diffusion problem (see Section 6). For stiff problems an assessment was made of the performance of various time-integration methods on a couple of test problems (Section 5). A Rosenbrock method became the method of choice because its performance was observed to be comparable, and sometimes even superior to that of the well known Gear-methods, which are generally believed to be the method of choice when dealing with stiff problems. A further reason for selecting the Rosenbrock method was that, unlike the Gear-methods, it does not require storage of solutions at previous time-levels to predict the solution at a next time step with higher order accuracy. To demonstrate the feasibility of this combination of methods, it was attempted to solve the Euler equations (Section 7) and the compressible Navier-Stokes (Section 8) with an exothermic chemical reaction present.

Owing to the hyperbolic nature of the reactive Euler equations, (58) to (63), and the reactive Navier-Stokes equations, (89) to (94), two seemingly different sets of auxiliary relationships, (158) to (162), and (190) to (194), were derived to enable the implementation of

boundary conditions in terms of wave amplitude variations. The mechanism by which these relationships are to be employed for the implementation of boundary conditions is discussed in Subsection 7.3. To verify the practical implementation of boundary conditions based on wave amplitude variations, the reactive Euler equations were solved for the problem of a flowing mixture of reactant species, distorted by a transient heat source. The chemical source terms had to be amplified to generate a significant change in the species mass fractions within the short time span between the onset of the heat source and the time when wave variations reach the boundary of the domain. At the same time, the source term of the energy equation had to be weakened by decreasing the heat of reaction to prevent the mixture from igniting all over the domain. Because of the consequential small variation in the temperature, the chemical time scale turned out to be so large that stiffness could only arise from the convective terms, and the time scale of the heat pulse. Solutions of this problem, shown in Figures 7 and 8, indicate that boundary conditions in terms of wave amplitude variations are properly derived and implemented. These solutions also indicate that this combination of methods is feasible.

Next it was attempted to apply the combination of least-squares gradient reconstruction and the Rosenbrock method to a more severe test case involving the reactive Navier-Stokes equations. The compressible equations were first simplified to the system (95)–(101). These equations were solved without the convective and diffusive terms to study the influence of stiffness arising from the chemical source terms on the behavior of the time step. These solutions, obtained by means of the Rosenbrock method with adaptive stepsize adjustment, as well as the behavior of the time steps, are shown in Figure 9. The lower-right part of this figure shows that the stepsize varies by fifteen to twenty orders of magnitude in the course of the solution process. Because the implementation of the Rosenbrock method is known to be much easier without the adaptive stepsize adjustment strategy (44), it seemed worthwhile to derive a rule of the thumb for a conservative estimate of the chemical time scale based on physical grounds. Although such a rule of the thumb could be derived (i.e. equations (114) and (115)), there appears to be a lack of robustness connected to it as explained in Subsection 8.2. This observation implies that adaptive stepsize adjustment based on an error tolerance is of essential importance when dealing stiffness arising from chemistry.

The system (95) to (99) and (101) was subsequently solved with the convective and diffusive terms present. The solutions are shown in Figures 10 and 12. Because this set of equations represents a simplified model of a propagating laminar flame, it was decided to compare the motion of the temperature and species mass fraction profiles in Figure 12 with experimental laminar burning velocities. Our value of 0.37 m s^{-1} is seen to be in agreement with experimental values of $0.36\text{--}0.37 \text{ m s}^{-1}$. The laminar flame thickness of 0.3 mm, derived from the same profiles, is seen to be two to five times smaller than values of 1.4 mm, 0.7 mm and 1.1 mm reported by other researchers.

References

- [1] Godunov S.K. Finite difference method for numerical computation of discontinuous solution of the equations of fluid dynamics. *Matematicheskii Sbornik*, 47:271, 1959. Translated from Russian by I. Bohachevsky.
- [2] Leer B. Van. Towards the ultimate conservative difference scheme. V. A second-order sequel to Godunov's sequel. *Journal of Computational Physics*, 32:101–136, 1979.

- [3] Colella P. and Woodward P. The piecewise parabolic method for gas-dynamical simulations. *Journal of Computational Physics*, 54:174–201, 1984.
- [4] Harten A. and Osher S. Uniformly high order essentially non-oscillatory schemes I. *SIAM Journal on Numerical Analysis*, 24:279–309, 1987.
- [5] Harten A., Enquist B., Osher S., and Chakravarthy S. Uniformly high order essentially non-oscillatory schemes III. *Journal of Computational Physics*, 71:231–303, 1987.
- [6] Liu X.D., Osher S., and Chan T. Weighted essentially non-oscillatory schemes. *Journal of Computational Physics*, 115:200–212, 1994.
- [7] Jiang G. and Shu C.-W. Efficient implementation of weighted ENO schemes. *Journal of Computational Physics*, 126:201–228, 1996.
- [8] Cabello J., Morgan K., and Lohner R. A comparison of higher order schemes used in a finite volume solver for unstructured grids. AIAA-paper 94-2293, 1994.
- [9] Jawahar P. and Kamath H. A high-resolution procedure for Euler and Navier-Stokes computations on unstructured grids. *Journal of Computational Physics*, 164:165–203, 2000.
- [10] Venkatakrishnan V. and Barth T.J. Application of direct solvers to unstructured meshes for the Euler and Navier-Stokes equations using upwind schemes. AIAA-paper 89-0364, 1989.
- [11] Fezoui L. and Stoufflet B. A class of implicit Euler simulations with unstructured meshes. *Journal of Computational Physics*, 84:174–206, 1989.
- [12] Slack D.C., Whitaker D.L., and Walters R.W. Time-integration algorithms for the two-dimensional Euler equations on unstructured meshes. *AIAA Journal*, 32:1158–1166, 1994.
- [13] Batina J.T. Three-dimensional flux-split Euler schemes involving unstructured dynamic meshes. AIAA-paper 90-1649, 1990.
- [14] Barth T.J. and Jespersen D.C. The design and application of upwind schemes on unstructured meshes. AIAA-paper 89-0366, 1989.
- [15] Mathur S.R. and Murthy J.Y. A pressure-based method for unstructured meshes. *Numerical Heat Transfer, Part B*, 31:195–215, 1997.
- [16] Mathur S.R. and Murthy J.Y. Unstructured mesh methods for combustion problems. In Baukal C.E., Gershtein V.Y., and Li X., editors, *Computational Fluid Dynamics in Industrial Combustion*, Industrial Combustion Series, chapter 3, pages 61–94. CRC Press, Boca Raton, Florida, 2000.
- [17] Barth T.J. and Frederickson P.O. Higher order solution of the Euler equations on unstructured grids using quadratic reconstruction. AIAA-paper 90-0013, 1990.
- [18] Frink N.T. Upwind scheme for solving the Euler equations on unstructured tetrahedral meshes. *AIAA Journal*, 30:71–77, 1992.

- [19] Frink N.T. Recent progress towards a three-dimensional unstructured Navier-Stokes flow solver. AIAA-paper 94-0061, 1994.
- [20] Shepard D. A two dimensional interpolation function for irregularly spaced data. In *Proceedings of the 1968 23rd ACM national conference*, pages 517–523. Association for Computing Machinery, 1968.
- [21] Ollivier-Gooch C. and Altena M. Van. A high-order-accurate unstructured mesh finite volume scheme for the advection-diffusion equation. *Journal of Computational Physics*, 181:729–752, 2002.
- [22] Ollivier-Gooch C. Quasi-ENO schemes for unstructured meshes based on unlimited data-dependent least squares reconstruction. *Journal of Computational Physics*, 133:6–17, 1997.
- [23] Golub G.H. and Loan C.F. Van. *Matrix Computations*. The Johns Hopkins University Press, Baltimore, third edition, 1996.
- [24] Businger P. and Golub G.H. Linear least squares solutions by Householder transformations. *Numerische Mathematik*, 7:269–276, 1965.
- [25] Businger P. and Golub G.H. Linear least squares solutions by Householder transformations. In Wilkinson J.H. and Reinsch C., editors, *Handbook for Automatic Computation*, volume 2, chapter 1, pages 111–118. Springer-Verlag, New York, 1971.
- [26] Enright W.H., Hull T.E., and Lindberg B. Comparing numerical methods for stiff systems of ODEs. *BIT*, 15:10–48, 1975.
- [27] Enright W.H. and Hull T.E. Comparing numerical methods for the solution of stiff systems of ODEs arising in chemistry. In L. Lapidus and W.E. Schiesser, editors, *Numerical methods for differential systems*, pages 45–66, 1976.
- [28] Enright W.H. and Pryce J.D. Two FORTRAN packages for assessing initial value problems. *ACM Transactions on Mathematical Software*, 13:1–27, 1987.
- [29] Gear C.W. Algorithm 407, DIFSUB for solution of ordinary differential equations. *Comm. ACM*, 4:185–190, 1971.
- [30] Gear C.W. *Numerical initial value problems in ordinary differential equations*. Prentice Hall, Englewood Cliffs, N.J., 1971.
- [31] Hindmarsh A.C. GEAR: Ordinary differential equation system solver. Technical Report UCID-3001, University of California, Livermore, 1974.
- [32] Byrne G.D. and Hindmarsh A.C. A polyalgorithm for the numerical solution of ordinary differential equations. *ACM Transactions on Mathematical Software*, 1:71–96, 1964.
- [33] Byrne G.D. and Hindmarsh A.C. Implicit Runge-Kutta processes. *Math. Comp.*, 18:50–64, 1964.
- [34] Lawson J.D. and Ehle B.L. Improved generalized Runge-Kutta. In *Proceedings of Canadian Computer Conference*, pages 223201–223213, 1972.

- [35] Enright W.H. Second derivative multistep methods for stiff ordinary differential equations. *SIAM Journal of Numerical Analysis*, 11:321–331, 1974.
- [36] Shampine L.F. Implementation of Rosenbrock methods. *ACM Transactions on Mathematical Software*, 8:93–113, 1982.
- [37] Shampine L.F. Evaluation of a test set for stiff ODE solvers. *ACM Transactions on Mathematical Software*, 7:409–420, 1981.
- [38] Robertson. The solution of a set of reaction rate equations. In J. Walsh, editor, *Numerical Analysis, An Introduction*, pages 178–182, London, 1966. Academic Press.
- [39] Gear C.W. The automatic integration of stiff ordinary differential equations. *Information Processing*, 68:187–193, 1969.
- [40] Luss D. and Amundson N.R. Stability of batch catalytic fluidized beds. *AICHE Journal*, 14(1):211–221, 1968.
- [41] Lapidus L., Aiken R.C., and Liu Y.A. The occurrence and numerical solution of physical and chemical systems having widely varying time constants. In R.A. Willoughby, editor, *Stiff differential systems*, pages 187–200, New York, 1974. Plenum Press.
- [42] Radhakrishnan K. and Hindmarsh A.C. Description and use of LSODE, the Livermore Solver for Ordinary Differential Equations. Technical Report Lawrence Livermore National Laboratory Report UCRL-ID-113855 & NASA Reference Publication 1327, Lawrence Livermore National Laboratory & Lewis Research Center Group, Livermore, 1993.
- [43] Brown P.N., Byrne G.D., and Hindmarsh A.C. VODE: A variable-coefficient ODE solver. *SIAM Journal on Scientific and Statistical Computing*, 10:1038–1051, 1989.
- [44] Press W.H., Teukolsky S.A., Vetterling W.T., and Flannery B.P. *Numerical Recipes in C, The Art of Scientific Computing*. Cambridge, second edition, 1992.
- [45] Kaps P. and Rentrop P. Generalized Runge-Kutta methods of order four with stepsize control for stiff ordinary differential equations. *Numerische Mathematik*, 33:55–68, 1979.
- [46] Carslaw H.S. and Jaeger J.C. *Conduction of Heat in Solids*. Oxford University Press, London, second edition, 1959.
- [47] Hirsch C. *Numerical Computation of Internal and External Flows*, volume 1 of *Wiley series in numerical methods in engineering*. John Wiley & Sons, New York, 1988.
- [48] Jameson A., Baker T.J., and Weatherhill N.P. Calculation of inviscid flow over a complete aircraft. AIAA-paper 86-0103, 1986.
- [49] Dawes W.N. The simulation of three-dimensional viscous flow in turbomachinery geometries using a solution-adaptive unstructured mesh methodology. *Journal of Turbomachinery, Transactions of the ASME*, 114:528–537, 1992.
- [50] Dawes W.N. The practical application of solution-adaption to the numerical simulation of complex turbomachinery problems. *Progress in Aerospace Sciences*, 29:221–269, 1993.

- [51] Jameson A. and Baker T.J. Improvements to the aircraft Euler method. AIAA-paper 87-0425, 1987.
- [52] Lam C.K.G. and Bremhorst K. Modified form of the $k - \epsilon$ model for predicting wall turbulence. *Journal of Fluids Engineering*, 103:456–460, 1981.
- [53] Watterson J.K., Connell I.J., Savill A.M., and Dawes W.N. A solution-adaptive mesh procedure for predicting confined explosions. *International Journal for Numerical Methods in Fluids*, 26:235–247, 1998.
- [54] Bray K.N.C., Libby P.A., and Moss J.B. Unified modelling approach for premixed turbulent combustion – Part I: General formulation. *Combustion and Flame*, 61:87–102, 1985.
- [55] Birkby P., Cant R.S., and Savill A.M. The application of a laminar flamelet model to confined explosion hazards. *Flow, Turbulence and Combustion*, 63:361–377, 1999.
- [56] Patankar S.V. and Spalding D.B. A calculation procedure for heat, mass and momentum transfer in three-dimensional parabolic flows. *International Journal of Heat and Mass Transfer*, 15:1787–1806, 1972.
- [57] Patankar S.V. *Numerical Heat Transfer and Fluid Flow*. Hemisphere Publishing Corporation, Taylor & Francis Group, New York, 1980.
- [58] Doormaal J.P. Van and Raithby G.D. Enhancement of the SIMPLE method for predicting incompressible fluid flows. *Numerical Heat Transfer*, 7:147–163, 1984.
- [59] Issa R. Solution of the implicit discretized fluid flow equations by operator-splitting. *Journal of Computational Physics*, 62:40–65, 1985.
- [60] Karki K.C. and Patankar S.V. Pressure based calculation procedure for viscous flows at all speeds in arbitrary configurations. *AIAA Journal*, 27:1167–1174, 1989.
- [61] Chorin A.J. A numerical method for solving incompressible viscous flow problems. *Journal of Computational Physics*, 2:12–26, 1967.
- [62] Choi D. and Merkle. Application of time-iterative schemes to incompressible flow. AIAA-paper 84-1638, 1984.
- [63] Kwak D. and Chakravarthy S.R. A three-dimensional incompressible Navier-Stokes flow solver using primitive variables. AIAA-paper 84-0253, 1984.
- [64] Rizzi A. and Eriksson L. Computation of inviscid incompressible flow with rotation. *Journal of Fluid Mechanics*, 153:257–312, 1985.
- [65] Walker P.J. and Dawes W.N. The extension and application of three-dimensional time marching to incompressible turbomachinery flow. *Journal of Turbomachinery, Transactions of the ASME*, 112:385–390, 1990.
- [66] Merkle C.L. and Choi Y.-H. Computation of low-speed compressible flows with time-marching procedures. *International Journal for Numerical Methods in Engineering*, 25:293–311, 1988.

- [67] Guerra J. and Gustafsson B. A numerical method for incompressible and compressible flow problems with smooth solutions. *Journal of Computational Physics*, 63:377–397, 1986.
- [68] Klein R. Semi-implicit extension of a Godunov-type scheme based on low Mach number asymptotics. I. one-dimensional flow. *Journal of Computational Physics*, 121:213–237, 1995.
- [69] Schneider T., Botta N., Geratz K.J., and Klein R. Extension of finite volume compressible flow solvers to multi-dimensional, variable density zero mach number flows. *Journal of Computational Physics*, 155:248–286, 1999.
- [70] Choi Y.-H. and Merkle C.L. The application of preconditioning to viscous flows. *Journal of Computational Physics*, 105:207–223, 1993.
- [71] Rook R. and Goey L.P.H. de. The acoustic response of burner-stabilized flat flames: a two-dimensional numerical analysis. *Combustion and Flame*, 133:119–132, 2003.
- [72] Thompson K.W. Time-dependent boundary conditions for hyperbolic systems. *Journal of Computational Physics*, 68:1–24, 1987.
- [73] Thompson K.W. Time-dependent boundary conditions for hyperbolic systems II. *Journal of Computational Physics*, 89:439–461, 1990.
- [74] Poinsot T.J. and Lele S.K. Boundary conditions for direct simulations of compressible viscous flows. *Journal of Computational Physics*, 101:104–129, 1992.
- [75] Baum M., Poinsot T., and Thevenin D. Accurate boundary conditions for multicomponent reactive flows. *Journal of Computational Physics*, 116:247–261, 1994.
- [76] Rudy D.H. and Strikwerda J.C. A nonreflecting outflow boundary condition for subsonic Navier-Stokes calculations. *Journal of Computational Physics*, 36:55–70, 1980.
- [77] Maaren A. Van, Thung D.S., and Goey L.P.H. de. Measurement of flame temperature and adiabatic burning velocity of methane-air mixtures. *Combustion Science and Technology*, 96:327–344, 1994.
- [78] Vagelopoulos C.M. and Egolfopoulos F.N. Direct experimental determination of laminar flame speeds. In *Proceedings of the Twenty-Seventh Symposium (International) on Combustion*, pages 513–519. The Combustion Institute, 1998.
- [79] Gu X.J., Haq M.Z., Lawes M., and Woolley R. Laminar burning velocities and markstein lengths of methane-air mixtures. *Combustion and Flame*, 121:41–58, 2000.
- [80] Bosschaart K.J. and Goey L.P.H. de. Detailed analysis of the heat flux method for measuring burning velocities. *Combustion and Flame*, 132:170–180, 2003.
- [81] Andrews G.E. and Bradley D. The burning velocity of methane-air mixtures. *Combustion and Flame*, 19:275–288, 1972.

- [82] Dixon-Lewis G. and Wilson J.G. A method for the measurement of the temperature distribution in the inner cone of a bunsen flame. *Transactions of the Faraday Society*, 46:1106–1114, 1951.
- [83] Janisch G. · *Chemie-Ing.-Techn.*, 43:561, 1971.

Appendix A

The similarity transformation matrix \mathbf{Q} and its inverse \mathbf{Q}^{-1} appearing in equation (81), with \mathbf{A} defined according to equation (79), may be found as follows. First, the eigenvalues of \mathbf{A} have to be determined by solving the polynomial

$$\det(\mathbf{\Lambda} \cdot \mathbf{I} - \mathbf{A}) = 0. \quad (118)$$

Next, with Λ_{ii} denoting the roots of the polynomial and at the same time the diagonal components of the matrix $\mathbf{\Lambda}$ in equation (81), the right and left eigenvectors, \mathbf{r}_i and \mathbf{l}_i , of \mathbf{A} may be found by solving

$$\Lambda_{ii}\mathbf{r}_i - \mathbf{A} \cdot \mathbf{r}_i = \mathbf{0} \quad (119)$$

and

$$\mathbf{l}_i\Lambda_{ii} - \mathbf{l}_i \cdot \mathbf{A} = \mathbf{0} \quad (120)$$

for each eigenvalue. This procedure leads to (the eigenvalues Λ_{ii} are sorted in ascending order)

$$\Lambda_{11} = v_x - c, \Lambda_{22} = v_x, \Lambda_{33} = v_x, \dots, \Lambda_{(2+N_s)(2+N_s)} = v_x, \Lambda_{(3+N_s)(3+N_s)} = v_x + c, \quad (121)$$

$$\begin{aligned} \mathbf{r}_1 &= \alpha_1' [1, v_x - c, Y_1, Y_2, \dots, Y_{2+N_s}, \frac{1}{\gamma-1}c^2 + \frac{1}{2}v_x^2 - v_xc] \\ \mathbf{r}_2 &= \alpha_2' [1, v_x, 0, 0, \dots, 0, \frac{1}{2}v_x^2] \\ \mathbf{r}_3 &= \alpha_3' [0, 0, 1, 0, \dots, 0, 0] \\ &\quad \dots \\ \mathbf{r}_{2+N_s} &= \alpha_{2+N_s}' [0, 0, 0, 0, \dots, 1, 0] \\ \mathbf{r}_{3+N_s} &= \alpha_{3+N_s}' [1, v_x + c, Y_1, Y_2, \dots, Y_{2+N_s}, \frac{1}{\gamma-1}c^2 + \frac{1}{2}v_x^2 + v_xc], \end{aligned} \quad (122)$$

and

$$\begin{aligned} \mathbf{l}_1 &= \alpha_1'' [\frac{1}{2}v_x^2 + \frac{1}{\gamma-1}v_xc, -\frac{1}{\gamma-1}c - v_x, 0, 0, \dots, 0, 1] \\ \mathbf{l}_2 &= \alpha_2'' [\frac{1}{2}v_x^2 - \frac{1}{\gamma-1}v_xc, -v_x, 0, 0, \dots, 0, 1] \\ \mathbf{l}_3 &= \alpha_3'' [-Y_1, 0, 1, 0, \dots, 0, 0] \\ \mathbf{l}_4 &= \alpha_4'' [-Y_2, 0, 0, 1, \dots, 0, 0] \\ &\quad \dots \\ \mathbf{l}_{2+N_s} &= \alpha_{2+N_s}'' [-Y_{N_s}, 0, 0, 0, \dots, 1, 0] \\ \mathbf{l}_{3+N_s} &= \alpha_{3+N_s}'' [\frac{1}{2}v_x^2 - \frac{1}{\gamma-1}v_xc, \frac{1}{\gamma-1}c - v_x, 0, \dots, 0, 1], \end{aligned} \quad (123)$$

where $\alpha_1', \alpha_2', \dots, \alpha_{3+N_s}'$, and $\alpha_1'', \alpha_2'', \dots, \alpha_{3+N_s}''$ denote scaling factors. Due to the orthogonality condition,

$$\mathbf{l}_i \cdot \mathbf{r}_j = \delta_{ij} = \begin{cases} 1 & \text{if } i = j \\ 0 & \text{if } i \neq j, \end{cases} \quad (124)$$

the arbitrariness of the scaling factors, $\alpha'_1, \alpha'_2, \dots, \alpha'_{3+N_s}$, and $\alpha''_1, \alpha''_2, \dots, \alpha''_{3+N_s}$ reduces to

$$\alpha'_1 = \frac{\gamma - 1}{2\alpha'_1 c^2}, \quad \alpha'_2 = -\frac{\gamma - 1}{\alpha'_2 c^2}, \quad \alpha'_3 = \frac{1}{\alpha'_3}, \quad \dots, \quad \alpha'_{2+N_s} = \frac{1}{\alpha'_{2+N_s}}, \quad \alpha''_{3+N_s} = \frac{\gamma - 1}{2\alpha''_{3+N_s} c^2}. \quad (125)$$

With

$$\alpha'_1 = -\rho/2c, \quad \alpha'_2 = 1, \quad \alpha'_3 = 1, \quad \dots, \quad \alpha'_{2+N_s} = 1, \quad \alpha''_{3+N_s} = \rho/2c, \quad (126)$$

(the choice of these values is motivated further on) the similarity transformation matrix (its columns are the right eigenvectors of \mathbf{A}) and its inverse (its rows are the left eigenvectors of \mathbf{A}) become

$$\mathbf{Q} = \begin{bmatrix} -\frac{\rho}{2c} & 1 & 0 & 0 & \cdot & 0 & \frac{\rho}{2c} \\ -\frac{\rho}{2c}[v_x - c] & v_x & 0 & 0 & \cdot & 0 & \frac{\rho}{2c}[v_x + c] \\ -\frac{\rho}{2c}Y_1 & 0 & 1 & 0 & \cdot & 0 & \frac{\rho}{2c}Y_1 \\ -\frac{\rho}{2c}Y_2 & 0 & 0 & 1 & \cdot & 0 & \frac{\rho}{2c}Y_2 \\ \vdots & \vdots & \ddots & \ddots & \ddots & \ddots & \vdots \\ -\frac{\rho}{2c}Y_{N_s} & 0 & 0 & 0 & \cdot & 1 & \frac{\rho}{2c}Y_{N_s} \\ -\frac{\rho}{2c}\left[\frac{1}{\gamma-1}c^2 + \frac{1}{2}v_x^2 - v_xc\right] & \frac{1}{2}v_x^2 & 0 & 0 & \cdot & 0 & \frac{\rho}{2c}\left[\frac{1}{\gamma-1}c^2 + \frac{1}{2}v_x^2 + v_xc\right] \end{bmatrix} \quad (127)$$

and

$$\mathbf{Q}^{-1} = \frac{\gamma - 1}{\rho c} \begin{bmatrix} -\frac{1}{\gamma-1}v_xc - \frac{1}{2}v_x^2 & \frac{1}{\gamma-1}c + v_x & 0 & \cdot & 0 & -1 \\ \frac{\rho}{c}\left[\frac{1}{\gamma-1}c^2 - \frac{1}{2}v_x^2\right] & \frac{\rho}{c}v_x & 0 & \cdot & 0 & -\frac{\rho}{c} \\ -\frac{\rho c}{(\gamma-1)}Y_1 & 0 & \frac{\rho c}{(\gamma-1)} & \cdot & 0 & 0 \\ \vdots & \vdots & \ddots & \ddots & \ddots & \vdots \\ -\frac{\rho c}{(\gamma-1)}Y_{N_s} & 0 & 0 & \cdot & \frac{\rho c}{(\gamma-1)} & 0 \\ -\frac{1}{\gamma-1}v_xc + \frac{1}{2}v_x^2 & \frac{1}{\gamma-1}c - v_x & 0 & \cdot & 0 & 1 \end{bmatrix} \quad (128)$$

so that the system (77) may be transformed into the characteristic form as

$$\mathbf{Q}^{-1} \cdot \frac{\partial \mathbf{U}}{\partial t} + \mathbf{Q}^{-1} \cdot \mathbf{A} \cdot \frac{\partial \mathbf{U}}{\partial x} = \mathbf{0} \quad (129)$$

$$\iff \mathbf{Q}^{-1} \cdot \frac{\partial \mathbf{U}}{\partial t} + [\mathbf{Q}^{-1} \cdot \mathbf{A} \cdot \mathbf{Q}] \cdot \mathbf{Q}^{-1} \cdot \frac{\partial \mathbf{U}}{\partial x} = \mathbf{0} \quad (130)$$

$$\iff \frac{\partial \tilde{\mathbf{U}}}{\partial t} + \Lambda \cdot \frac{\partial \tilde{\mathbf{U}}}{\partial x} = \mathbf{0} \quad (131)$$

with the characteristic variables defined by

$$d\tilde{\mathbf{U}} = \mathbf{Q}^{-1} d\mathbf{U}. \quad (132)$$

With properly chosen values for the scaling factors $\alpha'_1, \alpha'_2, \dots, \alpha'_{3+N_s}$, as done in equation (126), the preceding expression transforms the system (67) to (72) into a system defined in terms of a combination of variables that remain constant along the characteristics. These so

called Riemann invariants of system (67) to (72) are seen to be

$$d\tilde{\mathbf{U}} = \mathbf{0} \implies \begin{cases} dv_x - \frac{1}{\rho c} dp = 0 & \text{for } \frac{dx}{dt} = \Lambda_{11} = v_x - c \\ d\rho - \frac{1}{c^2} dp = 0 & \text{for } \frac{dx}{dt} = \Lambda_{22} = v_x \\ dY_1 = 0 & \text{for } \frac{dx}{dt} = \Lambda_{33} = v_x \\ dY_2 = 0 & \text{for } \frac{dx}{dt} = \Lambda_{44} = v_x \\ \dots \\ dY_{2+N_s} = 0 & \text{for } \frac{dx}{dt} = \Lambda_{(2+N_s)(2+N_s)} = v_x \\ dv_x + \frac{1}{\rho c} dp = 0 & \text{for } \frac{dx}{dt} = \Lambda_{(3+N_s)(3+N_s)} = v_x + c \end{cases} \quad (133)$$

and will be used as a reference for choosing the scaling factors in Appendix B, C, D and E.

Appendix B

Define a set of primitive variables

$$\mathbf{V} = [\rho, v_x, Y_1, Y_2, \dots, Y_{N_s}, p] \quad (134)$$

$$= [\rho, v_x, Y_1, Y_2, \dots, Y_{N_s}, (\gamma - 1)(\rho E_t - \frac{1}{2}\rho v_x^2)], \quad (135)$$

such that the transformations,

$$\begin{aligned} V_1 &= U_1 & U_1 &= V_1 \\ V_2 &= U_2/U_1 & U_2 &= V_1 V_2 \\ V_3 &= U_3/U_1 & U_3 &= V_1 V_3 \\ V_4 &= U_4/U_1 & U_4 &= V_1 V_4 \\ \dots & & \dots & \\ V_{2+N_s} &= U_{2+N_s}/U_1 & U_{2+N_s} &= V_1 V_{2+N_s} \\ V_{3+N_s} &= (\gamma - 1)[U_{3+N_s} - \frac{1}{2}U_2^2/U_1] & U_{3+N_s} &= V_{3+N_s}/(\gamma - 1) + \frac{1}{2}V_1 V_2^2 \end{aligned} \quad (136)$$

and hence the transformation matrices

$$\mathbf{P} = \frac{\partial \mathbf{U}}{\partial \mathbf{V}} = \begin{bmatrix} 1 & 0 & 0 & 0 & \cdot & 0 & 0 \\ v_x & \rho & 0 & 0 & \cdot & 0 & 0 \\ Y_1 & 0 & \rho & 0 & \cdot & 0 & 0 \\ Y_2 & 0 & 0 & \rho & \cdot & 0 & 0 \\ \cdot & \cdot & \cdot & \cdot & \cdot & \cdot & \cdot \\ Y_{2+N_s} & 0 & 0 & 0 & \cdot & \rho & 0 \\ \frac{1}{2}v_x^2 & \rho v_x & 0 & 0 & \cdot & 0 & (\gamma - 1)^{-1} \end{bmatrix} \quad (137)$$

and

$$\mathbf{P}^{-1} = \frac{\partial \mathbf{V}}{\partial \mathbf{U}} = \begin{bmatrix} 1 & 0 & 0 & 0 & \cdot & 0 & 0 \\ -v_x/\rho & 1/\rho & 0 & 0 & \cdot & 0 & 0 \\ -Y_1/\rho & 0 & 1/\rho & 0 & \cdot & 0 & 0 \\ -Y_2/\rho & 0 & 0 & 1/\rho & \cdot & 0 & 0 \\ \cdot & \cdot & \cdot & \cdot & \cdot & \cdot & \cdot \\ -Y_{2+N_s}/\rho & 0 & 0 & 0 & \cdot & 1/\rho & 0 \\ \frac{1}{2}(\gamma-1)v_x^2 & -(\gamma-1)v_x & 0 & 0 & \cdot & 0 & \gamma-1 \end{bmatrix} \quad (138)$$

come into existence. These matrices may then be used to restate equation (77) in the primitive form:

$$\mathbf{P}^{-1} \cdot \frac{\partial \mathbf{U}}{\partial t} + \mathbf{P}^{-1} \cdot \mathbf{A} \cdot \frac{\partial \mathbf{U}}{\partial x} = \mathbf{0} \quad (139)$$

$$\iff \mathbf{P}^{-1} \cdot \frac{\partial \mathbf{U}}{\partial t} + (\mathbf{P}^{-1} \cdot \mathbf{A} \cdot \mathbf{P}) \cdot \mathbf{P}^{-1} \cdot \frac{\partial \mathbf{U}}{\partial x} = \mathbf{0} \quad (140)$$

$$\iff \frac{\partial \mathbf{V}}{\partial t} + \mathbf{B} \cdot \frac{\partial \mathbf{V}}{\partial x} = \mathbf{0} \quad (141)$$

where

$$\mathbf{B} = \mathbf{P}^{-1} \cdot \mathbf{A} \cdot \mathbf{P} = \begin{bmatrix} v_x & \rho & 0 & 0 & \cdot & 0 & 0 \\ 0 & v_x & 0 & 0 & \cdot & 0 & 1/\rho \\ 0 & 0 & v_x & 0 & \cdot & 0 & 0 \\ 0 & 0 & 0 & v_x & \cdot & 0 & 0 \\ \cdot & \cdot & \cdot & \cdot & \cdot & \cdot & \cdot \\ 0 & 0 & 0 & 0 & \cdot & v_x & 0 \\ 0 & \rho c^2 & 0 & 0 & \cdot & 0 & v_x \end{bmatrix}. \quad (142)$$

An auxiliary system of equations in terms of wave amplitude variations, \mathcal{L} , may be obtained by applying a similarity transformation to (141), i.e.

$$\mathbf{S}^{-1} \cdot \mathbf{B} \cdot \mathbf{S} = \Lambda \iff \mathbf{B} = \mathbf{S} \cdot \Lambda \cdot \mathbf{S}^{-1} \quad (143)$$

Details of the similarity transformation and the precise form of \mathbf{S} and \mathbf{S}^{-1} are described in Appendix D. With these transformation matrices the primitive form (141) in terms of the wave amplitude variations becomes,

$$\frac{\partial \mathbf{V}}{\partial t} + \mathbf{S} \cdot \Lambda \cdot \mathbf{S}^{-1} \cdot \frac{\partial \mathbf{V}}{\partial x} = \mathbf{0} \quad (144)$$

$$\iff \frac{\partial \mathbf{V}}{\partial t} + \mathbf{S} \cdot \mathcal{L} = \mathbf{0} \quad (145)$$

and the conservation form (77) becomes:

$$\frac{\partial \mathbf{U}}{\partial t} + (\mathbf{P} \cdot \mathbf{S}) \cdot \Lambda \cdot (\mathbf{S} \cdot \mathbf{P})^{-1} \cdot \frac{\partial \mathbf{U}}{\partial x} = \mathbf{0} \quad (146)$$

$$\iff \frac{\partial \mathbf{U}}{\partial t} + \mathbf{P} \cdot \mathbf{S} \cdot \mathcal{L} = \mathbf{0} \quad (147)$$

where

$$\mathcal{L} = \mathbf{\Lambda} \cdot \mathbf{S}^{-1} \cdot \frac{\partial \mathbf{V}}{\partial x}, \quad (148)$$

or, more explicitly,

$$\mathcal{L}_1 = (v_x - c) \left[\frac{\partial v_x}{\partial x} - \frac{1}{\rho c} \frac{\partial p}{\partial x} \right] \quad (149)$$

$$\mathcal{L}_2 = v_x \left[\frac{\partial \rho}{\partial x} - \frac{1}{c^2} \frac{\partial p}{\partial x} \right] \quad (150)$$

$$\mathcal{L}_3 = \rho v_x \frac{\partial Y_1}{\partial x} \quad (151)$$

$$\mathcal{L}_4 = \rho v_x \frac{\partial Y_2}{\partial x} \quad (152)$$

$$\dots \quad (153)$$

$$\mathcal{L}_{2+N_s} = \rho v_x \frac{\partial Y_{N_s}}{\partial x} \quad (154)$$

$$\mathcal{L}_{3+N_s} = (v_x + c) \left[\frac{\partial v_x}{\partial x} + \frac{1}{\rho c} \frac{\partial p}{\partial x} \right] \quad (155)$$

Substitution of the wave amplitude variations into (147) and noting that

$$\mathbf{P} \cdot \mathbf{S} = \begin{bmatrix} -\rho/2c & 1 & 0 & 0 & \dots & 0 & \rho/2c \\ -\frac{\rho}{2c}v_x + \frac{\rho}{2} & v_x & 0 & 0 & \dots & 0 & \frac{\rho}{2c}v_x + \frac{\rho}{2} \\ -\frac{\rho}{2c}Y_1 & 0 & 1 & 0 & \dots & 0 & \frac{\rho}{2c}Y_1 \\ -\frac{\rho}{2c}Y_2 & 0 & 0 & 1 & \dots & 0 & \frac{\rho}{2c}Y_2 \\ \vdots & \vdots & \ddots & \ddots & \ddots & \vdots & \vdots \\ -\frac{\rho}{2c}Y_{N_s} & 0 & 0 & 0 & \dots & 1 & \frac{\rho}{2c}Y_{N_s} \\ -\frac{\rho}{4c}v_x^2 + \frac{\rho v_x}{2} - \frac{\rho c}{2(\gamma - 1)} & \frac{v_x^2}{2} & 0 & 0 & \dots & 0 & \frac{\rho}{4c}v_x^2 + \frac{\rho v_x}{2} + \frac{\rho c}{2(\gamma - 1)} \end{bmatrix} \quad (156)$$

leads to the auxiliary system

$$\frac{\partial \rho}{\partial t} + \mathcal{L}_2 + \frac{\rho}{2c} [\mathcal{L}_{3+N_s} - \mathcal{L}_1] = 0 \quad (157)$$

$$\frac{\partial (\rho v_x)}{\partial t} + v_x \mathcal{L}_2 + \frac{\rho}{2} [\mathcal{L}_{3+N_s} + \mathcal{L}_1] + \frac{\rho v_x}{2c} [\mathcal{L}_{3+N_s} - \mathcal{L}_1] = 0 \quad (158)$$

$$\frac{\partial (\rho Y_1)}{\partial t} + \mathcal{L}_3 + \frac{\rho Y_1}{2c} [\mathcal{L}_{3+N_s} - \mathcal{L}_1] = 0 \quad (159)$$

$$\frac{\partial (\rho Y_2)}{\partial t} + \mathcal{L}_4 + \frac{\rho Y_2}{2c} [\mathcal{L}_{3+N_s} - \mathcal{L}_1] = 0 \quad (160)$$

$$\dots$$

$$\frac{\partial (\rho Y_{N_s})}{\partial t} + \mathcal{L}_{2+N_s} + \frac{\rho Y_{N_s}}{2c} [\mathcal{L}_{3+N_s} - \mathcal{L}_1] = 0 \quad (161)$$

$$\frac{\partial (\rho E_t)}{\partial t} + \frac{v_x^2}{2} \mathcal{L}_2 + \frac{\rho v_x}{2} [\mathcal{L}_{3+N_s} + \mathcal{L}_1] + \left[\frac{\rho v_x^2}{4c} + \frac{\rho c}{2(\gamma - 1)} \right] [\mathcal{L}_{3+N_s} - \mathcal{L}_1] = 0 \quad (162)$$

Dirichlet conditions may be implemented through the system obtained by substituting the wave amplitude variations into (145),

$$\frac{\partial \rho}{\partial t} + \mathcal{L}_2 + \frac{\rho}{2c} [\mathcal{L}_{3+N_s} - \mathcal{L}_1] = 0 \quad (163)$$

$$\frac{\partial v_x}{\partial t} + \frac{1}{2} [\mathcal{L}_{3+N_s} + \mathcal{L}_1] = 0 \quad (164)$$

$$\frac{\partial Y_1}{\partial t} + \frac{1}{\rho} \mathcal{L}_3 = 0 \quad (165)$$

$$\frac{\partial Y_2}{\partial t} + \frac{1}{\rho} \mathcal{L}_4 = 0 \quad (166)$$

...

$$\frac{\partial Y_{N_s}}{\partial t} + \frac{1}{\rho} \mathcal{L}_{2+N_s} = 0 \quad (167)$$

$$\frac{\partial p}{\partial t} + \frac{\rho c}{2} [\mathcal{L}_{3+N_s} - \mathcal{L}_1] = 0 \quad (168)$$

and Neumann conditions may be imposed by using the equations that result from solving (149) to (155) for the gradients:

$$\frac{\partial \rho}{\partial x} = \frac{\mathcal{L}_2}{v_x} + \frac{\rho}{2c} \left[\frac{\mathcal{L}_{3+N_s}}{v_x + c} - \frac{\mathcal{L}_1}{v_x - c} \right] \quad (169)$$

$$\frac{\partial v_x}{\partial x} = \frac{1}{2} \left[\frac{\mathcal{L}_{3+N_s}}{v_x + c} + \frac{\mathcal{L}_1}{v_x - c} \right] \quad (170)$$

$$\frac{\partial Y_1}{\partial x} = \frac{\mathcal{L}_3}{\rho v_x} \quad (171)$$

$$\frac{\partial Y_2}{\partial x} = \frac{\mathcal{L}_4}{\rho v_x} \quad (172)$$

...

$$\frac{\partial Y_{N_s}}{\partial x} = \frac{\mathcal{L}_{2+N_s}}{\rho v_x} \quad (173)$$

$$\frac{\partial p}{\partial x} = \frac{\rho c}{2} \left[\frac{\mathcal{L}_{3+N_s}}{v_x + c} - \frac{\mathcal{L}_1}{v_x - c} \right] \quad (174)$$

Appendix C

Define another set of primitive variables

$$\mathbf{V} = [\rho, v_x, Y_1, Y_2, \dots, Y_{N_s}, T] \quad (175)$$

$$= [\rho, v_x, Y_1, Y_2, \dots, Y_{N_s}, (E_t - \frac{1}{2}v_x^2)/\hat{C}_V], \quad (176)$$

such that the transformations,

$$\begin{aligned}
V_1 &= U_1 & U_1 &= V_1 \\
V_2 &= U_2/U_1 & U_2 &= V_1 V_2 \\
V_3 &= U_3/U_1 & U_3 &= V_1 V_3 \\
V_4 &= U_4/U_1 & U_4 &= V_1 V_4 \\
&\dots & &\dots \\
V_{2+N_s} &= U_{2+N_s}/U_1 & U_{2+N_s} &= V_1 V_{2+N_s} \\
V_{3+N_s} &= [(U_{3+N_s}/U_1) - \frac{1}{2}(U_2^2/U_1^2)]/\hat{C}_V & U_{3+N_s} &= \hat{C}_V V_1 V_{3+N_s} + \frac{1}{2} V_1 V_2^2
\end{aligned} \tag{177}$$

and hence the transformation matrices

$$\mathbf{P} = \frac{\partial \mathbf{U}}{\partial \mathbf{V}} = \begin{bmatrix} 1 & 0 & 0 & 0 & \cdot & 0 & 0 \\ v_x & \rho & 0 & 0 & \cdot & 0 & 0 \\ Y_1 & 0 & \rho & 0 & \cdot & 0 & 0 \\ Y_2 & 0 & 0 & \rho & \cdot & 0 & 0 \\ \cdot & \cdot & \cdot & \cdot & \cdot & \cdot & \cdot \\ Y_{2+N_s} & 0 & 0 & 0 & \cdot & \rho & 0 \\ \frac{1}{\gamma(\gamma-1)}c^2 + \frac{1}{2}v_x^2 & \rho v_x & 0 & 0 & \cdot & 0 & \rho \hat{C}_V \end{bmatrix} \tag{178}$$

and

$$\mathbf{P}^{-1} = \frac{\partial \mathbf{V}}{\partial \mathbf{U}} = \begin{bmatrix} 1 & 0 & 0 & 0 & \cdot & 0 & 0 \\ -v_x/\rho & 1/\rho & 0 & 0 & \cdot & 0 & 0 \\ -Y_1/\rho & 0 & 1/\rho & 0 & \cdot & 0 & 0 \\ -Y_2/\rho & 0 & 0 & 1/\rho & \cdot & 0 & 0 \\ \cdot & \cdot & \cdot & \cdot & \cdot & \cdot & \cdot \\ -Y_{2+N_s}/\rho & 0 & 0 & 0 & \cdot & 1/\rho & 0 \\ -\left[\frac{1}{\gamma(\gamma-1)}c^2 - \frac{1}{2}v_x^2\right]/\rho \hat{C}_V & -v_x/\rho \hat{C}_V & 0 & 0 & \cdot & 0 & 1/\rho \hat{C}_V \end{bmatrix} \tag{179}$$

come into existence. Following equations (139) to (141), these matrices may be used to restate equation (77) in the primitive form (141), where

$$\mathbf{B} = \mathbf{P}^{-1} \cdot \mathbf{A} \cdot \mathbf{P} = \begin{bmatrix} v_x & \rho & 0 & 0 & \cdot & 0 & 0 \\ c^2/\gamma\rho & v_x & 0 & 0 & \cdot & 0 & (\gamma-1)\hat{C}_V \\ 0 & 0 & v_x & 0 & \cdot & 0 & 0 \\ 0 & 0 & 0 & v_x & \cdot & 0 & 0 \\ \cdot & \cdot & \cdot & \cdot & \cdot & \cdot & \cdot \\ 0 & 0 & 0 & 0 & \cdot & v_x & 0 \\ 0 & c^2/\gamma\hat{C}_V & 0 & 0 & \cdot & 0 & v_x \end{bmatrix}. \tag{180}$$

An auxiliary system of equations in terms of wave amplitude variations, \mathcal{L} , defined according to equation (148), may be obtained by applying a similarity transformation to (180). Details of this similarity transformation and the matrices \mathbf{S} and \mathbf{S}^{-1} arising from it are given in

appendix E. With these matrices, the wave amplitude variations are seen to become

$$\mathcal{L}_1 = (v_x - c) \left[-\frac{c}{\gamma\rho} \frac{\partial\rho}{\partial x} + \frac{\partial v_x}{\partial x} - \frac{(\gamma-1)\hat{C}_V}{c} \frac{\partial T}{\partial x} \right] \quad (181)$$

$$\mathcal{L}_2 = v_x \left[\frac{\gamma-1}{\gamma} \frac{\partial\rho}{\partial x} - \frac{(\gamma-1)\rho\hat{C}_V}{c^2} \frac{\partial T}{\partial x} \right] \quad (182)$$

$$\mathcal{L}_3 = \rho v_x \frac{\partial Y_1}{\partial x} \quad (183)$$

$$\mathcal{L}_4 = \rho v_x \frac{\partial Y_2}{\partial x} \quad (184)$$

$$\dots \quad (185)$$

$$\mathcal{L}_{2+N_s} = \rho v_x \frac{\partial Y_{N_s}}{\partial x} \quad (186)$$

$$\mathcal{L}_{3+N_s} = (v_x + c) \left[\frac{c}{\gamma\rho} \frac{\partial\rho}{\partial x} + \frac{\partial v_x}{\partial x} + \frac{(\gamma-1)\hat{C}_V}{c} \frac{\partial T}{\partial x} \right] \quad (187)$$

After substitution into equation (147) and by noting that

$$\mathbf{P} \cdot \mathbf{S} = \begin{bmatrix} -\rho/2c & 1 & 0 & 0 & \dots & 0 & \rho/2c \\ -\frac{\rho}{2c}v_x + \frac{\rho}{2} & v_x & 0 & 0 & \dots & 0 & \frac{\rho}{2c}v_x + \frac{\rho}{2} \\ -\frac{\rho}{2c}Y_1 & 0 & 1 & 0 & \dots & 0 & \frac{\rho}{2c}Y_1 \\ -\frac{\rho}{2c}Y_2 & 0 & 0 & 1 & \dots & 0 & \frac{\rho}{2c}Y_2 \\ \vdots & \vdots & \vdots & \vdots & \ddots & \vdots & \vdots \\ -\frac{\rho}{2c}Y_{N_s} & 0 & 0 & 0 & \dots & 1 & \frac{\rho}{2c}Y_{N_s} \\ -\frac{\rho}{2c} \left[\hat{C}_V T + \frac{v_x^2}{2} \right] + \frac{\rho v_x}{2} - \frac{\rho c}{2\gamma} & \frac{v_x^2}{2} & 0 & 0 & \dots & 0 & \frac{\rho}{2c} \left[\hat{C}_V T + \frac{v_x^2}{2} \right] + \frac{\rho v_x}{2} + \frac{\rho c}{2\gamma} \end{bmatrix}, \quad (188)$$

the following auxiliary system is obtained:

$$\frac{\partial\rho}{\partial t} + \mathcal{L}_2 + \frac{\rho}{2c} [\mathcal{L}_{3+N_s} - \mathcal{L}_1] = 0 \quad (189)$$

$$\frac{\partial(\rho v_x)}{\partial t} + v_x \mathcal{L}_2 + \frac{\rho}{2} [\mathcal{L}_{3+N_s} + \mathcal{L}_1] + \frac{\rho v_x}{2c} [\mathcal{L}_{3+N_s} - \mathcal{L}_1] = 0 \quad (190)$$

$$\frac{\partial(\rho Y_1)}{\partial t} + \mathcal{L}_3 + \frac{\rho Y_1}{2c} [\mathcal{L}_{3+N_s} - \mathcal{L}_1] = 0 \quad (191)$$

$$\frac{\partial(\rho Y_2)}{\partial t} + \mathcal{L}_4 + \frac{\rho Y_2}{2c} [\mathcal{L}_{3+N_s} - \mathcal{L}_1] = 0 \quad (192)$$

$$\dots$$

$$\frac{\partial(\rho Y_{N_s})}{\partial t} + \mathcal{L}_{2+N_s} + \frac{\rho Y_{N_s}}{2c} [\mathcal{L}_{3+N_s} - \mathcal{L}_1] = 0 \quad (193)$$

$$\frac{\partial(\rho E_t)}{\partial t} + \frac{v_x^2}{2} \mathcal{L}_2 + \frac{\rho v_x}{2} [\mathcal{L}_{3+N_s} + \mathcal{L}_1] + \left[\frac{\rho}{2c} \left[\hat{C}_V T + \frac{v_x^2}{2} \right] + \frac{\rho c}{2\gamma} \right] [\mathcal{L}_{3+N_s} - \mathcal{L}_1] = 0 \quad (194)$$

Dirichlet conditions may be implemented through the system obtained by substituting the wave amplitude variations into (145),

$$\frac{\partial \rho}{\partial t} + \mathcal{L}_2 + \frac{\rho}{2c} [\mathcal{L}_{3+N_s} - \mathcal{L}_1] = 0 \quad (195)$$

$$\frac{\partial v_x}{\partial t} + \frac{1}{2} [\mathcal{L}_{3+N_s} + \mathcal{L}_1] = 0 \quad (196)$$

$$\frac{\partial Y_1}{\partial t} + \frac{1}{\rho} \mathcal{L}_3 = 0 \quad (197)$$

$$\frac{\partial Y_2}{\partial t} + \frac{1}{\rho} \mathcal{L}_4 = 0 \quad (198)$$

...

$$\frac{\partial Y_{N_s}}{\partial t} + \frac{1}{\rho} \mathcal{L}_{2+N_s} = 0 \quad (199)$$

$$\frac{\partial T}{\partial t} + \frac{c^2}{\gamma(\gamma-1)\rho\hat{C}_V} \mathcal{L}_2 + \frac{c}{2\gamma\hat{C}_V} [\mathcal{L}_{3+N_s} - \mathcal{L}_1] = 0 \quad (200)$$

and Neumann conditions may be imposed by using the equations that result from solving (181) to (187) for the gradients:

$$\frac{\partial \rho}{\partial x} = \frac{\mathcal{L}_2}{v_x} + \frac{\rho}{2c} \left[\frac{\mathcal{L}_{3+N_s}}{v_x + c} - \frac{\mathcal{L}_1}{v_x - c} \right] \quad (201)$$

$$\frac{\partial v_x}{\partial x} = \frac{1}{2} \left[\frac{\mathcal{L}_{3+N_s}}{v_x + c} + \frac{\mathcal{L}_1}{v_x - c} \right] \quad (202)$$

$$\frac{\partial Y_1}{\partial x} = \frac{\mathcal{L}_3}{\rho v_x} \quad (203)$$

$$\frac{\partial Y_2}{\partial x} = \frac{\mathcal{L}_4}{\rho v_x} \quad (204)$$

...

$$\frac{\partial Y_{N_s}}{\partial x} = \frac{\mathcal{L}_{2+N_s}}{\rho v_x} \quad (205)$$

$$\frac{\partial T}{\partial x} = \frac{c^2}{\gamma(\gamma-1)\rho\hat{C}_V} \left[-\frac{\mathcal{L}_2}{v_x} + (\gamma-1)\frac{\rho}{2c} \left(\frac{\mathcal{L}_{3+N_s}}{v_x + c} - \frac{\mathcal{L}_1}{v_x - c} \right) \right] \quad (206)$$

However, because

$$\hat{C}_V T = E_t - \frac{1}{2} v_x^2 = \frac{1}{\gamma(\gamma-1)} c^2, \quad (207)$$

and hence

$$\frac{\rho}{2c} \left[\hat{C}_V T + \frac{v_x^2}{2} \right] + \frac{\rho c}{2\gamma} = \frac{\rho v_x^2}{4c} + \frac{\rho c}{2(\gamma-1)}, \quad (208)$$

equation (188) and system (190) to (194) are seen to become identical to equation (156) and system (158) to (162). Furthermore, equation (208) and the ideal gas law

$$p = \rho R T \implies dp = RT d\rho + \rho R dT \quad (209)$$

may be used to transform equation (200) and (206) into equation (168) and (174). This consistency between the auxiliary systems arising from two distinct sets of primitive variables, (134) and (175), serves as a verification of their derivation.

Appendix D

The similarity transformation matrix \mathbf{S} and its inverse \mathbf{S}^{-1} in equations (147) and (148), with \mathbf{B} defined according to equation (142), may be found by following the procedure constituted by equations (118) to (120). This leads to (the eigenvalues Λ_{ii} are sorted in ascending order)

$$\Lambda_{11} = v_x - c, \Lambda_{22} = v_x, \Lambda_{33} = v_x, \dots, \Lambda_{(2+N_s)(2+N_s)} = v_x, \Lambda_{(3+N_s)(3+N_s)} = v_x + c, \quad (210)$$

$$\begin{aligned} \mathbf{r}_1 &= \alpha'_1 [-\rho/c, 1, 0, 0, \dots, 0, -\rho c] \\ \mathbf{r}_2 &= \alpha'_2 [1, 0, 0, 0, \dots, 0, 0] \\ \mathbf{r}_3 &= \alpha'_3 [0, 0, 1, 0, \dots, 0, 0] \\ \mathbf{r}_4 &= \alpha'_4 [0, 0, 0, 1, \dots, 0, 0] \\ &\dots \\ \mathbf{r}_{2+N_s} &= \alpha'_{2+N_s} [0, 0, 0, 0, \dots, 1, 0] \\ \mathbf{r}_{3+N_s} &= \alpha'_{3+N_s} [\rho/c, 1, 0, 0, \dots, 0, \rho c], \end{aligned} \quad (211)$$

and

$$\begin{aligned} \mathbf{l}_1 &= \alpha''_1 [0, -\rho c, 0, 0, \dots, 0, 1] \\ \mathbf{l}_2 &= \alpha''_2 [-c^2, 0, 0, 0, \dots, 0, 1] \\ \mathbf{l}_3 &= \alpha''_3 [0, 0, 1, 0, \dots, 0, 0] \\ \mathbf{l}_4 &= \alpha''_4 [0, 0, 0, 1, \dots, 0, 0] \\ &\dots \\ \mathbf{l}_{2+N_s} &= \alpha''_{2+N_s} [0, 0, 0, 0, \dots, 1, 0] \\ \mathbf{l}_{3+N_s} &= \alpha''_{3+N_s} [0, \rho c, 0, 0, \dots, 0, 1]. \end{aligned} \quad (212)$$

Since the left and right eigenvectors must fulfill the orthogonality condition (124), the scaling factors $\alpha'_1, \alpha'_2, \dots, \alpha'_{3+N_s}$, and $\alpha''_1, \alpha''_2, \dots, \alpha''_{3+N_s}$ are related to one another as

$$\alpha'_1 = -\frac{1}{2\alpha'_1\rho c}, \quad \alpha'_2 = -\frac{1}{\alpha'_2 c^2}, \quad \alpha'_3 = \frac{1}{\alpha'_3}, \quad \dots, \quad \alpha''_{2+N_s} = \frac{1}{\alpha'_{2+N_s}}, \quad \alpha''_{3+N_s} = \frac{1}{2\alpha'_{3+N_s}\rho c} \quad (213)$$

With

$$\alpha'_1 = 1/2, \quad \alpha'_2 = 1, \quad \alpha'_3 = 1, \quad \dots, \quad \alpha'_{2+N_s} = 1, \quad \alpha'_{3+N_s} = 1/2 \quad (214)$$

the similarity transformation matrix, \mathbf{S} , and its inverse, \mathbf{S}^{-1} , become:

$$\mathbf{S} = \begin{bmatrix} -\rho/2c & 1 & 0 & 0 & \cdot & 0 & \rho/2c \\ 1/2 & 0 & 0 & 0 & \cdot & 0 & 1/2 \\ 0 & 0 & 1/\rho & 0 & \cdot & 0 & 0 \\ 0 & 0 & 0 & 1/\rho & \cdot & 0 & 0 \\ \cdot & \cdot & \cdot & \cdot & \cdot & \cdot & \cdot \\ 0 & 0 & 0 & 0 & \cdot & 1/\rho & 0 \\ -\rho c/2 & 0 & 0 & 0 & \cdot & 0 & \rho c/2 \end{bmatrix} \quad (215)$$

and

$$\mathbf{S}^{-1} = \begin{bmatrix} 0 & 1 & 0 & 0 & \cdot & 0 & -1/\rho c \\ 1 & 0 & 0 & 0 & \cdot & 0 & -1/c^2 \\ 0 & 0 & \rho & 0 & \cdot & 0 & 0 \\ 0 & 0 & 0 & \rho & \cdot & 0 & 0 \\ \cdot & \cdot & \cdot & \cdot & \cdot & \cdot & \cdot \\ 0 & 0 & 0 & 0 & \cdot & \rho & 0 \\ 0 & 1 & 0 & 0 & \cdot & 0 & 1/\rho c \end{bmatrix} \quad (216)$$

The choice of the scaling factors $\alpha'_1, \alpha'_2, \dots, \alpha'_{3+N_s}$, in equation (214) may be verified from the fact that the Riemann invariants arising from the transformation

$$d\tilde{\mathbf{U}} = \mathbf{S}^{-1} d\mathbf{V} \quad (217)$$

are the same as those given by system (133). Because the Riemann invariants must be the same for the conservative system (77) and the primitive system (141),

$$d\tilde{\mathbf{U}} = \mathbf{Q}^{-1} d\mathbf{U} = \mathbf{Q}^{-1} \mathbf{P} d\mathbf{V} = \mathbf{S}^{-1} d\mathbf{V}, \quad (218)$$

the choice of these constants may also be verified by calculating $\mathbf{S}^{-1} = \mathbf{Q}^{-1} \mathbf{P}$ and $\mathbf{S} = \mathbf{P}^{-1} \mathbf{Q}$ using equations (137), (138), (127) and (128). It is seen that this procedure yields the same similarity transformation matrices as obtained from the left and right eigenvectors of \mathbf{B} .

Appendix E

The similarity transformation matrix \mathbf{S} and its inverse \mathbf{S}^{-1} in equations (147) and (148), with \mathbf{B} defined according to equation (180), may be found by following the procedure constituted by equations (118) to (120). This leads to (the eigenvalues Λ_{ii} are sorted in ascending order)

$$\Lambda_{11} = v_x - c, \Lambda_{22} = v_x, \Lambda_{33} = v_x, \dots, \Lambda_{(2+N_s)(2+N_s)} = v_x, \Lambda_{(3+N_s)(3+N_s)} = v_x + c, \quad (219)$$

$$\begin{aligned}
\mathbf{r}_1 &= \alpha'_1 \left[-\frac{\rho}{c}, 1, 0, 0, \dots, 0, -\frac{c}{\gamma \hat{C}_V} \right] \\
\mathbf{r}_2 &= \alpha'_2 \left[1, 0, 0, 0, \dots, 0, -\frac{c^2}{\gamma(\gamma-1)\rho \hat{C}_V} \right] \\
\mathbf{r}_3 &= \alpha'_3 [0, 0, 1, 0, \dots, 0, 0] \\
\mathbf{r}_4 &= \alpha'_4 [0, 0, 0, 1, \dots, 0, 0] \\
&\quad \cdots \\
\mathbf{r}_{2+N_s} &= \alpha'_{2+N_s} [0, 0, 0, 0, \dots, 1, 0] \\
\mathbf{r}_{3+N_s} &= \alpha'_{3+N_s} \left[\frac{\rho}{c}, 1, 0, 0, \dots, 0, \frac{c}{\gamma \hat{C}_V} \right],
\end{aligned} \tag{220}$$

and

$$\begin{aligned}
\mathbf{l}_1 &= \alpha''_1 \left[-\frac{c}{\gamma\rho}, 1, 0, 0, \dots, 0, -\frac{(\gamma-1)\hat{C}_V}{c} \right] \\
\mathbf{l}_2 &= \alpha''_2 \left[\frac{c^2}{\gamma\rho\hat{C}_V}, 0, 0, 0, \dots, 0, 1 \right] \\
\mathbf{l}_3 &= \alpha''_3 [0, 0, 1, 0, \dots, 0, 0] \\
\mathbf{l}_4 &= \alpha''_4 [0, 0, 0, 1, \dots, 0, 0] \\
&\quad \cdots \\
\mathbf{l}_{2+N_s} &= \alpha''_{2+N_s} [0, 0, 0, 0, \dots, 1, 0] \\
\mathbf{l}_{3+N_s} &= \alpha''_{3+N_s} \left[\frac{c}{\gamma\rho}, 1, 0, 0, \dots, 0, \frac{(\gamma-1)\hat{C}_V}{c} \right].
\end{aligned} \tag{221}$$

Since the left and right eigenvectors must fulfill the orthogonality condition (124), the scaling factors $\alpha'_1, \alpha'_2, \dots, \alpha'_{3+N_s}$, and $\alpha''_1, \alpha''_2, \dots, \alpha''_{3+N_s}$ are related to one another as

$$\alpha'_1 = \frac{1}{2\alpha'_1}, \quad \alpha''_2 = \frac{(\gamma-1)\rho\hat{C}_V}{\alpha'_2 c^2}, \quad \alpha''_3 = \frac{1}{\alpha'_3}, \quad \dots, \quad \alpha''_{2+N_s} = \frac{1}{\alpha'_{2+N_s}}, \quad \alpha''_{3+N_s} = \frac{1}{2\alpha'_{3+N_s}} \tag{222}$$

With

$$\alpha'_1 = 1/2, \quad \alpha'_2 = 1, \quad \alpha'_3 = 1, \quad \dots, \quad \alpha'_{2+N_s} = 1, \quad \alpha'_{3+N_s} = 1/2 \tag{223}$$

the similarity transformation matrix, \mathbf{S} , and its inverse, \mathbf{S}^{-1} , become:

$$\mathbf{S} = \begin{bmatrix} -\rho/2c & 1 & 0 & 0 & \cdot & 0 & \rho/2c \\ 1/2 & 0 & 0 & 0 & \cdot & 0 & 1/2 \\ 0 & 0 & 1/\rho & 0 & \cdot & 0 & 0 \\ 0 & 0 & 0 & 1/\rho & \cdot & 0 & 0 \\ \cdot & \cdot & \cdot & \cdot & \cdot & \cdot & \cdot \\ 0 & 0 & 0 & 0 & \cdot & 1/\rho & 0 \\ -\frac{c}{2\gamma\hat{C}_V} & -\frac{c^2}{\gamma(\gamma-1)\rho\hat{C}_V} & 0 & 0 & \cdot & 0 & \frac{c}{2\gamma\hat{C}_V} \end{bmatrix} \tag{224}$$

and

$$\mathbf{S}^{-1} = \begin{bmatrix} -\frac{c}{\gamma\rho} & 1 & 0 & 0 & \cdot & 0 & -\frac{(\gamma-1)\hat{C}_V}{c} \\ \frac{\gamma-1}{\gamma} & 0 & 0 & 0 & \cdot & 0 & -\frac{(\gamma-1)\rho\hat{C}_V}{c^2} \\ 0 & 0 & \rho & 0 & \cdot & 0 & 0 \\ 0 & 0 & 0 & \rho & \cdot & 0 & 0 \\ \cdot & \cdot & \cdot & \cdot & \cdot & \cdot & \cdot \\ 0 & 0 & 0 & 0 & \cdot & \rho & 0 \\ \frac{c}{\gamma\rho} & 1 & 0 & 0 & \cdot & 0 & \frac{(\gamma-1)\hat{C}_V}{c} \end{bmatrix} \quad (225)$$

The choice of the scaling factors $\alpha'_1, \alpha'_2, \dots, \alpha'_{3+N_s}$, in equation (223) may be verified from the fact that the Riemann invariants arising from the transformation (217),

$$d\tilde{\mathbf{U}} = \mathbf{0} \implies \begin{cases} dv_x - \frac{c}{\gamma\rho}d\rho - \frac{(\gamma-1)\hat{C}_V}{c}dT = 0 & \text{for } \frac{dx}{dt} = \Lambda_{11} = v_x - c \\ d\rho - \frac{\gamma\rho\hat{C}_V}{c^2}dT = 0 & \text{for } \frac{dx}{dt} = \Lambda_{22} = v_x \\ dY_1 = 0 & \text{for } \frac{dx}{dt} = \Lambda_{33} = v_x \\ dY_2 = 0 & \text{for } \frac{dx}{dt} = \Lambda_{44} = v_x \\ \dots & \\ dY_{2+N_s} = 0 & \text{for } \frac{dx}{dt} = \Lambda_{(2+N_s)(2+N_s)} = v_x \\ dv_x + \frac{c}{\gamma\rho}d\rho + \frac{(\gamma-1)\hat{C}_V}{c}dT = 0 & \text{for } \frac{dx}{dt} = \Lambda_{(3+N_s)(3+N_s)} = v_x + c \end{cases} \quad (226)$$

are the same as those given by system (133). This becomes evident with the aid of equations (207) and (209). Because the Riemann invariants must be the same for the conservative system (77) and the primitive system (141) according to (218), the choice of these constants may also be verified by calculating $\mathbf{S}^{-1} = \mathbf{Q}^{-1}\mathbf{P}$ and $\mathbf{S} = \mathbf{P}^{-1}\mathbf{Q}$ using equations (178), (179), (127) and (128). It is seen that this procedure yields the same similarity transformation matrices as obtained from the left and right eigenvectors of \mathbf{B} .